AREVA

SOURCE REFERENCE RECORD

Source Reference for: _____ 43-10231(NP)A-01 / COPERNIC Fuel Rod Design Computer Code
Document Number/Title

File No.	Subject	Remarks/Applicable Licensing Document
32-5016629-01	Temperature Uncertainty for MOX Fuel Thermal Analyses with COPERNIC	

BAW-10231(NP)-A
Revision 1
January 2004

COPERNIC Fuel Rod Design Computer Code

NON PROPRIETARY

FRAMATOME ANP

U.S. Nuclear Regulatory Commission

Report Disclaimer

Importance Notice Regarding Contents and Use of this document

Please Read Carefully

This technical report was derived through research and development programs sponsored by FRAMATOME ANP. It is being submitted by FRAMATOME ANP to the U.S. Nuclear Regulatory Commission as part of a technical contribution to facilitate safety analyses by licensees of the U.S. Nuclear Regulatory Commission with utilize FRAMATOME ANP fabricated reload fuel or technical services provided by FRAMATOME ANP for light power reactors and it is true and correct to the best of FRAMATOME ANP knowledge, information and belief. The information contained herein may be used by the U.S. Nuclear Regulatory Commission in its review of this report and, under the terms of the respective agreements, by licensees or applicants before the U.S. Nuclear Regulatory Commission which are customers of FRAMATOME ANP in their demonstration of compliance with the U.S. Nuclear Regulatory Commission's regulations.

FRAMATOME ANP's warranties and representations concerning the subject matter of this document are those set forth in the agreement between FRAMATOME ANP and the Customer pursuant to which this document is issued. Accordingly, except as otherwise expressly provided in such agreement, neither FRAMATOME ANP nor any person acting on its behalf:

a. makes any warranty, or representation, expressed or implied, with respect to the accuracy, completeness, or usefulness of the information contained in this document, or that the use of any information, apparatus, method, or process disclosed in this document will not infringe privately owned rights;

   or

b. assumes any liabilities with respect to the use of, or for damages resulting from the use of, any information, apparatus, method, or process disclosed in this document.

UNITED STATES
NUCLEAR REGULATORY COMMISSION
WASHINGTON, D.C. 20555-0001

January 14, 2004

Mr. James Mallay
Director, Regulatory Affairs
Framatome ANP
3815 Old Forest Road
Lynchburg, VA 24501

SUBJECT: FINAL SAFETY EVALUATION FOR TOPICAL REPORT BAW-10231P, "COPERNIC FUEL ROD DESIGN CODE" CHAPTER 13, MOX APPLICATIONS (TAC NO. MB7547)

Dear Mr. Mallay:

On July 31, 2000, Framatome ANP (FANP) submitted Topical Report (TR) BAW-10231P, "COPERNIC Fuel Rod Design Code," Chapter 13, MOX Applications, to the staff. On November 21, 2003, an NRC draft safety evaluation (SE) regarding our approval of BAW-10231P was provided for your review and comments. By letter dated December 4, 2003, FANP commented on the draft SE. The staff's disposition of FANP's comments on the draft SE are discussed in the attachment to the final SE enclosed with this letter.

The staff has found that BAW-10231P, Chapter 13, is acceptable for referencing in licensing applications for pressurized water reactors to the extent specified and under the limitations delineated in the report and in the enclosed SE. The SE defines the basis for acceptance of the report.

Our acceptance applies only to material provided in the subject report. We do not intend to repeat our review of the material described in the report. When the report appears as a reference in license applications, our review will ensure that the material presented applies to the specific plant involved. License amendment requests that deviate from this TR will be subject to a plant-specific review in accordance with applicable review standards.

In accordance with the guidance provided on the NRC website, we request that FANP publish an accepted version of this TR within three months of receipt of this letter. The accepted version shall incorporate this letter and the enclosed SE between the title page and the abstract. It must be well indexed such that information is readily located. Also, it must contain in appendices historical review information, such as questions and accepted responses, draft SE comments, and original report pages that were replaced. The accepted version shall include a "-A" (designating accepted) following the report identification symbol.

If the NRC's criteria or regulations change so that its conclusion in this letter, that the TR is acceptable, is invalidated, FANP and/or the licensees referencing the TR will be expected to revise and resubmit its respective documentation, or submit justification for the continued applicability of the topical report without revision of the respective documentation.

Sincerely,

Herbert N. Berkow, Director
Project Directorate IV
Division of Licensing Project Management
Office of Nuclear Reactor Regulation

Project No. 728

Enclosure: Safety Evaluation

UNITED STATES
NUCLEAR REGULATORY COMMISSION
WASHINGTON, D.C. 20555-0001

SAFETY EVALUATION BY THE OFFICE OF NUCLEAR REACTOR REGULATION

BAW-10231P, "COPERNIC FUEL ROD DESIGN COMPUTER CODE"

CHAPTER 13 - MOX APPLICATIONS

FRAMATOME ANP

PROJECT NO. 728

1.0 INTRODUCTION

Framatome Cogema Fuels (FCF) (now known as Framatome ANP [FANP]) submitted to the NRC staff Chapter 13 (Reference 1) of Topical Report (TR) BAW-10231P, entitled "COPERNIC Fuel Rod Design Computer Code," for review and approval. Chapter 13 describes a design and analysis methodology for mixed oxide (MOX) fuel rod performance. MOX fuel pellets have a mixture of uranium dioxide (UO_2) and plutonium dioxide (PuO_2). This report deals with the use of weapons grade (WG) PuO_2 in MOX fuel designs.

The staff has previously approved the COPERNIC code for UO_2 licensing applications (References 2 and 3) with advanced cladding material, M5, to a peak rod average burnup of 62 GWd/MTU. Although Chapter 13 is an extended application of the COPERNIC code, detailed MOX fuel designs including irradiation experiences are described in other FANP TRs such as BAW-10238(P), Revision 1, entitled "MOX Fuel Design Report," that describes FANP's use of WG PuO_2. FANP requested an approval of the COPERNIC code for MOX licensing applications to a Pu content of 6 weight percent (wt%) and a peak rod average burnup of 53 GWd/MThm. Although FANP obtained some data beyond 53 GWd/MThm, the staff review and audit verifications are only up to a peak rod average burnup of 50 GWd/MThm. The staff considers that since this fuel will be irradiated for a maximum of two fuel cycles, 50 GWd/MThm will be sufficient. This conservative limitation is appropriate after considering the applicable data and audit calculations.

As a result of the staff's review, assisted by its consultant, Pacific Northwest National Laboratory (PNNL), two requests for additional information (RAIs) were sent to FANP (References 4 and 5). FANP provided responses in References 6, 7, and 8.

This review addresses those major computer models of the MOX fuel design features in the COPERNIC code that are different from the UO_2 fuel design features, and the MOX fuel design licensing applications. The licensing applications include fuel melting analysis, fuel rod internal pressure, cladding strain, and stored energy for a loss-of-coolant accident (LOCA).

The staff used the NRC audit code, FRAPCON-3.2 with MOX properties (Reference 9), to evaluate the models and analytical results from the COPERNIC code. The FRAPCON-3.2 code is a modification of the UO_2 version of the FRAPCON-3 code (Reference 10). The

FRAPCON-3.2 code has been verified against thermal data from irradiated MOX fuel rod segments to rod average burnup of 60 GWd/MThm. The verification process demonstrated that the FRAPCON-3.2 code provided best-estimate predictions of the thermal and fission gas release data for MOX fuel rods.

2.0 REGULATORY EVALUATION

The objectives of the fuel system safety review are to provide assurance that (1) the fuel system is not damaged as a result of normal operation and anticipated operational occurrences, (2) fuel system damage is never so severe as to prevent control rod insertion when it is required, (3) the number of fuel rod failures is not underestimated for postulated accidents, and (4) coolability is always maintained. The staff acceptance criteria are based on Chapter 4.2, "Fuel System Design," of the Standard Review Plan (SRP). These criteria include three parts: (1) design bases that describe specified acceptable fuel design limits as depicted in General Design Criterion 10 to 10 CFR Part 50, Appendix A, (2) design evaluation that demonstrates that the design bases are met, and (3) testing, inspection, and surveillance plans that show that there is adequate monitoring and surveillance of irradiated fuel. The design bases include (1) fuel system damage, (2) fuel rod failure, and (3) fuel coolability.

3.0 TECHNICAL EVALUATION

3.1 Fuel Thermal Conductivity

The COPERNIC MOX fuel thermal conductivity model is similar to that used for UO_2 (including the burnup dependence) with the addition of two terms, which are functions of PuO_2 content and oxygen-to-metal (O/M) ratio. The staff compared the COPERNIC MOX thermal conductivity model to the MOX thermal conductivity model (Reference 11) used in the FRAPCON-3.2 code. The MOX thermal conductivity model in FRAPCON-3.2 is based on the Duriez model (Reference 12) for unirradiated MOX fuel pellets (with O/M dependence) along with the burnup dependence proposed by the staff's consultant, PNNL (References 13 and 14). The comparison showed that the two models were close for the low burnup regime, and FRAPCON-3.2 had slightly higher fuel temperature predictions than COPERNIC for the high burnup regime.

The comparison of the COPERNIC MOX thermal conductivity model to in-reactor Halden fuel temperature data also showed a similar trend of good agreement between the two except at the high burnup regime. The COPERNIC model could slightly underpredict fuel temperatures at the high burnup regime. Overall, the COPERNIC model showed consistent results with the FRAPCON-3.2 code and Halden data.

Based on the overall good agreement of the temperature predictions, the staff concludes that the MOX thermal conductivity model is acceptable for the COPERNIC MOX code to a peak rod average burnup of 50 GWd/MThm.

3.2 Fission Gas Release

Fission gas release is important because it degrades the fuel-to-clad gap conductance and simultaneously increases fuel rod pressures. There are two fission gas release (FGR) models

in the COPERNIC code: a steady-state model and a transient model. FANP has FGR data from the Halden reactor as well as its own irradiation program.

The audit code FRAPCON-3.2 uses a release model that is taken from the American Nuclear Society (ANS) Standard 5.4 (Reference 15) and a thermally-activated diffusion model proposed by Forsberg and Massih (Reference 16) with modifications to the diffusion coefficient. The FRAPCON-3.2 model also assumes that the fission gas is stored on the grain boundary until saturation, and the gas saturation level is the same for MOX and UO_2 fuel. The COPERNIC code adopts a similar approach.

The COPERNIC code was compared to MOX FGR from steady-state power operations. The COPERNIC comparisons to the data showed that the code provided a best-estimate calculation of FGR for steady-state operations. The COPERNIC code assumes that the transient release model for MOX is identical to that for UO_2 fuel. The transient release results were compared to power ramp data. The COPERNIC code conservatively overpredicted the measured FGR on most of the power ramp data. Based on the overprediction of the majority of the data, the staff considers that the FGR models have adequate conservatism and the predictions are acceptable.

FGR has significant impact on the end-of-life (EOL) rod pressure analysis for the peak operating rods within a core. The rod pressure analysis generally limits the peak linear heat generation rates (LHGRs) at high burnup levels. The staff performed an audit calculation of an EOL rod pressure provided by FANP using best-estimate input values. This audit calculation demonstrated that the audit code predicted slightly higher rod pressures than the COPERNIC code at EOL, but the differences were very small when compared to the uncertainties in the analysis.

Based on the good agreement between the two codes, the staff concludes that the FGR predictions are acceptable for the COPERNIC MOX code to peak rod average burnup of 50 GWd/MThm.

3.3 Fuel Densification and Swelling

The fuel densification and swelling models in COPERNIC are important for cladding strain, fuel melting, and LOCA analyses. FANP determined the fuel densification according to the recommendation of Regulatory Guide 1.126, "An Acceptable Model and Related Statistical Methods for the Analysis of Fuel Densification" (Reference 17). FANP provided data to demonstrate that the MOX fuel was similar to UO_2 fuel in fuel densification and swelling performance. The COPERNIC predictions also compared reasonably well with those measured from MOX fuel. A comparison of the densification and swelling models in COPERNIC and FRAPCON-3.2 showed that the two models were very similar in densification kinetics.

Based on the comparison of the two codes with the densification and swelling data, the staff concludes that the fuel densification and swelling models are acceptable for the COPERNIC MOX code to a peak rod average burnup of 50 GWd/MThm.

3.4 Power-to-Melt Analysis

The difference between COPERNIC and FRAPCON-3.2 fuel thermal conductivity models at the high temperature regime leads to a difference in power-to-melt calculations. The staff performed an audit calculation using the FRAPCON-3.2 code. The results showed that the two codes predicted very closely at the beginning of life, but the COPERNIC code predicted a slightly higher result than the FRAPCON-3.2 code for higher burnups. The staff considers that the minor difference in the power-to-melt analysis has little impact in the overall safety analyses.

Based on the conservative thermal models and the comparisons with the audit code, the staff concludes that the power-to-melt analysis is acceptable for the COPERNIC MOX code to a peak rod average burnup of 50 GWd/MThm.

3.5 Fuel Rod Internal Pressure

FANP uses the COPERNIC code to verify the maximum EOL rod pressure for a MOX fuel design. FANP provided an EOL fuel rod internal pressure analysis of a Mark-BW fuel design. The staff performed an audit calculation with FRAPCON-3.2 using the same input, and FRAPCON-3.2 predicted similar results as COPERNIC.

Based on the similar results, the staff concludes that the fuel rod internal pressure analysis is acceptable for the COPERNIC MOX code to a peak rod average burnup of 50 GWd/MThm.

3.6 Clad Strain

Chapter 4.2 of the SRP establishes that the 1 percent strain limit should be used for normal operation and anticipated operational occurrences. FANP provided a clad strain analysis of a Mark-BW fuel design. The staff performed an audit calculation with FRAPCON-3.2 using the same input. The results showed that FRAPCON-3.2 predicted a slightly lower threshold than COPERNIC in reaching the 1 percent strain limit. The staff considers that the difference has little impact in the safety analyses because of the code conservatism and very limited irradiated strain data.

Based on the conservative mechanical models and compatible results, the staff concludes that the cladding strain analysis is acceptable for the COPERNIC MOX code to a peak rod average burnup of 50 GWd/MThm.

3.7 Stored Energy

FANP uses the COPERNIC MOX code to calculate initial fuel stored energy for LOCA analyses to verify that the MOX fuel design meets the requirements of Appendix K to 10 CFR Part 50. The fuel stored energy is approximately proportional to the fuel volume-average temperature.

The staff uses prediction-to-measurement comparisons at LHGR levels for LOCA stored energy calculations to estimate uncertainty including standard deviation in fuel performance codes. The uncertainty is then applied to code predictions to obtain a conservative stored energy prediction at a 95/95 tolerance level (bounding 95 percent of the measured data with a 95

percent confidence) for LOCA analyses. The staff used the FRAPCON-3.2 code to compare the results from the COPERNIC code for stored energy calculations to a peak rod average burnup of 50 GWd/MThm.

All fuel performance codes with UO_2 fuel examined by the staff, including the FRAPCON code, have a standard deviation equivalent to 6 to 8 percent. The 6 to 8 percent standard deviation is consistent with the standard deviation of the measured UO_2 fuel rod powers. FANP demonstrated that the COPERNIC code predicted best-estimate, i.e., small standard deviation, fuel centerline temperatures for the Halden MOX irradiated data. The COPERNIC code has a smaller standard deviation for the MOX data than for the UO_2 data. The COPERNIC code predicted small standard deviation on the MOX data may be attributed to two different reasons: (1) the LHGRs of the majority of the MOX data are low resulting in low measured temperatures, and (2) the number of irradiated MOX fuel rods is much smaller than the number of irradiated UO_2 fuel rods.

A comparison between predicted and measured fuel temperatures at a 95/95 tolerance level from these irradiated MOX data showed that the COPERNIC code slightly underpredicted fuel temperatures. The COPERNIC fuel temperature uncertainty performance is consistent with the audit code FRAPCON-3.2 behavior in that both codes slightly underpredict the data at a 95/95 tolerance level. The staff recognizes that the MOX fuel has a smaller data base than the UO_2 data base. In order to compensate for the smaller data base and the underprediction, FANP opted for a conservative approach using a large fuel uncertainty from the UO_2 data base for the MOX fuel stored energy calculations (Reference 18). Based on the small data base and conservative treatment of uncertainty, the staff accepted this conservative approach to address the under prediction.

Based on the best-estimate performance and a conservative approach to the 95/95 tolerance, the staff concludes that the stored energy analysis for LOCA initial conditions is acceptable for the COPERNIC MOX code to a peak rod average burnup of 50 GWd/MThm.

4.0 CONCLUSION

The staff has reviewed the FANP MOX fuel rod performance in Chapter 13 of the COPERNIC code of BAW-10231P. Based on the staff's review, as supplemented by its contractor's, PNNL, review and evaluation, the staff concludes that the COPERNIC code is acceptable for MOX fuel licensing applications up to a WG Pu content of 6 wt% and a peak rod average burnup of 50 GWd/MThm. Future staff reviews involving MOX fuel design, for example, BAW-10238(P) Revision 1, entitled "MOX Fuel Design Report," may result in additional restrictions on the licensing applications of the COPERNIC code.

5.0 REFERENCES

1. Framatome Cogema Fuels. July 31, 2000. *COPERNIC Fuel Rod Design Computer Code, Chapter 13 MOX Application.* BAW-10231P, Framatome Cogema Fuels, Lynchburg, Virginia, transmitted by letter, T. A. Coleman (Framatome Cogema Fuels) to U.S. NRC Document Control Desk, "Topical Report BAW-10231P, COPERNIC Fuel Rod Design Computer Code, Chapter 13 MOX Applications," dated September 16, 1999, GR00-088.doc.

2. Framatome Cogema Fuels. September 1997. *COPERNIC Fuel Rod Design Computer Code.* BAW-10231P, Framatome Cogema Fuels, Lynchburg, Virginia, transmitted by letter, T. A. Coleman (Framatome Cogema Fuels) to U.S. NRC Document Control Desk, "Topical Report BAW-10231P, COPERNIC Fuel Rod Design Computer Code," dated September 16, 1999, GR99-191.doc.

3. Framatome Cogema Fuels. *COPERNIC Fuel Rod Design Computer Code, Chapter 12 Application Methodology (United States).* BAW-10231P, Framatome Cogema Fuels, Lynchburg, Virginia, transmitted by letter, Stewart Bailey, NRC, to T. A. Coleman, Framatome Cogema Fuels, - *COPERNIC Fuel Rod Design Computer Code, Chapter 12 Application Methodology (United States)* Topical Report BAW-10231P, December 2, 1999, GR99-234.doc.

4. Letter, Stewart Bailey (NRC) to T. A. Coleman (Framatome ANP), "Request for Additional Information - Chapter 13 of Framatome Topical Report BAW-10231P (TAC No. MA9783)," May 14, 2001.

5. Letter, Drew Holland (NRC) to James Mallay (Framatome ANP), "Request for Additional Information - BAW-10231P, Chapter 13, COPERNIC MOX Applications, Fuel Rod Design Computer Code," dated April 25, 2002.

6. Letter, James Mallay (Framatome ANP) to NRC Document Control Desk, "Partial Response to RAI," NRC:01:033, July 27, 2001.

7. Letter, James Mallay (Framatome ANP) to NRC Document Control Desk, "Partial Response to RAI on Chapter 13 of BAW-10231P," NRC:02:021, April 26, 2002.

8. Letter, James Mallay (Framatome ANP) to NRC Document Control Desk, "Partial Response to RAI on Chapter 13 of BAW-10231P," NRC:02:038, July 17, 2002.

9. Berna, G.A., C.E. Beyer, K.L. Davis and D.D. Lanning. 1997. *FRAPCON-3: A Computer Code for the Calculation of Steady-State, Thermal-Mechanical Behavior of Oxide Fuel Rods for High Burnup.* NUREG/CR-6534 (PNNL-11513) Vol. 2. U.S. Nuclear Regulatory Commission, Washington, D.C.

10. Lanning, D.D., C.E. Beyer and C.L. Painter. 1997. *FRAPCON-3: Modifications to Fuel Rod Material Properties and Performance Models for High-Burnup Applications.* NUREG/CR-6534 (PNNL-11513) Vol. 1. U.S. Nuclear Regulatory Commission, Washington, D.C. 20555-0001.

11. Lanning, D. D. and C. E. Beyer. 2002. "Proposed FRAPCON-3 MOX Fuel Thermal Conductivity Model Compare to Halden Fuel Temperature Data," *Presented at Enlarged Halden Program Meeting, September 8-13, 2002.*

12. Duriez, C., J.P. Alleşandri, T. Gervais, and Y. Philipponneau. 2000. "Thermal Conductivity of Hypostoichiometric Low Pu Content (U,Pu)O_{2-x} Mixed Oxide." *Journal of Nuclear Materials* 277:143-158.

13. Lanning, D.D., C.E. Beyer, and M.E. Cunningham. 2000. "FRAPCON-3 Fuel Rod Temperature Predictions with Fuel Conductivity Degradation Caused by Fission Products and Gadolinia Additions," in *Proceedings of the ANS International Topical Meeting on Light Water Reactor Fuel Performance, Park City, Utah, April 2000,* pages 261 to 274.

14. Lanning, D. D. and C. E. Beyer. 2001. "Assessment of Recent Data and Correlations for Fuel Pellet Thermal Conductivity," *Presented at Enlarged Halden Program Meeting March 11-16, 2001*, HPR-356.

15. American Nuclear Society (ANS). 1982. *Method for Calculating the Fractional Release of Volatile Fission Products from Oxide Fuel,* ANSI/ANS-5.4-9182. ANS 5.4 of the Standards Committee of the American Nuclear Society.

16. Forsberg, K. and A. R. Massih. 1985. "Diffusion Theory of Fission Gas Migration in Irradiated Nuclear Fuel UO_2," *J. of Nucl. Mater.*; Vol. 135, pp. 140-148.

17. Regulatory Guide 1.126, Revision 1, "An Acceptable Model and Related Statistical Methods for the Analysis of Fuel Densification," 1978.

18. Letter, James Mallay (Framatome ANP) to NRC Document Control Desk, "Final Responses to RAIs on Chapter 13 of BAW-10231P," NRC:03:027, April 18, 2003.

Attachment: Resolution of Comments

Principal Contributor: S. Wu

Date: January 14, 2004

RESOLUTION OF COMMENTS

ON DRAFT SAFETY EVALUATION EVALUATION FOR BAW-10231, "COPERNIC FUEL ROD DESIGN CODE" CHAPTER 13, MOX APPLICATIONS

By letter dated December 4, 2003, Framatome ANP (FANP) provided comments on the draft safety evaluation (SE) for BAW-10231, "COPERNIC Fuel Rod Design Code," Chapter 13, MOX Applications. The following is the staff's resolution of those comments.

1. FANP Comment: Section 1.0, first paragraph, fourth sentence states, "Currently, there are two types of PuO_2 in MOX fuel designs used in commercial nuclear reactors: reactor-grade PuO2 fuel and WG PuO_2 fuel."

   FANP Proposed Resolution: Weapons-grade fuel is not currently used in commercial nuclear reactors. Framatome ANP suggests rewording this sentence to: "Currently, there are two types of PuO_2 in MOX fuel designs."

   NRC Action: The staff considers it necessary to point out that WG PuO_2 is the fuel material discussed in the report. To avoid confusion, reactor grade PuO_2 is not mentioned in the safety evaluation.

2. FANP Comment: The units for burnup for MOX fuel used throughout the SE are indicated as GWd/MTU.

   FANP Proposed Resolution: The units for burnup for MOX fuel should be indicated as GWd/MThm (gigawatt days per metric tonne of initial heavy metal).

   NRC Action: This comment was fully adopted in the final SE

3. FANP Comment: Section 1.0, second paragraph, last sentence states, "However, the staff notes that the MOX irradiated data provided by FANP and audit verifications are only up to a peak rod average burnup of 50 GWd/MTU."

   FANP Proposed Resolution: Data provided by FANP exceeded peak rod average burnup of 50 GWd/MThm in numerous instances. The original submittal, BAW-10231, Rev. 0, pages 5-48 and 5-49 (and pages 9-34 and 9-35), identifies six MOX data points in excess of 50 GWd/MThm.

   FANP suggested that this sentence state: "To support this request, FANP provided MOX irradiated data, including audit verifications, to peak rod average burnups extending to 63 GWd/MThm."

   NRC Action: This comment was addressed in the final SE, but not exactly as requested. The following wording was used: "Although FANP obtained some data beyond 53 GWd/MThm, the staff review and audit verifications are only up to a peak rod average burnup of 50 GWd/MThm. The staff considers that since this fuel will be irradiated for a maximum of two fuel cycles, 50 GWd/MThm will be sufficient. This conservative limitation is appropriate after considering the applicable data and audit calculations."

UNITED STATES
NUCLEAR REGULATORY COMMISSION
WASHINGTON, D.C. 20555-0001
June 14, 2002

Mr. James Mallay
Director, Regulatory Affairs
Framatome ANP, Richland, Inc.
2101 Horn Rapids Road
Richland, WA 99352

SUBJECT: FRAMATOME ANP TOPICAL REPORT BAW-10231, "COPERNIC FUEL ROD DESIGN COMPUTER CODE" - CORRECTION OF ERROR IN SAFETY EVALUATION (TAC NO. MA6782)

Dear Mr. Mallay:

By letter dated April 18, 2002, the NRC staff transmitted its safety evaluation (SE) on BAW-10231 to Framatome ANP. In a May 1, 2002, letter, you notified us that the SE contained an error on page 6. Therefore, the second sentence of Section 5.0, "Fuel Densification and Swelling Models" is modified to read: "The modeling of fuel densification and solid swelling in COPERNIC are included together as one model for the Integrated Dry Route (IDR) and Ammonium Di-Uranate (ADU) fuel employed by FCF in the U. S. FCF also has a separate densification and swelling model for the Ammonium Uranyl Carbonate (AUC) fuel but this fuel is not used commercially and there are no plans for its use in U. S. plants." The April 18, 2002, SE also contained administrative errors. Therefore, we are reissuing the SE with this letter in its entirety. In accordance with the guidance provided in NUREG-0390, we request that Framatome include this revised SE in the published proprietary and nonproprietary version of this topical report.

We apologize for any inconvenience this may have caused. If you have any questions, please call Drew Holland at (301) 415-1436.

Sincerely,

Stephen Dembek, Chief, Section 2
Project Directorate IV
Division of Licensing Project Management
Office of Nuclear Reactor Regulation

Project No. 693

Enclosure: Corrected Safety Evaluation

UNITED STATES
NUCLEAR REGULATORY COMMISSION
WASHINGTON, D.C. 20555-0001

SAFETY EVALUATION BY THE OFFICE OF NUCLEAR REACTOR REGULATION

TOPICAL REPORT BAW-10231P

"COPERNIC FUEL ROD DESIGN COMPUTER CODE"

FRAMATOME COGEMA FUELS

PROJECT NO. 693

1.0 INTRODUCTION

On September 16, 1999, Framatome Cogema Fuels (FCF) submitted to the NRC the revised Topical Report (TR) BAW-10231P (Reference 1), entitled "COPERNIC Fuel Rod Design Computer Code," for review and approval. The COPERNIC computer code is an improved fuel performance code for fuel rod design and analysis of natural, slightly enriched (up to 5 percent) uranium dioxide fuels and urania-gadolinia fuels with the advanced cladding material, M5. Chapter 13 of the TR deals with fuel rod design and analysis of mixed oxide fuel, and will be reviewed later with a separate safety evaluation (SE). FCF uses another approved fuel performance code (TACO3) for licensing applications of zircaloy-4 cladding.

Pacific Northwest National Laboratory (PNNL) acted as a consultant to the NRC for this review. As a result of the NRC staff and PNNL review of the topical report, a request for additional information (RAI) was sent by the NRC to FCF (Reference 2). FCF provided a response to this RAI in Reference 3. Since the issuance of the TR and Reference 3 response, FCF has changed their name to Framatome ANP. The FCF name will be used in this SE.

The SE addresses several major areas of the COPERNIC code including thermal models, material properties, fission gas release, corrosion and hydriding, fuel swelling and densification, mechanical models, and licensing applications. The licensing applications include stored energy and rod pressure inputs to the loss-of-coolant accident (LOCA), maximum rod internal pressures and rod pressure limits, cladding strain, and fuel melting analyses. Audit calculations have been made with the NRC developed FRAPCON-3 fuel performance code for comparison to COPERNIC calculations for maximum rod internal pressure, LOCA temperatures (stored energy) and pressures, temperatures for the fuel melting, and clad strain analyses.

2.0 THERMAL MODELS

2.1 Fuel Thermal Conductivity

The COPERNIC fuel thermal conductivity model is composed of a phonon term and a high-temperature electronic term, and a temperature-dependent porosity correction factor. The phonon term has both a burnup degradation function and a radiation degradation term in its denominator. However, the burnup degradation term is not as dominant as that contained in

the Nuclear Fuel Industries (NFI) model, nor as dominant as that in two other recently published thermal conductivity models by Halden (Reference 4) and the French utility Electricite de France (EDF) (Reference 5). Furthermore, the model underpredicts the high temperature conductivity data for unirradiated UO_2 recently published by Ronchi, et al. (Reference 6).

The NRC audit code, FRAPCON-3, currently utilizes two fuel thermal conductivity models: (1) a model proposed by Lucuta, et al. (Reference 7) that was originally used in the code, and (2) an alternate conductivity model proposed by NFI of Japan (Reference 8). The NFI model is based on more recent high burnup thermal conductivity data and provides the best comparisons to both in-reactor fuel temperature and ex-reactor diffusivity data at high burnup (References 9 and 10). The NFI model has a larger degradation in thermal conductivity with fuel burnup than the Lucuta, et al. model, and thus provides higher predicted fuel temperatures with increasing burnup. The staff considers that the NFI model is better than the Lucuta, et al. model for use at high burnups with the FRAPCON-3 code, and it is therefore the primary model used for comparison to the COPERNIC code.

The staff requested (Reference 2) and received FCF information (Reference 3) that provided sufficient detailed design and operating history information to allow for one high-burnup database case comparison calculation (the "EXTRAFORT" rod) with FRAPCON-3. This case involved a re-fabricated high-burnup (58 GWd/MTU) pressurized water reactor (PWR) rod section that was instrumented with a fuel centerline thermocouple and then operated in the OSIRIS test reactor. FRAPCON-3 has been verified against a large amount of high burnup fuel rod data, including fuel centerline temperature measurements. The EXTRAFORT data were also compared with FRAPCON-3 code predictions as further verification of the code. The measured fuel temperatures were slightly under predicted by the FRAPCON-3 code (Lucata thermal conductivity) and slightly overpredicted when the NFI thermal conductivity model was used in the code. The COPERNIC code also slightly overpredicted the temperatures in the EXTRAFORT rod.

The staff (Reference 2) also requested and obtained (Reference 3) a comparison between COPERNIC predictions and data from Halden re-fabricated, instrumented boiling water reactor (BWR) high-burnup rod segment IFA-597.2/3. This rod was base-irradiated to 60 GWd/MTU in the Ringhals BWR and then re-fabricated with a fuel centerline thermocouple and irradiated at a nominal power (20 to 25 kW/m) in the Halden test reactor for approximately 100 days, thereby extending the rod-average burnup to 70 GWd/MTU. The COPERNIC code underpredicted the measured fuel temperatures for this rod near the end of the irradiation at 70 GWd/MTU. FCF also provided COPERNIC predictions of the widely used IFA 562 Rod 16 and 18 (Halden Ultra-High Burnup) data commonly referred to as the HUHB data. These comparisons to the two IFA 562 rods shows that the code underpredicted the temperatures for both rods when rod-average burnups exceed 35 GWd/MTU.

The overall code-data fuel temperature comparisons for COPERNIC indicate that the code predictions compare well to data, or are conservative at low fuel burnups. However, at medium to high burnup, the code's comparisons to data show mixed results, with a mean prediction of FCF data and an underprediction of the NRC database from the Halden reactor at high burnup. The comparison of the COPERNIC thermal conductivity model to other recently published models, plus in-reactor Halden data, and ex-reactor unirradiated data suggests that the code slightly overpredicts thermal conductivity at moderate to high burnups, and also slightly

overpredicts thermal conductivity at low burnups when fuel temperatures approach fuel melting. The small overprediction in fuel thermal conductivity results in a slight underprediction in fuel temperatures for some licensing analyses. Based on an acceptable uncertainty level and good agreement of the temperature predictions between the COPERNIC and NRC audit codes, the staff considers that the thermal conductivity model is acceptable in the COPERNIC code.

2.2 Other Models and Properties

The clad-coolant heat transfer coefficient is calculated as a function of mass flow rate, hydraulic diameter and coolant temperature by the "SAURY" relationship. This was compared to the Dittus-Boelter relationship in FRAPCON-3 and found to be conservative. Because the Dittus-Boelter equation is a standard relationship for the clad and coolant heat transfer, this model is considered acceptable.

The oxide growth model generates a significant oxide layer on the cladding at mid-to-high burnup, even for M5 cladding. The conductivity of this layer as a function of temperature is about 10 to 20 percent higher than the FRAPCON-3/MATRO-11 model. The basis for this conductivity was not given in the original documentation, but in response to RAI question number 22, the basis was stated to be experimental data. The difference between the COPERNIC oxide conductivity and that in FRAPCON-3 is within the uncertainty of this data. Thus, the staff considers that this model is acceptable.

The gap conductance coefficient is the sum of the radiation, gas conduction, and solid-solid contact conduction components. The radiation component is a standard formulation that compares well to FRAPCON-3. The solid-solid contact component is very similar to FRAPCON-3, and compares well to Garnier-Begej (References 11 and 12) ex-reactor data sets for mated Zircaloy-UO2 compacts of varying characterized surface morphologies (roughness) With the good agreement between COPERNIC and FRAPCON-3 codes, the staff considers that the contact conductance model is acceptable for modeling gap conductance for M5 cladding.

The gas conduction function for large fuel-clad gaps is a standard formulation that compares closely to GAPCON/FRAPCON. The gas conduction for small gaps (relative to the fuel/cladding roughness) is the model put forward in 1986 by Wesley and Yavanovich (Reference 13). This model was approved for use in the TACO3 code that has been demonstrated to predict conservatively against the full Garnier-Begej database, including the high-gas pressure database. Because of the approved model, the staff concludes that the gas conduction model is acceptable for the COPERNIC code.

The radial power profile used in COPERNIC is determined from values calculated with the APOLLO2 neutronic transport code (Reference 14) for UO_2 and MOX at different burnup levels. These values are tabulated in COPERNIC and are activated by specifying the U-235 and Pu enrichments. The UO_2-Gd_2O_3 radial powers are entered from a neutronic code calculation of the specific enrichment and core configuration. Examination of the COPERNIC code shows that the radial power profiles become peaked in light-water reactor (LWR) pellets as low as 14 GWd/MTU burnup, according to the APOLLO2 code predictions. The differences between the COPERNIC predicted radial power profiles and those predicted by the TUBRNP model in FRAPCON-3 are relatively small considering that they have only a small impact on calculated

temperatures. Because of the small differences between the COPERNIC and FRAPCON-3 codes, the staff concludes that the radial power profiles are acceptable for the COPERNIC code.

3.0 FISSION GAS RELEASE (FGR) MODEL

Two FGR models operate within the COPERNIC code: a steady-state model and a transient model that tracks the fuel response to rapid power changes.

The COPERNIC steady-state model has two parts: an athermal knockout-recoil component and thermally-activated diffusion component, leading to grain boundary accumulation, saturation, and release.

The athermal portion depends on burnup and rim width and compares slightly conservatively relative to the FRAPCON-3/ANS5.4 athermal model. The athermal model predicts FGR values of less than one percent so that this model is not significant for most analyses that evaluate the limiting rods in a core.

The thermally activated diffusion to the grain boundary results in saturation of the boundary and subsequent release as burnup increases. Once saturation is achieved, the code conservatively assumes that there is an ongoing pathway for release; i.e., once a fuel segment (ring) has achieved saturation, all subsequently produced gas is released from that segment. The diffusion constant is made up of three parts, one of which depends on temperature alone, one on temperature and fission rate, and one on fission rate alone. A comparison of the FRAPCON-3 diffusion coefficients shows that the two match closely at mid-life burnup. The discrepancy at higher burnups is not significant because the power and temperature levels in commercial rods decrease at high burnups and significant FGR is usually encountered as a result of power transients, for which COPERNIC has a completely different model.

The NRC audit code FRAPCON-3 utilizes an athermal release model from ANS 5.4 (Reference 15) and a thermally activated diffusion model proposed by Forsberg and Massih (Reference 16) with modifications to the diffusion coefficient. The COPERNIC predicted cumulative FGR as a function of burnup at constant linear heat generation rate (LHGR) and temperature is similar to that predicted by the Massih model in FRAPCON-3. At high temperatures above 1100°C, the FRAPCON-3 model predicts greater FGR than COPERNIC. FRAPCON-3 predicts a greater FGR than COPERNIC in the range between 900 and 1100°C for burnups greater than 40 GWd/MTU. From 900°C downward, the COPERNIC model predicts more rapid incubation and hence higher FGR in the 40 to 60 GWd/MTU range. However, the overall trend of the COPERNIC FGR model predictions are consistent with the FRAPCON-3 results.

The transient gas release model consists of an enhanced diffusion model for short times, and a burst model that involves controlled release of the grain boundary gas inventory on a time basis related to the current diffusion constant.

The COPERNIC code has been compared against a database of punctured and analyzed fuel rods from LWRs and test reactors that demonstrates that the code provides a best estimate

prediction of this data. This database includes a number of test reactor rod cases from steady-state and transient power operation that are typically used for fuel rod performance code validation. However, the data base is sparse for high-burnup fuel rods of U.S. design. Therefore, the staff requested and obtained a code-data comparison for power ramped Mark B rods reported in 1994 (Reference 17). The results showed that the comparison was favorable for the COPERNIC code. In addition, the staff noted in an RAI (Reference 2) that the COPERNIC model did not appear to bound FGR data for urania-gadolinia rods. FCF's response (Reference 3) was to add a multiplier to the temperatures calculated for these rods, which resulted in bounding FGR calculations. The staff considers that this modification is acceptable for the COPERNIC code.

Based on the consistent results between the COPERNIC and FRAPCON-3 codes, the staff concludes that the FGR model in the COPERNIC code is acceptable.

4.0 CLADDING CORROSION AND HYDRIDING MODELS

The waterside corrosion models in COPERNIC are used to predict corrosion during normal operation, are used as input to LOCA analyses, and account for clad thinning in mechanical analyses. The waterside cladding corrosion model for M5 cladding is formulated in a standard way, with pre-transition and post-transition corrosion relationships. The M5 model consists of a pre-transition parabolic rate relationship with an Arrhenius temperature dependence, and a simple post-transition rate relationship, with an Arrhenius temperature dependence. The M5 model coefficients for pre- and post-transition are different from those previously approved in Reference 18 because additional corrosion data have been applied. The transition oxide layer thickness for M5 is near the commonly used value of 2.0 microns for zircaloy.

The FRAPCON-3 code does not have a corrosion model for M5 cladding because this is a new proprietary cladding material used exclusively for FCF fuel designs. However, FRAPCON-3 does have a corrosion model (developed for the Electric Power Research Institute) for zircaloy-4 that has been compared to the COPERNIC model for zircaloy-4 corrosion. The FCF prediction of the corrosion rate for M5 is about ½ to ⅓ of the value predicted by the FRAPCON-3 zircaloy-4 corrosion model. The COPERNIC predicted values for M5 cladding are also about ½ to ⅓ of those observed for FCF zircaloy-4 cladding. The reduced corrosion rate predicted by the COPERNIC M5 corrosion model has been demonstrated to be consistent with in-reactor data for M5 cladding, up to a rod-average burnup of 62 GWd/MTU, i.e., the maximum observed corrosion is about ½ to ⅓ of that for low-tin zircaloy-4 in similar conditions.

Examination of the M5 data from 28 fuel rods from 10 plants (approximately 78 measurements from operation of 1 to 6 cycles) shows that only one data point exists at a rod-average burnup of 62 GWd/MTU and this is from a low duty operational plant. Past experience has shown that fuel rod corrosion is greatest in high duty plants, particularly at high burnup. FCF has provided M5 corrosion data from four high duty plants from Europe with a maximum rod-average burnup of 40 GWd/MTU and have committed to obtain further oxide data at high burnups (Reference 18). It is expected that the corrosion level for M5 cladding will be significantly less than the 100 micron oxide thickness limit for corrosion at rod-average burnups of 62 GWd/MTU even for the high duty plants based on the current M5 data. Based on FCF's commitment to continuously collect corrosion data and use the conservative model, the staff concludes that the M5 corrosion model is acceptable for the COPERNIC code.

The hydrogen pickup fraction recommended for the M5 cladding in COPERNIC is less than the pickup fraction used in FRAPCON-3 for zircaloy-4. The FRAPCON-3 pickup fraction for zircaloy-4 in PWRs is based on a relatively large database of high-exposure U.S. PWR fuel rod cladding. The COPERNIC hydrogen pickup model is consistent with the FCF M5 data base. Based on the conservative way that it models the M5 data, the staff concludes that the M5 hydrogen pickup model is acceptable for the COPERNIC code.

5.0 FUEL DENSIFICATION AND SWELLING MODELS

The fuel densification and swelling models in COPERNIC are important for thermal (LOCA and fuel melting) and cladding strain analyses. The modeling of fuel densification and solid swelling in COPERNIC are included together as one model for the Integrated Dry Route (IDR) and Ammonium Di-Uranate (ADU) fuel employed by FCF in the U.S. FCF also has a separate densification and swelling model for the Ammonium Uranyl Carbonate (AUC) fuel but this fuel is not used commercially and there are no plans for its use in U.S. plants. The maximum fuel densification is determined by FCF in accordance with the recommendation in Regulatory Guide 1.126 (Reference 19). A comparison of the predicted results from COPERNIC (IDR/AUC) and FRAPCON-3 for densification and swelling versus burnup shows that the densification kinetics of the two models are very similar but the COPERNIC solid swelling rate is 15 percent (relative) lower than that predicted by FRAPCON-3. The COPERNIC solid swelling rate is also slightly lower than the rate indicated by the high burnup swelling data used for verification of FRAPCON-3. This will result in a higher burnup level at which hard contact between the fuel and cladding is achieved which is conservative for fuel temperature analyses, but is non-conservative for the cladding strain analysis. This may partially explain why COPERNIC predicts lower clad strain than FRAPCON-3, particularly, at moderate burnups where the fuel-clad gap is closing.

The gaseous swelling model is only used by COPERNIC for thermal analyses and not for the cladding strain analysis. The code comparisons to the thermal data included the use of the gaseous swelling model so that use of the swelling model for thermal predictions is justified. The gaseous swelling model was also used in the prediction of most of their cladding strain data which suggests that it should also be used in their analysis of the 1 percent strain limit. FCF indicated that the strain data used for COPERNIC validation with gaseous swelling came from rods that were ramped to power and held for 1 to 12 hours while the typical transient for the 1 percent strain is a ramp to power that results in immediate scram, i.e., maximum power is for 1 to 2 minutes or less. FCF stated that the elimination of gaseous swelling was justified for this transient because of the short duration of the transient. The expected time frame for these transients will be less than the kinetics of gaseous swelling, and gaseous swelling will be negligible. The staff agrees with this explanation.

Based on the use of conservative models that are consistent with the RG, the staff concludes that the fuel densification and swelling models are acceptable for the COPERNIC code.

6.0 MECHANICAL MODELS

6.1 Modeling

The modeling of mechanical fuel rod behavior by COPERNIC assumes that the pellet is solid (no fuel creep) and the fuel strain determines the amount of elastic-plastic strain in the cladding when hard contact between the fuel and cladding is achieved. Hard contact is initiated when the voids created by the fuel relocation due to the outward movement of fuel fragments are completely consumed by the negative strain due to fuel swelling and thermal expansion. The total fuel strains are calculated from solid swelling, gaseous swelling, densification, thermal expansion, relocation and negative strain models. It is noted that the gaseous swelling model will not be used by COPERINC to predict cladding strains because the use of this model significantly overpredicts some measured cladding strains from fuel rods that were ramped in power. The COPERNIC total cladding strains are calculated from the thermal, creep (slow strain rate), elastic, and high stress creep (fast strain rate) models.

The mechanical model is simplistic in that it assumes a plane strain hypothesis, i.e., cladding deformation in radial and azimuthal directions are independent of the axial stress and strain. The code also assumes isotropic properties of the cladding. Both of these assumptions are not completely accurate for unirradiated stress relief annealed zircaloy-4 fuel cladding, but they are reasonable considering the adequate conservatism in fuel rod mechanical analyses. The cladding loses some of its anisotropic properties as it is irradiated so that it comes closer to isotropic behavior at high burnup.

FCF was questioned by the staff about the mechanical properties for both their zircaloy-4 and M5 cladding types (Reference 2). FCF responded (Reference 3) that at the present time they do not anticipate the use of COPERNIC for licensing their fuel designs with zircaloy-4 cladding in the U.S. The response noted that M5 was expected to be the only cladding used for licensing applications in the COPERNIC code. The M5 mechanical properties of yield strength, ultimate tensile strength, Young's modulus, Poison's ratio, and irradiation growth used in COPERNIC are the same as those approved in the M5 topical report (Reference 18) and, therefore, are acceptable for applications in COPERNIC.

6.2 Irradiation Creep

The M5 creep model in COPERNIC has been modified from that provided in the M5 topical report (Reference 18); however, the differences in predicted creepdown are not significantly different between the two models, particularly within the first 500 days of irradiation when fuel-clad gap closure takes place. The COPERNIC creep model has added a thermal creep component and an irradiation creep component, and the latter component is the most dominant for in-reactor creep (> 95 percent creep is irradiation creep).

The in-reactor creepdown data used to verify the COPERNIC creep model is the same as used in the Reference 14 submittal with the exception that data from two additional rods recently examined at poolside are added to the database. However, the creep database is still very small, with data from only 6 fuel rods with 1 and 2 cycles of operation and 2 rods with 3 cycles of operation. There are several measurements from each fuel rod, but no description of the rod to rod variability that is observed in creep data due to fabrication variability. FCF also presented

data from 2 additional rods with 3 cycles of operation that provided a small amount of creepdown data at the rod ends where fuel clad contact had not occurred due to low burnup and swelling. The majority of the axial length of the 3 cycle rods had fuel cladding contact and cannot be used as a measurement of cladding creepdown. A comparison of the M5 creep model from COPERNIC to the in-reactor creepdown data shows a relatively good fit.

FCF proposes to use the uncertainty from their zircaloy-4 creep model for the M5 creep model uncertainties. This uncertainty appears to be conservative because it bounds a great majority of the M5 creepdown data points. The staff considers that the use of the zircaloy-4 creep uncertainties for M5 creep model is conservative and reasonable. Based on the conservative uncertainty and good data fit, the staff concludes that the irradiated creep model for M5 in COPERNIC is acceptable for licensing applications.

6.3 High Stress Creep Model

FCF has also proposed a high stress model for M5 creep in COPERNIC. The main application of this model in the code is to determine stress relaxation when the fuel and cladding are in hard contact. For the situation of hard fuel-cladding contact, the fuel strain determines the total elastic and uniform plastic cladding strain. The high stress creep model is used to determine the rate of stress relaxation and the ratio of plastic to elastic strain. The staff reviewed the model and considered that it is conservative and reasonable. Based on the conservatism, the staff concludes that this model is acceptable for the COPERNIC code.

6.4 Comparison of Code Versus Data

FCF provided several comparisons of code predictions of cladding permanent strain to measured permanent strains from test fuel rods that have been power-ramp tested. However, all but one of these test fuel rods were clad with the older zircaloy-4 material and only one test rod used was clad with the M5 cladding. In addition, these tests involved power ramps that lasted for several hours. This is in contrast to the 1-percent cladding strain analysis performed by FCF, which is intended for anticipated transients that usually last only for a few minutes. The COPERNIC comparison of the predicted permanent strain to the measured strain for the ramped rod with M5 cladding (with a 12 hour hold-time) shows very good agreement. FCF has also provided comparisons of the high stress creep model to permanent strain data from sections of M5 cladding from irradiated fuel rods that were pressure tested at high stresses in out-of-reactor tests. These results are not considered to be integral tests of the code's ability to predict permanent strain in-reactor, but do show that the high stress creep model predicts this data well with a small amount of conservatism.

FCF was asked by the staff whether the comparisons of the COPERNIC predictions to the power ramped rods presented in Sections 6 and 7 of the submittal used the gaseous swelling model in COPERNIC. FCF responded that the gaseous swelling model was used. FCF was further asked by the staff why it was reasonable to use the gaseous swelling model for analyzing the power ramped test rods, but not so to use the gaseous swelling model for the 1-percent strain analysis in anticipated transients. FCF responded that the anticipated transients only lasted a few minutes duration while the test rods in power ramps had hold times of several hours. FCF explained that the gaseous swelling model is important for ramp hold times of several hours, but the kinetics of gaseous swelling is too slow for it to be an important

phenomena for transients that last only a few minutes. The staff acknowledges that there is a technical basis for the position that the gaseous swelling kinetics may be slow for anticipated transients, but notes that there is little data to confirm this assertion. Based on the conservative models and satisfactory comparisons between the code and data, the staff concludes that the mechanical models in the COPERNIC code are acceptable for licensing applications.

7.0 LICENSING APPLICATIONS

7.1 Power-to-Melt Analysis

The differences between COPERNIC and FRAPCON-3 fuel thermal conductivity models at high temperatures (> 2000 K) lead to differences in calculated power-to-melt results. Compared to the COPERNIC code at the BOL, the power-to-melt results drop about 5 to 7 percent when the NFI fuel conductivity model from the FRAPCON-3 code is used. Also, due to the lower thermal conductivity burnup degradation of the COPERNIC code, the difference between COPERNIC and FRAPCON-3 with the NFI model increases to about 9 to 10 percent at burnups of 20 to 30 GWd/MTU. The NFI thermal conductivity model compares well with the Ronchi (Reference 6) high-temperature data. FCF noted the trend of reductions in thermal conductivity as burnup increases. FCF believes that the combined effect of the conservatism in the UO_2 fuel melting model and the conservatism in the fuel centerline temperature predictions is enough to offset the effect of the higher thermal conductivity as burnup increases (Reference 22). The staff generally agrees with this finding. In examining the results, the staff considers that the power-to-melt analysis is close to best estimate results at burnups greater than 10 GWd/MTU.

The fuel melting analysis predicts conservative results at BOL, and close to best estimate results when burnups exceed 10 GWd/MTU. Therefore, based on the conservative models and the comparisons with the audit code, the staff concludes that the power-to-melt analysis is acceptable for the COPERNIC code.

7.2 Stored Energy

COPERNIC is used to calculate the initial fuel stored energy for LOCA analyses to verify that fuel designs meet Appendix K requirements. The fuel stored energy is approximately proportional to the fuel volume-average temperature (VAT). Sample COPERNIC "bounding" values for the fuel volume-average temperature as a function of burnup and linear heat generation rate (LHGR) are plotted for the Mark B design (UO2 cycles) in Figure 12-21 of Reference 1. The COPERNIC results show that VATs are at a maximum between rod-average burnups of 30 to 35 GWd/MTU.

The staff requested (Reference 2) and obtained (Reference 3) the power histories and axial power shapes used to make this plot, and repeated the calculations with various thermal conductivity models inserted into FRAPCON-3. The FRAPCON-3 code audit analysis used the same input as used for COPERNIC but used three recently published UO_2 conductivity models (References 4, 5, and 8) to predict VAT. The FRAPCON-3 audit results from all three conductivity models predicted similar values for VAT, and stored energy values that were 10 to 19 percent greater than those predicted by COPERNIC at burnups > 5 GWd/MTU.

The three models used in the FRAPCON-3 were the NFI, Halden, and the EDF models. The NFI thermal conductivity model (Reference 8) has been shown to provide good agreement with Halden high burnup centerline data and ex-reactor measured thermal conductivity data from high burnup fuel published in the open literature (References 9 and 10). The Halden thermal conductivity model is primarily based on Halden measurements of fuel centerline temperatures from high burnup rods. Some of the Halden high burnup rods were irradiated in commercial reactors and then re-fabricated with thermocouples and then irradiated in the Halden reactor. The recently published thermal conductivity model by the French utility EDF is primarily based on ex-reactor measurements of thermal conductivity from high burnup fuel that resulted from the Nuclear Fuel Industry Research (NFIR) program (sponsored by industry) and it should be noted that this model predicts the highest VATs of the three models. The NFIR data has not been published in enough detail that it can be used by PNNL for model verification nor is the detailed data available to the NRC. Therefore, the EDF model is based on a completely independent database from that used to develop the NFI and Halden models, but the data base is not available to PNNL for examination. The databases used to develop the NFI and Halden models are not the same but some of the data used for each overlap. The reason for the higher VATs predicted by the three recent thermal conductivity models is that they show a stronger degradation in thermal conductivity with increasing burnups.

Because the FCF VAT plots in the submittal show VAT increasing with burnup, the staff asked an additional question about whether LOCA peak clad temperatures (PCTs) remain limiting at BOL for FCF fuel (Reference 20). FCF responded (Reference 21) that this will be determined when the COPERNIC code is approved and then the LHGR limits for LOCA will be determined accordingly. FCF further stated that for Westinghouse and Combustion Engineering plants, the local peaking factor is restricted so that BOL PCTs remain limiting. However, a new LHGR limit may be required for these plants when the COPERNIC code is used. COPERNIC and FRAPCON-3 audit code calculations both show that the maximum stored energy is no longer greatest at BOL but is greatest at mid-life burnups of about 30 to 35 GWd/MTU. This is important because most approvals for fuel performance audit codes in the past have been based on calculations that show LOCA PCTs are greatest at BOL where fuel rod properties beyond BOL do not have to be considered.

In addition, FCF has proposed in their response (Reference 22) that they reduce the hold-time of the power transient (they currently use a 12 hour hold-time) used to initialize the LOCA stored energy and rod pressures. They propose to use the plant specific technical specification that limits the amount of time (typically in the range of 15 minutes to 4 hours) that the fuel can operate in excess of the specified acceptable fuel design limits for the power transient hold-times used to initialize LOCA conditions.

The 12 hour hold-time is a legacy from the original approval of the TACO3 fuel performance code (Reference 24). The TACO3 code required a long hold-time because the FGR model in this code did not adequately predict FGR for short time transients, but adequately predicted FGR for steady-state power operation. Consequently, the application of the TACO3 code to transient power conditions required long hold-times for the code to allow for equilibrium FGR to be achieved. The COPERNIC code appears to adequately predict FGR during power transients. Therefore, it is not necessary to continue the practice of using abnormally long hold-times for accident initiation unless justified for the accident type. The staff concludes that

the use of technical specification limits to determine the amount of hold-time for LOCA initial conditions is acceptable for the COPERNIC code.

Based on the consistent results with the audit code and the conservative models, the staff concludes that the stored energy analysis for LOCA initial conditions is acceptable for the COPERNIC code.

7.3 Fuel Rod Internal Pressure

FCF provided an example of the COPERNIC results from a fuel rod internal pressure analysis of the Mark B design. An audit calculation was performed with FRAPCON-3 using the same input, and the results showed that FRAPCON-3 predicted slightly greater pressures than COPERNIC except near the end-of-life, where the two predictions were nearly identical. This is considered acceptable because most fuel today is licensed for rod-average burnups greater than 55 GWd/MTU where the two codes predict similar results. The staff concludes that the COPERNIC code is acceptable for application to fuel rod pressure analyses.

7.4 Clad Strain

Section 4.2 of the Standard Review Plan (SRP) suggests a 1 percent strain limit (elastic plus uniform plastic) for normal and anticipated transient fuel operation (Reference 23). In general, anticipated transients provide the greatest prediction of clad strain, and are therefore used for the1 percent strain analysis. FCF provided examples of COPERNIC calculated power limits for their clad strain analysis of the Mark B design as a function of burnup results in Figure 12-28 (Reference 1). An audit calculation was performed by the staff with FRAPCON-3 using the same input. A comparison of the COPERNIC and FRAPCON-3 results shows that the two codes are generally in good agreement. This small difference makes it difficult for assessing the ability of either code in performing these calculations because of the lack of in-reactor measured strain data for the relatively fast power ramps (on the order of a few minutes) assumed for this analysis.

Based on its use of conservative models and good agreement with the NRC audit code which predict results that are conservative compared to the staff's independent analysis, the staff concludes that the cladding strain analysis is acceptable for the COPERNIC code.

8.0 CONCLUSIONS

The staff has reviewed FCF's improved fuel performance code, COPERNIC, for the advanced cladding M5 for fuel rod mechanical designs described in BAW-10231P. The staff concludes that the COPERNIC code is acceptable for fuel licensing applications up to a rod average burnup of 62 Gwd/MTU.

Licensees that reference this topical report still need to meet 10 CFR 51.52, "Environmental effects of transportation of fuel and waste"-Table S-4.

9.0 REFERENCES

1. Letter, T. A. Coleman (Framatome Cogema Fuels) to U.S. NRC Document Control Desk, "Topical Report BAW-10231P, COPERNIC Fuel Rod Design Computer Code," September 16, 1999, GR99-191.doc.

2. Letter, Stewart Bailey, NRC, to T. A. Coleman, Framatome Cogema Fuels, "Request for Additional Information - Topical Report BAW-10231P," August 11, 2000.

3. Letter, T. A. Coleman, Framatome Cogema Fuels, to U.S. NRC Document Control Desk, GR01-021.doc, February 5, 2001.

4. W. Wiesenack and T. Tverberg, 2000, "Thermal Performance of High Burnup Fuel - In-Pile Temperature Data And Analysis," in Proceedings of the ANS International Topical Meeting on Light Water Reactor Fuel Performance, Park City, Utah, April 2000, pages 730 to 737.

5. Baron, D. and S. Biz, 2001, "EDF Fuel Thermal Conductivity Model at High Burnup Based on TD Measurements Conducted on the NFIR Irradiated Fuel Wafers, Up to 80 GWd/MTU," Enlarged Halden Meeting on High Burnup Performance, HPR-356, Halden Reactor Project, Halden, Norway.

6. Ronchi, C., M. Shiendlin, M. Musella, and G.J. Hyland, 1999, "Thermal Conductivity of Uranium Dioxide up to 2900 K from Simultaneous Measurement of the Heat Capacity and Thermal Diffusivity," *Journal of Applied Physics*, Vol. 85 no.2, pages 776 to 789.

7. P.G. Lucuta, H.S. Matzke, and I.J. Hastings, "A Pragmatic Approach to Modeling Thermal Conductivity of Irradiated UO_2 Fuel: Review and Recommendations," Journal of Nuclear Materials, Vol 232, pages 155 to 180, 1996.

8. Ohira, K., and N. Itagaki, 1997, "Thermal Conductivity Measurements of High Burnup UO2 Pellet and a Benchmark Calculation of Fuel Center Temperature," Proceedings of the ANS International Topical Meeting on LWR Fuel Performance, Portland, OR, March 2-6 1997, pages 541 to 549.

9. Lanning, D.D., C.E. Beyer, and M.E. Cunningham, 2000, "FRAPCON-3 Fuel Rod Temperature Predictions with Fuel Conductivity Degradation Caused by Fission Products and Gadolinia Additions," in Proceedings of the ANS International Topical Meeting on Light Water Reactor Fuel Performance, Park City, Utah, April 2000, pages 261 to 274.

10. Lanning, D. D, and C. E. Beyer, 2001, "Assessment of Recent Data and Correlations for Fuel Pellet Thermal Conductivity," Presented at Enlarged Halden Program Meeting March 11-16, 2001, HPR-356.

11. Garnier, J. E. and S. Begej, 1979, "Ex-Reactor Determination of Thermal Gap and Contact Conductance Between Uranium Dioxide: Zircaloy-4 Interfaces: Stage I: Low Gas Pressure, " NUREG/CR-0330, PNL-2696, Vol. 1, prepared for the U.S. Nuclear Regulatory Commission by Pacific Northwest Laboratory, Richland, Washington.

12. Garnier, J. E. and S. Begej, 1980, "Ex-Reactor Determination of Thermal Gap and Contact Conductance Between Uranium Dioxide: Zircaloy-4 Interfaces: Stage II: High Gas Pressure," NUREG/CR-0330, PNL-2696, Vol. 2, prepared for the U.S. Nuclear Regulatory Commission by Pacific Northwest Laboratory, Richland, Washington.

13. Wesley, D. A. and M. Yovanovich, "A New Gaseous Gap Conductance Relationship," Nuclear Technology, Vol. 72, January 1986, pages 70-74.

14. BAW-10228P,1998, "SCIENCE," Topical Report, February 1998.

15. American Nuclear Society (ANS), 1982, "Method for Calculating the Fractional Release of Volatile Fission Products from Oxide Fuel, ANSI/ANS-5.4-9182," ANS 5.4 of the Standards Committee of the American Nuclear Society.

16. Forsberg, K. and A. R. Massih, 1985, "Diffusion Theory of Fission Gas Migration in Irradiated Nuclear Fuel UO_2," J. of Nuc. Mater., Vol. 135, pages 140-148.

17. Wesley, D. A., K. Mori, and S. Inoue, 1994, "A Mark BEB Ramp Testing Program presented in the proceedings of the 1994 ANS/ENS International Topical Meeting on Light Water Reactor Fuel Performance, West Palm Beach, Florida, Page 343, American Nuclear Society.

18. Framatome Cogema Fuels, November 1999, "Evaluation of Advanced Cladding and Structural Material (M5) in PWR Reactor Fuel," BAW-10227P-A, Framatome Cogema Fuels, Lynchburg, Virginia.

19. U.S. Nuclear Regulatory Commission, 1978, "An Acceptable Model and Related Statistical Methods for the Analysis of Fuel Densification," Regulatory Guide 1.126, Revision 1, U.S. Nuclear Regulatory Commission, Washington D.C.

20. Letter, Stewart Bailey, NRC, to T. A. Coleman, Framatome ANP, Request for Additional Information - Chapter 13 of Framatome Topical Report BAW-10231P, May 14, 2001.

21. Letter, J. F. Mallay, Framatome ANP, to U.S. NRC Document Control Desk, NRC 02-010, February 5, 2002.

22. Letter, J. F. Mallay, Framatome ANP, to U.S. NRC Document Control Desk, NRC:01:033, July 27, 2001.

23. U.S. Nuclear Regulatory Commission, July 1981, "Section 4.2, Fuel System Design." In Standard Review Plan for the Review of Safety Analysis Reports for Nuclear Power Plants - LWR Edition, NUREG-0800, Rev. 2, U.S. Nuclear Regulatory Commission, Washington, D.C.

24. Wesley, D. A., and K. J. Firth, October 1989, "TACO3 Fuel Pin Thermal Analysis Code," BAW-10162P-A, Babcock & Wilcox, Lynchburg, Virginia.

Principal Contributor: S. Wu

Date: April 18, 2002

Note from the preparer:

In Paragraph 5.0 of the SER, it is stated:

"A comparison of the predicted results from COPERNIC (IDR/AUC) and FRAPCON-3 for densification and swelling versus burnup shows that the densification kinetics of the two models are very similar but the COPERNIC swelling rate is 15 percent (relative) lower than that predicted by FRAPCON-3."

This paragraph should read, as indicated on the Safety Evaluation Report cover letter:

"A comparison of the predicted results from COPERNIC (IDR/ADU) and FRAPCON-3 for densification and swelling versus burnup shows that the densification kinetics of the two models are very similar but the COPERNIC swelling rate is 15 percent (relative) lower than that predicted by FRAPCON-3."

Preparer	FP Faucher	07/22/2002
	Signature	Date
Manager	D.M. Brown	7/29/02
	Signature	Date
Regulatory Affairs Director		7/26/02
	Signature	Date

RAI Responses dated 4/18/2003, 7/17/2002 and 4/26/2002

FRAMATOME ANP

An AREVA and Siemens Company

FRAMATOME ANP, Inc.

April 18, 2003
NRC:03:027

Document Control Desk
ATTN: Chief, Planning, Program and Management Support Branch
U.S. Nuclear Regulatory Commission
Washington, D.C. 20555-0001

Final Responses to RAIs on Chapter 13 of BAW-10231P

Ref.: 1. Letter, Stewart Bailey (NRC) to T. A. Coleman (Framatome ANP), "Request for Additional Information – Chapter 13 of Framatome Topical Report BAW-10231P (TAC No. MA9783)," May 14, 2001.

Ref.: 2. Letter, Drew Holland (NRC) to James Mallay (Framatome ANP), "Request for Additional Information – BAW-10231P, Chapter 13, 'COPERNIC MOX Applications,' " April 25, 2002.

Ref.: 3. Letter, James F. Mallay (Framatome ANP) to Document Control Desk (NRC), "Partial Response to RAI," NRC:01:033, July 27, 2001.

Ref.: 4. Letter, James F. Mallay (Framatome ANP) to Document Control Desk (NRC), "Partial Response to RAI on Chapter 13 of BAW-10231P," NRC:02:021, April 26, 2002.

Ref.: 5. Letter, James F. Mallay (Framatome ANP) to Document Control Desk (NRC), "Partial Response to RAI on Chapter 13 of BAW-10231P," NRC:02:038, July 17, 2002.

References 1 and 2 provided requests for additional information (RAIs) on the MOX applications of the COPERNIC topical report. References 3 through 5 contained responses to all but two of the questions in those RAIs.

Attached please find responses to the two remaining questions.

Framatome ANP considers some of the material contained in the attachments to be proprietary. The affidavit submitted with Reference 3 satisfies the requirements of 10 CFR 2.790(b) to support withholding of the information from public disclosure. Attachment 1 is the proprietary version of the RAI responses. Attachment 2 is the non-proprietary version. After the SER is received, Framatome ANP will incorporate all the enclosed material into the approved version of BAW-10231P.

Very truly yours,

Sandra M. Sloan for

James F. Mallay, Director
Regulatory Affairs

Enclosures

cc: D. G. Holland (w/enclosures)
Project 728

FRAMATOME ANP, Inc.
3315-A Old Forest Road, P.O. Box 10935 - Lynchburg, VA 24506-0935
Tel.: 434-832-3000 Fax: 434-832-2953 www.us.framatome-anp.com

Attachment 1 (proprietary version) with the RAI responses has been removed.
Attachment 2 (the non-proprietary version of Attachment 1) follows.

RESPONSE TO OUTSTANDING REQUESTS FOR ADDITIONAL INFORMATION

TOPICAL REPORT BAW-10231P, CHAPTER 13

"COPERNIC MOX APPLICATIONS"

Below are responses to the outstanding 1st- and 2nd-Round questions received on the COPERNIC MOX Addendum.

Round 1, Question 8:

The integral MOX experiments provided, where centerline temperatures are measured, to verify the COPERNIC integral thermal predictions of MOX fuel rods are limited to very low burnup levels, i.e., less than 5 GWd/MTU. Please provide COPERNIC predictions of at least three of the following Halden MOX instrumented assemblies, IFA-597.4/.5/.6, IFA-606, IFA-610, and IFA-648.1, that achieved burnups of approximately 24 GWd/MTM to 57 GWd/MTM, or suggest other Halden MOX instrumented assemblies. Please justify the reasons for eliminating some of the data and/or assemblies for COPERNIC comparisons and the reasons for selecting others (this should be discussed with the NRC reviewer prior to issuing a response to the request for additional information). Also, rod pressures due to fission gas release were measured for two experimental Halden MOX fuel rods in IFA-597.4/.5/.6. COPERNIC predictions of rod pressure are also needed, where appropriate.

Response:

Framatome ANP considers the lower-burnup experiment IFA-597.4/.5/.6 to be atypical of MIMAS fuel performance. The follow-on experiment IFA-597.7 showed very high fission gas release at the beginning of the irradiation, as indicated in Halden Status Report HR1110. This level is unusual and not consistent with other experiments.

Therefore, Framatome ANP selected the experiments IFA-606, IFA-610.2, IFA-610.4, and IFA-648.1, which are more representative of MIMAS fuel, to demonstrate the adequacy of the COPERNIC thermal predictions. Measured versus predicted central temperatures for these four experiments are provided in Figures 1 through 4B.

The fission gas release for IFA-606, rodlet 3, which yielded the highest release fraction, was predicted[1] to be 15.9% compared to the measured value of 12.2%.

It is concluded that COPERNIC provides very good agreement with the measured data.

Round 2, Question 5:

The application of COPERNIC for MOX temperature predictions assumes that the uncertainty for MOX is the same as for UO_2 fuel temperature predictions. This assumption is questionable, particularly at higher burnups (>25 GWd/MTU) because there are no centerline temperature data and no thermal diffusivity data for MOX fuel at these burnups. In addition, there may be further reduction in MOX thermal conductivity at higher burnups if the MOX becomes more hypostoichiometric with increasing burnup (see Question 4 above). Please justify why the COPERNIC calculated temperature uncertainty for UO_2 can be applied to MOX at burnups greater than 25 GWd/MTU without data to confirm this assumption.

Response:

As shown in the attached figures, COPERNIC provides very good predictions of high burnup MOX fuel temperatures. Since the temperature uncertainty for these high burnup MOX experiments is

[c, e]

Figure 1

IFA606 Measured and Predicted Peak Temperatures

[d]

Figure 2

IFA610.2 Measured and Predicted Peak Temperatures

[d]

Figure 3

IFA610.4 Measured and Predicted Peak Temperatures

[d]

Figure 4A
IFA-648.1 Experiment (Rod N12)
Measured and Predicted Peak Temperatures

[d]

Figure 4B
IFA-648.1 Experiment (Rod P16)
Measured and Predicted Peak Temperatures

[d]

References

1. L.C. Bernard et. al., *An Efficient Model for the Analysis of Fission Gas Release*, Journal of Nuclear Materials 302 (2002), 125-134.

bcc: NRC:03:027
L. C. Bernard
D. M. Brown
R. E. Collingham
J. J. Cudlin
B. J. Delano
F. P. Faucher
J. D. Gale
G. E. Hanson
R. L. Hame
P. J. Henningson
J. A. Hoerner
J. S. Holm
W. F. Jones
J. A. Klingenfus
L. L. Losh
J. F. Marrot
C. F. McPhatter
G. A. Meyer
E. Morel (FFJC)
L. D. O'Dell
R. S. Reynolds
J. R. Tandy
J. N. Vemay
P. Vesco
D. A. Wesley
R. D. Williamson

FRAMATOME ANP

July 17, 2002
NRC:02:038

Document Control Desk
ATTN: Chief, Planning, Program and Management Support Branch
U.S. Nuclear Regulatory Commission
Washington, D.C. 20555-0001

Partial Response to RAI on Chapter 13 of BAW-10231P

Ref.: 1. Letter, Drew Holland (NRC) to James Mallay (Framatome ANP, Inc.), "Request for Additional Information – BAW-10231P, Chapter 13, 'COPERNIC MOX Applications,' " April 25, 2002.

Ref.: 2. Letter, T.A. Coleman (Framatome ANP) to Document Control Desk (NRC), GR00-088, July 31, 2000.

In Reference 1, the NRC issued a request for additional information (RAI) on BAW-10231P, Chapter 13, "COPERNIC MOX Applications." The responses to all but Question 5 are contained in the attachments to this letter. The response to Question 5 will be provided at a later date. Attachment 1 contains the proprietary version of the response and Attachment 2 the non-proprietary.

Framatome ANP considers some of the material in these responses to be proprietary. The affidavit provided with Reference 2, which transmitted Chapter 13 of BAW-10231 (on which this RAI is based), satisfies the requirements of 10 CFR 2.790(b) to support the withholding of this information from public disclosure.

Very truly yours,

James F. Mallay, Director
Regulatory Affairs

Attachments

cc: D. G. Holland
Shih-Liang Wu
Project 693

Framatome ANP, Inc.

2101 Horn Rapids Road
Richland, WA 99352
Tel: (509) 375-8100
Fax: (509) 375-8402

Attachment 1 (proprietary version) with the RAI responses has been removed.
Attachment 2 (the non-proprietary version of Attachment 1) follows.

PARTIAL RESPONSE TO 4/25/2002 REQUEST FOR ADDITIONAL INFORMATION

TOPICAL REPORT BAW-10231P, CHAPTER 13

"COPERNIC MOX APPLICATIONS"

Below are responses to the 2nd-Round questions received on the COPERNIC MOX Addendum, less Question 5, which will be provided at a later date.

1. **Please provide densification and swelling data that demonstrate that the UO_2 densification and swelling models may be applied to the Framatome fabricated MOX using the MIMAS process from ADU powder. Also provide information on how Framatome assures that the PuO_2 powder supplied by DOE will behave similarly to that previously fabricated by Framatome and applies to the densification and swelling MOX data supplied to NRC in this submittal.**

Response:

Figure 1 provides the measured hydrostatic density versus burnup for MOX fuel fabricated from ADU powder and UO_2 fuel.

The PuO_2 powder supplied by the DOE will be further processed by Duke Cogema Stone and Webster in order to remove impurities. The final PuO_2 powder used as feed to the Micronized MASter blend (MIMAS) process will be produced using the same processes and specifications as the material produced in Europe.

The weapons grade (WG) MOX pellet specification, developed based upon the current specification used in Europe, ensures the similar performance of MOX fuels and applicability of the European experience base. This specification is derived from the FRA-ANP (France) specification for MOX pellets used with COGEMA-supplied MOX fuel in Europe using the Micronized MASter blend (MIMAS) process. Since the MIMAS process will be replicated in the U.S. fabrication facilities for the Plutonium Disposition program, this European experience is directly applicable.

The overall MOX pellet microstructure is dominated by the UO_2 powder characteristics and will be produced by the same process and feed UO_2 material. Limits on O/U (oxygen/uranium) ratio, density, and resinter densification are identical to those of the European experience. Impurity lists are also similar; however, limits on some additional elements such as gallium are addressed in the WG specification.

The grain size, particle size, and particle distribution will be identical since the production process is the same in terms of blender operation, size of sieves, pressing conditions, and sintering conditions. The maximum size and Pu content of the particles is controlled through a milling and sieving operation followed by a sintering process that induces diffusion of the PuO_2 bearing particles into the UO_2 lattice. Control of the process is verified through metallographic examination and autoradiography of a representative number of samples from

each batch of pellets. These examinations provide measurements of the effective particle size, the grain size and the plutonium content. Alternatively, these parameters can be measured using Electron Probe Micro Analysis (EPMA) during qualification, with the process monitored during fabrication using metallography and autoradiography.

Due to the different isotopics, the weapons grade material will have an equivalent fissile content approximately 50% greater than that of the reactor grade material. Therefore, the master mix ratio will be 80/20 (UO_2/PuO_2) for the weapons grade material, rather than the 70/30 ratio employed for reactor grade material, to ensure that the fissile content of the Pu rich particles remains the same as the reactor grade material. Since the particle size and distribution within the pellet are the same, the distribution of fissile material within the pellet will be the same. Thus, the fission density and the fission product inventory will be the same in reactor grade and weapons grade MOX fuels, and the pellet thermal-mechanical behavior – fission gas release, transient response, densification and swelling – will be replicated and consistent with the European experience base.

2. Please compare COPERNIC predicted MOX radial Pu distributions at different burnup levels to measured radial Pu distributions at the same burnup levels. Also compare COPERNIC predicted MOX radial burnup distributions to those measured radial burnup distributions at different burnup levels. List the initial starting Pu distributions for the data.

Response:

COPERNIC does not predict the Pu distribution. The pellet radial power profiles and consequently the radial plutonium profiles are inputs to COPERNIC calculated by the neutron transport code APOLLO-II [1,2]. As discussed in the response to 1st-round Question 1, COPERNIC contains internal tables of the fuel pellet normalized radial power profile inputs.

The radial burnup profile is related to the radial Pu distribution, and several MOX fuel radial burnup profile measurements have been inferred from Neodymium measurements made using Electron Probe Micro Analyses (EPMA).

Comparisons of these measured and predicted normalized radial burnup profile comparisons are provided for several MOX pellets in Figures 2 through 8. Note that at low burnup, the Neodymium content is low, resulting in a low Nd/background count and corresponding higher scatter. The heterogeneity of local Pu-rich spots also decreases with burnup.

3. Please supply any new data that have been obtained since the issuance of the topical report related to MOX behavior/properties such as fission gas release, fuel swelling, thermal conductivity, and thermal expansion.

Response:

Figures 9 through 12 provide the available data. These figures include recently obtained data for MIMAS ADU fuel (~55 GWD/t rod average burnup) and MIMAS AUC fuel (60 GWD/t) that have been irradiated for four or five cycles.

4. The COPERNIC thermal conductivity model does not appear to account for changes in stoichiometry of MOX with irradiation. This is of concern because it has been proposed in the literature (Duriez et al., J. Nuc Mater. 277: 143 – 158) that MOX fuel may become more hypostoichiometric due to an increase in oxygen vacancies with increasing burnup and, therefore, result in more thermal conductivity degradation in addition to the degradation due to irradiation and fission products. Please provide data and analysis demonstrating that the COPERNIC assumption of no thermal conductivity degradation due to MOX stoichiometry changes with burnup is valid.

Response:

[b, c]

6. The following additional input data are needed for PNNL to perform audit analyses of COPERNIC example results of MOX licensing analyses.

The axial power shapes used for steady-state power operation for example licensing analyses were not found in the topical report. Please provide these axial power shapes in electronic format if possible. Please provide the radial power shapes as a function of burnup for these analyses.

What is the assumed stoichiometry of the MOX for these analyses and how does this compare to the specification on stoichiometry for MOX for commercial application? Do these analyses include possible changes in stoichiometry with burnup (see Question 4 above) and, if so, what are the assumed changes?

Response:

The axial power shapes used in the Chapter 13 examples are provided in Table 1. The transient power shapes have been included for convenience. Pellet radial power profiles were provided in the response to 1st-round Question 1.

The oxygen/metal ratio of the MOX fuel is assumed to be 2.00 in these analyses. The specification limit on O/M ratio, calculated as O/(U + Pu + Am), is 1.98 to 2.01 (see the response to 1st-round question 2). [b, c]

Figure 1
MOX and UO_2 Hydrostatic Density versus Burnup

[c]

Figure 2
Comparison of Measured and Predicted Normalized Radial Burnup Profiles

[c]

Figure 3
Comparison of Measured and Predicted Normalized Radial Burnup Profiles

[c]

Figure 4
Comparison of Measured and Predicted Normalized Radial Burnup Profiles

[c]

Figure 5
Comparison of Measured and Predicted Normalized Radial Burnup Profiles

[c]

Figure 6
Comparison of Measured and Predicted Normalized Radial Burnup Profiles

[c]

Figure 7
Comparison of Measured and Predicted Normalized Radial Burnup Profiles

[c]

Figure 8
Comparison of Measured and Predicted Normalized Radial Burnup Profiles

[c]

Figure 9
MOX Measured End of Life Internal Pressure

[c]

Figure 10
MOX Fission Gas Release

[c]

Figure 11
MOX Fuel Column Growth

[c]

Figure 12
MOX Fuel Densification and Swelling
And Comparison with UO_2

[c]

Table 1
MOX Fuel Normalized Power Distributions

[b]

Table 1 (continued)
MOX Fuel Normalized Power Distributions

[b]

Table 1 (continued)
MOX Fuel Normalized Power Distributions

[b]

References

1. Stewart N. Bailey (NRC) to T. A. Coleman (Framatome Cogema Fuels), *Safety Evaluation of Topical Report BAW-10228P, "SCIENCE" (TAC No. MA4599)*, October 26, 1999.

2. Stuart A. Richards (NRC) to T. A. Coleman (Framatome Cogema Fuels), *Correction to Safety Evaluation of Topical Report BAW-10228P, "SCIENCE" (TAC No. MA4599)*, May 24, 2000.

bcc: NRC:02:038
L. C. Bernard
D. M. Brown
R. E. Collingham
J. J. Cudlin
B. J. Delano
F. P. Faucher
J. D. Gale
G. E. Hanson
R. L. Harne
P. J. Henningson
J. A. Hoerner
J. S. Holm
W.F. Jones
J. A. Klingenfus
L. L. Losh
J. F. Mallay
J. F. Marrot
C. F. McPhatter
G. A. Meyer
E. Morel (FFJC)
L. D. O'Dell
R. S. Reynolds
J. R. Tandy
J. N. Vernay
P. Vesco
D. A. Wesley
R. D. Williamson

FRAMATOME

April 26, 2002
NRC:02:021

Document Control Desk
ATTN: Chief, Planning, Program and Management Support Branch
U.S. Nuclear Regulatory Commission
Washington, D.C. 20555-0001

Partial Response to RAI on Chapter 13 of BAW-10231P

Ref.: 1. Letter, Stewart Bailey (NRC) to T. A. Coleman (Framatome ANP), "Request for Additional Information – Chapter 13 of Framatome Topical Report BAW-10231P (TAC No. MA9783), May 14, 2001.

Ref.: 2. Letter, James F. Mallay (Framatome ANP) to Document Control Desk (NRC), "Partial Response to RAI," NRC:01:033, July 27, 2001.

Ref.: 3. Letter, T. A. Coleman (Framatome ANP) to Document Control Desk (NRC), GR00-088, July 31, 2000.

In Reference 1 the NRC issued a request for additional information (RAI) on BAW-10231P, "COPERNIC Fuel Rod Design Code." This RAI included questions concerning both the UO2 and the MOX portions of the report. The UO2-related questions were responded to in Reference 2. Responses to the remaining questions, except number 8, for which analyses are still being conducted, are enclosed. Attachment 1 contains the proprietary version of the response and Attachment 2 the non-proprietary.

Framatome ANP considers some of the material in these responses to be proprietary. The affidavit provided with Reference 3, which transmitted Chapter 13 of BAW-10231 (on which this RAI is based) satisfies the requirements of 10 CFR 2.790(b) to support the withholding of this information from public disclosure.

Very truly yours,

James F. Mallay, Director
Regulatory Affairs

Enclosures

cc: D. G. Holland
Shih-Liang Wu
Project 693

Framatome ANP, Inc.

2101 Horn Rapids Road
Richland, WA 99352
Tel: (509) 375-8100
Fax: (509) 375-8402

3315 Old Forest Road P.O. Box 10935 Lynchburg, VA 24506-0935 Tel: 804-832-3000 www.framatech.com

Attachment 1 (proprietary version) with the RAI responses has been removed.
Attachment 2 (the non-proprietary version of Attachment 1) follows.

ATTACHMENT 2

PARTIAL RESPONSE TO 5/21/2001 REQUEST FOR ADDITIONAL INFORMATION

TOPICAL REPORT BAW-10231P, CHAPTER 13

"COPERNIC FUEL ROD DESIGN CODE"

MOX APPLICATIONS

Below are responses to several of the 1st-Round questions received on the COPERNIC MOX Addendum. Responses to Questions 6 & 7 have previously been provided. The response to Question 8 will be provided at a later date.

1. **It is recognized that weapons grade plutonium will be used for MOX for commercial application in the U.S. However, the isotopic plutonium ratios are significantly different between reactor grade (reprocessed LWR fuel) plutonium and weapons grade plutonium. Please provide the plutonium ratios for reactor grade and weapons grade plutonium and; also, the tabular values of pellet radial power profiles to be used for weapons grade plutonium and how these values were determined. If the reactor grade and weapons grade MOX radial profiles are proposed to be similar, provide the calculational results for both MOX types that demonstrate this conclusion.**

Response:

Typical values for fresh reactor grade (RG) and weapons grade (WG) plutonium isotopics are provided in Table 1. These isotopics vary for reactor grade fuel depending upon the reprocessed uranium fuel enrichment, burnup, and decay time.

COPERNIC contains internal tables for MOX fuel pellet normalized radial power profiles. These tables are a function of [d.] .

The maximum weapons-grade plutonium content of any fuel rod to be used in the Plutonium Disposition Program is six weight percent plutonium, and the initial licensed rod-average burnup limit requested will be 50 GWd/t. Radial power profiles for RG and WG MOX fuels are presented in Tables 2a and 2b respectively. These profiles were calculated with the APOLLO-II transport code[1,2].

[b., d.]

2. Please provide the specifications (including nominal values) of oxygen-to-metal (O/M) ratio, PuO_2 particle size, and grain size specified for the U.S. commercial application.

Response:

The weapons grade MOX pellet specification was developed based upon the current specification used in Europe in order to ensure the similar performance of MOX fuels and applicability of the European experience base.

Fabrication will use the COGEMA/BELGONUCLEAIRE-developed Micronized MASter blend (MIMAS) process currently supplying MOX fuel to 32 reactors in Europe. MOX manufactured by the MIMAS process involves blending and milling of UO_2 and PuO_2 powders (master mix) and then dilution of the master mix with more UO_2 to reach the final Pu content. The products of this process are not as homogeneous as the UO_2 pellet on a micro-scale although they approximate to the same condition on a macro-scale. Microscopic examination of MOX pellets shows Pu finely dispersed in a UO_2 matrix and micron size islands of plutonium rich particles. The particles are not pure PuO_2 particles but master mix particles with a maximum Pu content determined by the ratio of UO_2 (80%) to PuO_2 (20%) in the master mix.

The specification for plutonium rich particles states that at least 95% of the plutonium rich particles shall have an effective diameter (square root of the grain surface area) of less than 100 µm, the mean plutonium rich particle distribution shall be less than 50 µm, and no pure plutonium grain shall be greater than 400 µm.

The average grain size of the UO_2 matrix shall be greater than 4 µm.

The limit on O/M ratio, calculated as O/(U + Pu + Am), is 1.98 to 2.01.

3. For the experimental thermal MOX data, what were the O/M ratios used for code verification?

Response:

The O/M values used in the code verification are presented below. They are the best definition of the actual fuel characterization, i.e. the fabrication values for lower burnup MOX (GRIMOX) and equilibrium values reached after irradiation of higher burnup MOX (IFA 610 & IFA 606).

[d.]

4. **For the MOX fission gas release data, please provide the nominal and range of PuO_2 particle size for the different experimental rods used for code verification?**

Response:

The mean particle diameter in the MIMAS ammonium uranyl carbonate (AUC) wet route process pellet lots used in surveillance programs was [d.] microns. The mean particle diameter in the MIMAS ammonium diuranate (ADU) wet route process pellet lot was [d.] microns.

Figure 1 shows the results of electron probe micro-analyses of the plutonium rich particle size distribution on two representative fuel batches of MOX AUC and ADU (TU2). The total plutonium content is plotted as a function of particle size. This shows that about [d.] of the plutonium in the pellet is contained within particles larger than [d.] microns for the MIMAS/ADU (TU2) fuel, and about [d.] for the MIMAS/AUC fuel. Current plans are to utilize UO_2 produced via the ADU process in the Weapons Grade MOX Program.

5. **The conductivity equation for unirradiated MOX (Eq. 4-44) defines the term, y, as Pu content in weight-percent, but it appears that this may be weight fraction. Please verify which unit is intended. If the Pu content is in weight fraction, the correction for Pu conductivity is small for 100 wt% PuO_2, which appears to be too low (see questions 6 and 8 below).**

Response:

The correct unit is weight fraction.

As indicated in Chapter 1 of the COPERNIC topical, COPERNIC is applicable to MOX fuels up to [d.] weight percent plutonium. However, the maximum plutonium content currently planned for weapons grade MOX fuels is less than 5 weight percent and will be limited to less than six weight percent.

MOX fuel is a heterogeneous mixture of UO_2 and PuO_2 with the bulk of the fuel matrix comprised of UO_2. This leads to a modest reduction in thermal conductivity for MOX fuels compared with UO_2 fuels, as demonstrated for the COPERNIC and other thermal conductivity relationships in the response to 1st-Round MOX Question 6.

9. What are the gas production values (xenon, krypton and helium) used in COPERNIC for MOX. Justify their application to weapons grade Pu. Also, how are the release fractions for helium determined in the rod pressure analysis, LOCA analyses, and other analyses where it is important?

Response:

COPERNIC uses [b., d]

The fission yield of stable Xe + Kr isotopes for thermal fission of U-235 is 24.99% and 25.29% for thermal fission of Pu-239[3].

Helium is generated in fuel matrices by alpha decay of trans-uranium nuclides, such as the Cm^{242} (n, alpha) reaction, and ternary fission, the former being the major source. Studies of helium behavior showed that the helium diffusion coefficient in UO_2 is several orders of magnitude larger than that of noble fission gases and that helium is highly soluble in UO_2 [4,5]. Helium is not released from the fuel as long as its content does not exceed the solubility limit, which depends on the helium partial pressure in the rod.

[b., d.]

Additionally, helium production in weapons grade MOX fuel is lower than that of reactor grade MOX fuel due to the lower initial Pu-240, Pu-241, and Am-241 content (see Table 1).

10. Has Framatome (or other parties) examined the interface between MOX fuel and the cladding at high burnups to determine if there are any chemical reactions (such as Zr-oxide formation or other reactions) between the fuel and cladding?

Response:

The interface between MOX fuel and the cladding has been thoroughly examined on ~20 radial ceramographic micrographs performed on high burnup (53 GWd/t) rods. A zirconia layer of up to 10-12 μm has been observed, which is comparable to that seen for uranium fuel at equivalent exposure. No other chemical reactions have been observed.

Table 1
Typical plutonium isotopics (wt %) for the most abundant isotopes

Plutonium Isotope	Weapons Grade	Reactor Grade
^{238}Pu	0.0	1.0
^{239}Pu	93.6	59.0
^{240}Pu	5.9	24.0
$^{241}Pu^{*}$	0.4	10.0
^{242}Pu	0.1	5.0
$^{241}Am^{*}$	0.0	1.0

*Amount varies with decay time.

Table 2a
Normalized Radial Power Profile for 6 Weight Percent Reactor Grade MOX

[b., d.]

Table 2b
Normalized Radial Power Profile for 6 Weight Percent Weapons Grade MOX

[b., d.]

Figure 1
Plutonium Rich Particle Size Distribution

[d.]

Figure 2
Helium Balance in MOX PWR Fuel Rods

[b., d.]

References

1. Stewart N. Bailey (NRC) to T. A. Coleman (Framatome Cogema Fuels), *Safety Evaluation of Topical Report BAW-10228P, "SCIENCE" (TAC No. MA4599)*, October 26, 1999.

2. Stewart A. Richards (NRC) to T. A. Coleman (Framatome Cogema Fuels), *Correction to Safety Evaluation of Topical Report BAW-10228P, "SCIENCE" (TAC No. MA4599)*, May 24, 2000.

3. JEF – PC, O.E.C.D./NEA Data Bank, Version 1, November, 1994.

4. W.A. Stark, *Helium release from PuO_2 microspheres*", Nuclear Metallurgy, Vol. 17, Part 2 (1970) 554.

5. R. W. Grimes, *Simulating the behaviour of inert gases in UO_2*, Fundamental Aspects of Inert Gases, Plenum Press, New York, 1991.

bc:

NRC:02:021
L. C. Bernard
B. J. Delano
S. De Perthuis
F. P. Faucher
J. D. Gale
G. E. Hanson
R. L. Hame
P. J. Henningson
J. A. Hoerner
J. S. Holm
J. A. Klingenfus
L. L. Losh
J. F. Marrot
C. F. McPhatter
G. A. Meyer
E. Morel
P. Vesco
D. A. Wesley
R. D. Williamson
File/LB

FRAMATOME COGEMA FUELS

Lynchburg, Virginia

Report BAW-10231

September, 1999

COPERNIC Fuel Rod Design Computer Code

Key Words: Pressurized Water Reactor, Fuel Rod Design, Uranium Dioxide, Mixed Oxide, Urania-Gadolinia, Zircaloy-4, M5 Advanced Alloy, Material Properties

---

ABSTRACT

This document describes the COPERNIC fuel rod design computer code and its application to fuel designed and licensed by FRAMATOME COGEMA FUELS. COPERNIC performs thermal/mechanical analyses to accurately simulate the behavior of a fuel rod during irradiation and will be used to verify that specific rod designs meet all design and safety criteria. COPERNIC will be used to calculate fuel melting, fuel rod internal gas pressure, cladding strain, cladding creep collapse code initialization, cladding peak oxide thickness, and loss-of-coolant accident (LOCA) analysis initialization parameters. COPERNIC will also provide best-estimate fuel performance predictions for other analyses as appropriate. COPERNIC is applicable to uranium dioxide, mixed oxide, and urania-gadolinia fuel with either Zircaloy-4 or M5 advanced alloy cladding. Fuel rod average burnups of up to 67 GWd/tU can be analyzed.

This page intentionally left blank.

This page intentionally left blank.

1. INTRODUCTION

This document presents the new fuel rod design tool developed by FRAMATOME to evaluate fuel rod thermal-mechanical performance: COPERNIC (Fuel Rod Design Computer Code).

The European TRANSURANUS code (Ref. 1-1 and Ref. 1-2) was used as a basis for COPERNIC. The TRANSURANUS code architecture which is based on a mathematical framework of the heat transfer and mechanical models was maintained. However, the individual physical models representing the complex phenomena which take place in the fuel, the pellet-cladding gap, the cladding and at the fuel rod/coolant interface are FRAMATOME models. The individual physical models were developed from the latest knowledge of these phenomena based on FRAMATOME's large experimental data base from domestic and international programs. The qualification of the COPERNIC code by comparison of code predictions to test results is described in this document.

COPERNIC performs the thermal/mechanical analyses necessary to accurately simulate the behavior of a fuel rod during its irradiation.

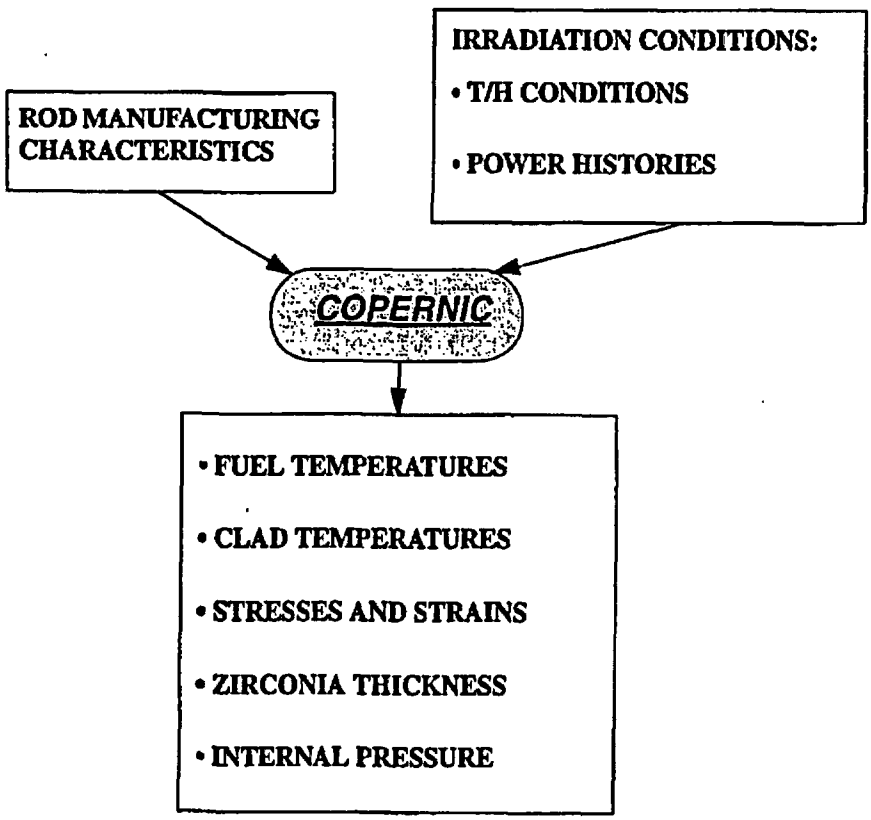

COPERNIC will be used to verify that specific fuel rod designs, for a given reactor and operating conditions, meet all design and safety criteria.

COPERNIC is applicable to the following:

Fuel:

- UO_2, MOX, UO_2-Gd_2O_3

Cladding:

- Zircaloy 4 (stress-relieved and recrystallized)
- Alloy 5 Advanced Cladding (M5)

Enrichments and contents in weight per cent:

- UO_2: up to [b.]
- MOX: up to [b.]
- UO_2-Gd_2O_3: up to 10 wt.% Gd_2O_3 (8 wt.% for United States applications only)

Initial density:

- Greater than [b.]

Maximum rod power:

- Up to [b.]

Rod average burnup:

- UO_2: 0-67000 MWd/tU
- MOX: 0-53000 MWd/tM
- UO_2-Gd_2O_3: 0-55000 MWd/tM

This report is divided into 12 chapters. Chapters 1, 2, and 3 provide an overview of the code architecture and experimental benchmark programs. In depth descriptions of the code models and benchmarks for various physical phenomena are contained in Chapters 4 to 9. The code specific material property relations are defined in Chapter 10 and Chapter 11 shows example code input and output listings. Chapter 12 concludes this Topical Report with the applications methodology for use in the United States.

REFERENCES

Ref. 1-1 K. LASSMANN, *URANUS - A Computer Program for the Thermal and Mechanical Analysis of the Fuel Rods in a Nuclear Reactor*, Nuclear Engineering and Design 45 (1978), pp 325-343.

Ref. 1-2 K. LASSMANN, H. BLANK, *Modeling of Fuel Rod Behaviour and recent Advances of the TRANSURANUS Code*, Nuclear Engineering and Design 106 (1988), pp 291-313.

This page intentionally left blank.

2. CODE ARCHITECTURE

2.1. Fuel Rod Modeling Hypotheses and Discretization

2.1.1. General Concept

The COPERNIC code architectural structure reflects the following general concepts. The fuel rod is subdivided into discrete axial regions or slices. These slices are further subdivided into discrete radial regions or concentric rings. This slice and ring composite forms the numerical framework (quasi-two dimensional) for the mathematical analyses. The axial slices are individually analyzed for each time step. When all of the slices have been analyzed, they are coupled and quantities such as internal pressure and axial friction forces are determined. This general mathematical calculation sequence, which is performed at each time step, produces fuel rod predictions that accurately simulate fuel rod behavior.

2.1.2. Irradiation History - Time Discretization

The time-dependent quantities (linear power, fast flux, T/H data, etc.) are described by the user for each «macro-time step». Each macro-time step is divided by the code into additional micro-time steps which are used for computation (Figure 2-1). These «micro-time steps» correspond to the largest permissible time step. Micro-time step size is based upon the variation of a certain number of quantities that relate to heat transfer, mechanical behavior, and fission gas release (increase in temperature, volume changes, increase in Xe concentration, etc.). The quantity is calculated by linear interpolation from the data of two successive macro-time steps.

2.1.3. Spatial Discretization

2.1.3.1. Axial Discretization

The fuel stack is divided into axial slices (Figure 2-2). The upper plenum is treated as an additional axial slice which can vary with time. A lower plenum volume can also be modeled but does not vary during irradiation. There is no variation of calculated parameters axially along a given axial slice.

2.1.3.2. Radial Discretization

Each axial slice is subdivided into concentric rings (called macro-zones), which are further divided into finer rings (called micro-zones) (Figure 2-3). In each macro-zone (fuel or clad), YOUNG's modulus and POISSON's ratios are assumed constant.

2.1.4. Thermal Calculation Approach

The thermal problem is solved for the axisymmetric cylindrical geometry (axial and azimuthal effects are neglected). Axial conduction (in the cladding and fuel) is therefore neglected. The coolant conditions are calculated separately with the temperature used as an external boundary condition. Steady state and transient predictions are available.

2.1.5. Mechanical Calculation Approach

The mechanical problem is formulated with an axisymmetrical cylindrical geometry using a generalized plane strain hypothesis (one-dimensional radial solution and uniform axial strain). Fuel-clad axial coupling effects are taken into account after gap closure. The elastic constants are isotropic and constant within each cylindrical ring (macro-zone).

2.2. Thermal Analysis

2.2.1. Basic Equation

Given the thermal calculational approach, the heat conduction equation reduces to:

$$\frac{\partial}{\partial t}(\rho c_p T) = \frac{1}{r}\cdot\frac{\partial}{\partial r}\left(\lambda r\cdot\frac{\partial T}{\partial r}\right)+\bar{q} \qquad \text{Eq. 2-1}$$

where:

- $\bar{q}$: volumetric heat generation rate,
- c_p : specific heat,
- r : radius,
- λ : thermal conductivity, and
- ρ : density.

2.2.2. Boundary Conditions

The boundary conditions used are:

- zero heat flux at the center of a solid pellet or at the inner radius of an annular pellet, and
- imposed outer surface temperature.

2.2.3. Method of Solution

The fuel temperatures are calculated at the radial region nodes:

i : inner surface of ring j, and

o : outer surface of ring j.

The quantity X_j, representing the physical properties within ring j, is calculated as follows:

[b.] Eq. 2-2

The coefficients β_i in the above equation are calculated [e.]:

[b.] Eq. 2-3

[b.] Eq. 2-4

The coefficients represent a trade-off between the finite difference and the finite element methods for temperature with optimal results obtained by letting:

[b.] Eq. 2-5

[b.] Eq. 2-6

[b.] Eq. 2-7

Fuel + cladding equation:

Assuming that [e.], the solution of equation 2-1 is:

$$T(r,t) = -\frac{\bar{q}_f \cdot r^2}{4\lambda} + \ln(r) \cdot c_1(t) + c_2(t) \qquad \text{Eq. 2-8}$$

where:

$$\bar{q}_f = \bar{q} - c_p \rho \cdot \frac{\partial T}{\partial t} \qquad \text{Eq. 2-9}$$

The constants $c_1(t)$ and $c_2(t)$ can be calculated from:

[b.] Eq. 2-10

[b.] Eq. 2-11

where: T_i^j = inner temperature of ring j, and

T_o^j = outer temperature of ring j.

The solution of T(r, t) using equation 2-8 then becomes:

[b.] Eq. 2-12

The heat transfer between rings j and j+1 can then be written as:

[b.] Eq. 2-13

[b.] Eq. 2-14

The heat transfer coefficient [e.]:

- [e.]
- [e.]

For other rings:

$$h_0^j = \infty \qquad \text{Eq. 2-15}$$

Since the heat flux and temperature gradient are related by Fourier's Law:

$$\vec{q}^j(r, t_n) = -\lambda^j \frac{\partial}{\partial r} T\left(r^j, t_n\right) \qquad \text{Eq. 2-16}$$

The substitution of the expression for the temperature derivative (equation 2-12) into the previous equation (2-16) yields an expression for the heat flux:

[b.] Eq. 2-17

If θ is the time discretization factor, a [e.] method applied to equation 2-13 gives:

[b.] Eq. 2-18

Equations 2-17 and 2-14 in equation 2-18 produce an equation of the form:

[b.] Eq. 2-19

The unknowns in equation 2-19 are [b.], where:

n is time t, and

n+1 is time t+Δt.

2.3. Mechanical Analysis

2.3.1. Basic Equations

The numerical solution of the equations that define the mechanical characteristics of the fuel rod requires dividing the fuel and cladding into rings (macro-zones) in which the material is considered homogeneous (the elastic constants, for example, are assumed constant) across each ring. Further, the large radial variation of temperature within the fuel, and therefore stress level, requires an additional subdivision of the calculational rings into a number of finer rings (micro-zones) to ensure numerical convergence.

2.3.1.1. Constitutive Equations

At each point (r, Θ, z), the total strain is the sum of the individual contributions, i.e:

$$[\varepsilon] = [b.] \qquad \text{Eq. 2-20}$$

The calculation of the various strains is described in the following paragraphs:

- Creep: Irradiation creep page 7-1,
- Densification-swelling: Densification-Solid Swelling page 6-5, and
- Relocation: Fractured Fuel Relocation page 6-1.

The set of non-elastic contributions can be [e.]:

$$[b.] \qquad \text{Eq. 2-21}$$

2.3.1.2. Compatibility Equations

Since the plane strain hypothesis requires ε_z to be constant and independent of radius, the compatibility equations are:

$$[\varepsilon] = \begin{bmatrix} \varepsilon_r \\ \varepsilon_\Theta \\ \varepsilon_z \end{bmatrix} = \begin{bmatrix} \frac{du}{dR} \\ \frac{u}{R} \\ C_3 \end{bmatrix} \qquad \text{Eq. 2-22}$$

where u is the displacement at radius R.

2.3.1.3. Equilibrium Equations

Axial symmetry dictates that the radial and azimuthal stresses are related by:

$$\frac{d\sigma_r}{dr} + \frac{\sigma_r - \sigma_\Theta}{R} = 0 \qquad \text{Eq. 2-23}$$

2.3.2. Boundary Conditions

The stresses calculated on the inner and outer faces of the fuel, cladding, or in case of contact, the fuel and cladding combination, must equal the internal and external pressures on these faces:

$$\left(\sigma_r^{R = R_{int}}\right)_{j=1} = -P_{int} \qquad \text{Eq. 2-24}$$

$$\left(\sigma_r^{R = R_{ext}}\right)_{j=n} = -P_{ext} \qquad \text{Eq. 2-25}$$

When passing from ring j to ring j+1, continuity conditions imposed on radial displacement and

stress require that:

$$\left(u^{R=R_o}\right)_j = \left(u^{R=R_i}\right)_{j+1} \quad \text{Eq. 2-26}$$

$$\left(\sigma_r^{R=R_o}\right)_j = \left(\sigma_r^{R=R_i}\right)_{j+1} \quad \text{Eq. 2-27}$$

The constant C_3^j is determined from the axial boundary condition imposed on the fuel, cladding, or in case of contact, the fuel and cladding combination.

$$\sum_{j=1}^{n} \int_{R_i}^{R_o} \sigma_z(R) 2\pi R dR = -F_z \quad \text{Eq. 2-28}$$

where F_Z is the axial force acting on an axial slice.

2.3.3. Method of Solution

A differential equation in [e.]:

[b.] Eq. 2-29

where ν is Poisson's ratio. The integrals (I_1, I_2, and I_3) and the constants (C_1, and C_2) are defined below.

The expressions for the three components [e.]

The resulting strain expressions are:

[b.] Eq. 2-30

[b.] Eq. 2-31

[b.] Eq. 2-32

and the stress expressions are:

[b.] Eq. 2-33

[b.] Eq. 2-34

[b.] Eq. 2-35

where E^j is Young's modulus, C_1, C_2, C_3 are constants of integration that are determined from the boundary conditions (equations 2-24, 2-25, 2-26, 2-27 and 2-28).

I_i^j are definite integrals that contain [e.]:

[b.] Eq. 2-36

[b.] Eq. 2-37

[b.] Eq. 2-38

[b.] Eq. 2-39

Since the ε^{ex} strains cannot be solved analytically, the integrals I_1 through I_4 must be evaluated numerically.

A semi-analytical solution that divides each «macro-zone» into small zones is used with the

following approximations:

[b.] Eq. 2-40

[e.]

[b.] Eq. 2-41

for plastic and creep strains.

2.4. Numerical Method and Flow Chart

The calculation logic is set by the modeling approaches. For each «micro-time step», each axial slice is successively calculated. The thermal analysis (page 2-2) and mechanical analysis (page 2-5), described in the previous paragraphs are combined with the fission gas release calculation for the fuel (chapter 5) and the waterside corrosion calculation for the cladding (chapter 8). The fuel rod internal gas pressure is then evaluated by considering [e.]. Given the close interactions between all the physical phenomena, it is necessary to perform iterations:

- [e.]
- [e.]

A general code flow chart is given in Figure 2-4. The various phenomena allowed for in an axial slice are shown in Figure 2-3.

This page intentionally left blank.

FIGURES

FIGURE 2-1 FUEL ROD POWER HISTORY

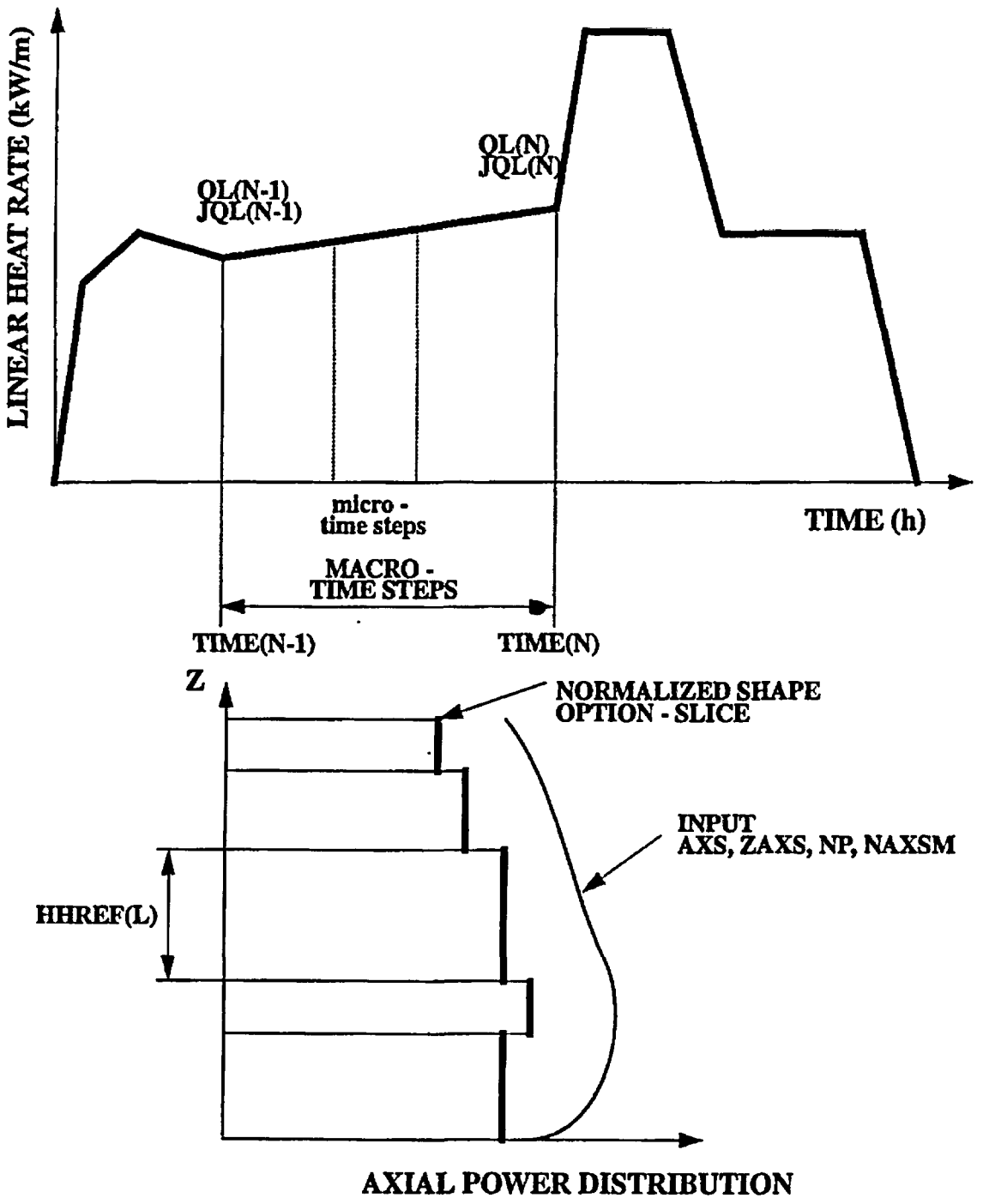

Note: The COPERNIC variables shown in this figure (QL, JQL, HHREF, etc.) are defined in chapter 11"User's guide"

FIGURE 2-2 FUEL ROD MODEL

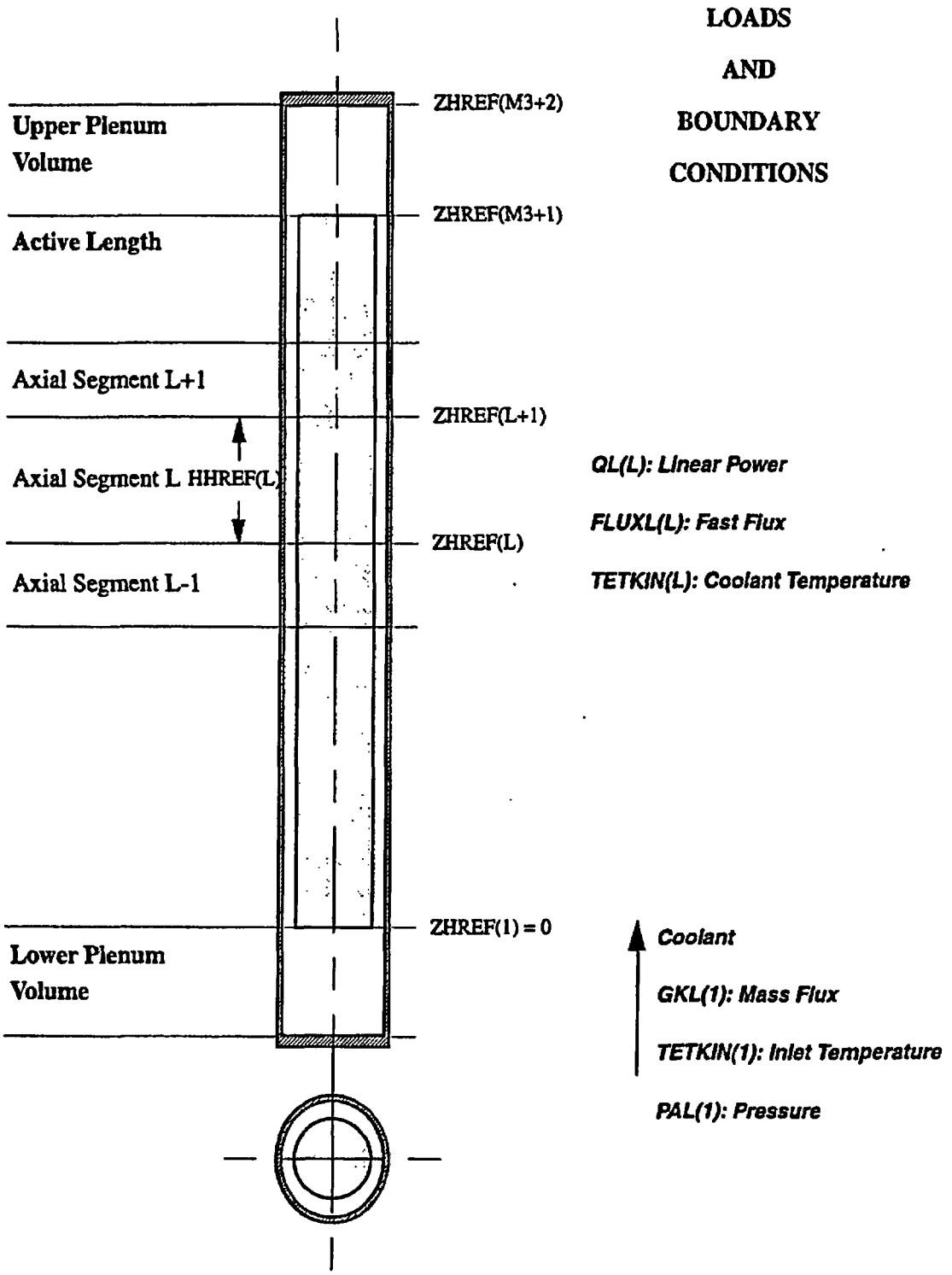

Note: The COPERNIC variables shown in this figure (QL, FLUXL, TETKIN, etc.) are defined in chapter 11"User's guide"

FIGURE 2-3 RADIAL NODING

[b.]

FIGURE 2-4 COPERNIC PROGRAM FLOW

[b.]

This page intentionally left blank.

3. EXPERIMENTAL DATABASE

The experimental database used to develop and validate the models includes results from a variety of Research and Development Programs, as follows (Table 3-1):

3.1. French Industry Programs

Instrumented fuel rods were irradiated or re-irradiated in pile and focused on one or more individual fuel rod phenomena. These experiments, conducted in conjunction with the CEA and most often with EDF, enable the direct validation of some models (thermal for example) or supply data to obtain greater insight into the mechanisms involved with the physical phenomena (fission gas release for example).

The programs used to validate COPERNIC were the following:

- [b., d.]
- [b., d.]
- [b., d.]
- [b., d.]
- [b., d.]
- [b., d.]
- [b., d.]
- [b., d.]

3.2. International Programs

These programs investigated fuel rod behavior in general or the variation of selected parameters under special irradiation conditions and include:

- the international STUDSVIK ramp test programs (OVER RAMP, TRANSRAMP IV): behavior of fuel rods during power ramps

- HBEP (High Burnup Effects Program): high burnup fission gas release [b., d.]

- TRIBULATION: influence of power transients on extended burnup fuel rod behavior

- NFIR: high-burnup fuel properties

- HBC (High Burnup Chemistry): high-burnup fuel chemistry and thermal properties

- PRIMO: PWR behavior of MOX fuel rods up to [b., d.]

- GAIN: PWR behavior of gadolinia fuel rods up to [b., d.]

- HALDEN reactor instrumented rod irradiation programs: IFA-431, IFA-432, IFA-513, IFA-527, [b., d.]

3.3. Power Ramp Programs

Power ramp tests on rodlets extracted from full-length fuel rod (initialy segmented or refabricated) irradiated in power reactors were used to qualify the code under transient conditions. These ramp tests were performed either in the Studsvik R2 reactor (OVER RAMP, TRANSRAMP IV, STUDSVIK ramps), in the CEA OSIRIS (J12_2 and other ramps) or SILOE experimental reactors (REGATE and HATAC ramps).

3.4. Commercial Reactor Irradiation Campaigns

These campaigns were performed in cooperation with EDF and CEA. Two types of programs have been implemented:

- on-site examinations which have yielded dimensional (fuel rod growth) and corrosion data from several thousand rods,

- post irradiation examinations (PIE) in the CEA hot cells.

These campaigns included the following fuel types:

- FRAGEMA UO_2 fuel was irradiated in the TIHANGE (15x15), BROKDORF (16x16), BUGEY, FESSENHEIM, GRAVELINES and CRUAS (17x17) reactors. Some of these rods were irradiated under load follow conditions (GRAVELINES, CRUAS). A maximum average rod burnup of [b., d.] was reached by rods that were irradiated for [e.] in the GRAVELINES reactors.

- FRAGEMA UO_2 fuel with Alloy 5 advanced cladding was irradiated in the CHINON 3, CRUAS 2, GRAVELINES 5 reactors. Rods from these campaigns were pulled after [e.] of irradiation. The maximum rod average burnup attained was [b., d.].

- FRAGEMA MOX fuel was irradiated in the St-LAURENT B1, St-LAURENT B2, GRAVELINES 4 and DAMPIERRE 2 reactors. Rods from these campaigns were pulled after [e.] and examined in a hot cell. The maximum rod average burnup attained was [b., d.].

- FRAGEMA UO_2-Gd_2O_3 fuel was irradiated in the GRAVELINES reactors. Rods from these campaigns were pulled after [e.] of irradiation. The maximum rod average burnup attained was [b., d.].

3.5. BR3 and CAP Test Reactor Irradiation Programs

Rods of various designs were investigated with the CEA in these programs. Approximately one thousand rods were irradiated in the BR3 test reactor (cores 2B to 4D2), and about 150 were subjected to post-irradiation-examinations. The maximum rod average burnup attained by a UO_2 rod irradiated [e.] was [b., d.].

Approximately one thousand rods were irradiated in the CAP (Chaudière Avancée Prototype) test reactor under load follow conditions. About thirty rods from this campaign were subjected to post-irradiation-examinations.

3.6. Older Programs

Data from programs that were conducted in the 1970's on UO_2 and MOX fuels were also used to validate the code. This data came from:

- American sponsored programs: ZORITA, BR3.

3.7. Literature Survey

In some cases, the information or experimental data supplied in the open literature were used to confirm COPERNIC modeling hypotheses and predictions.

3.8. Fuel Performance Database

Generally speaking, rods pulled and transferred to hot cells are non-destructively examined for the following:

- visual appearance
- rod length
- neutron radiography
- γ-spectrometry
- diameter
- eddy current
- oxide layer thickness
- gas puncture and analysis.

In some cases, destructive examinations are performed:
- metallography/ceramography
- density measurement
- microprobe analysis
- burnup measurement
- mechanical tests.

Irradiated rod data are placed in the FRAMATOME database as it becomes available. The database contains rods with a variety of designs and production runs that were irradiated under varying conditions.

Tables 3-2, 3-3 and 3-4 list the UO_2, MOX and UO_2-Gd_2O_3 fuel rods (examined in hot cells) contained in FRAMATOME's database.

TABLES

TABLE 3-1 EXPERIMENTS AND PROGRAMS

THERMAL	FGR	MECHANICAL	COMMENTS
[d.]			

TABLE 3-2 EXPERIMENTAL DATABASE - LIST OF UO_2 FUEL RODS

Design	Reactor	Program	Number of Cycles	Number of Fuel Rods	Fuel Type	Clad Type	Fuel Rod Average Burnup GWd/tU	Comments

[d.]

Design	Reactor	Program	Number of Cycles	Number of Fuel Rods	Fuel Type	Clad Type	Fuel Rod Average Burnup GWd/tU	Comments
[d.]								

Design	Reactor	Program	Number of Cycles	Number of Fuel Rods	Fuel Type	Clad Type	Fuel Rod Average Burnup, GWd/tU	Comments

[d.]

Design	Reactor	Program	Number of Cycles	Number of Fuel Rods	Fuel Type	Clad Type	Fuel Rod Average Burnup GWd/tU	Comments
[d.]								

[d.]

[d.]

[d.]

[d.]

[d.]

[d.]

[d.]

[d.]

[d.]

[d.]

[d.]

[d.]

[d.]

[d.]

[d.]

TABLE 3-3 EXPERIMENTAL DATABASE - LIST OF MOX FUEL RODS

Design	Reactor	Program	Number of Cycles	Number of Fuel Rods	Fuel Type	Clad Type	Fuel Rod Average Burnup GWd/tM
[d.]							

Design	Reactor	Program	Number of Cycles	Number of Fuel Rods	Fuel Type	Clad Type	Fuel Rod Average Burnup GWd/tM
[d.]							

TABLE 3-4 EXPERIMENTAL DATABASE - LIST OF UO_2-Gd_2O_3 FUEL RODS

Design	Reactor	Program	Number of Cycles	Number of Fuel Rods	Clad Type	Fuel Rod Average Burnup GWd/tM	Comments
[d.]							

4. THERMAL MODEL

Several thermal related phenomena must be properly addressed to accurately predict fuel temperatures. These phenomena include the heat transferred from the outside surface of the fuel rod to the coolant, the fuel-cladding gap conductance, the fuel thermal conductivity, the heat transfer gap closure, and the fuel radial power distribution. The COPERNIC models for these phenomena are presented in the following sections. Each section will contain, as appropriate, a description of the physical phenomena that must be considered, the model development, the experimental database used in calibrating the model, the experimental validation database, adaptations for mixed fuel types, and the range of validity. The global experimental validation, that considers all of the models, is presented in the last section.

4.1. Coolant-Fuel Rod Outside Surface Heat Transfer

4.1.1. Phenomenon

A single phase forced convection heat transfer coefficient (h) is used to predict the fuel rod outside surface temperature (T_{P1}), as function of fluid temperature (T_L) and the surface heat flux (Φ).

$$T_{P1} = T_L + \frac{\Phi}{h} \qquad \text{Eq. 4-1}$$

When boiling occurs, the fuel rod outside surface temperature is limited to a value T_{P2} that exceeds the saturation temperature (T_{SAT}) by ΔT_{SAT}:

$$T_{P2} = T_{SAT} + \Delta T_{SAT} \qquad \text{Eq. 4-2}$$

The fuel rod outside surface temperature is then obtained from the minimum of equations 4-1 and 4-2:

$$T_P = \min(T_{P1}, T_{P2}) \qquad \text{Eq. 4-3}$$

4.1.2. Model

The single phase forced convection heat transfer coefficient is predicted with the [e.] relationship:

[e.] Eq. 4-4

where

- h : exchange coefficient in $W/(cm^2.K)$,
- C = [e.],
- D_h : hydraulic diameter (cm),

G : mass flux in g/(cm^2.s),

h_0 = [e.],

K_h = [e.], and

ω = [e.].

During two phase forced convection, the difference (ΔT_{SAT}) between the fuel rod outside surface temperature and the saturation temperature is predicted with the Jens Lottes relationship:

$$\Delta T_{SAT} = 7.91 \cdot e^{-P/62} \cdot \Phi^{0.25} \qquad \text{Eq. 4-5}$$

where

P : pressure (bar), and

Φ : surface heat flux (W/cm^2).

4.2. Pellet-Cladding Heat Transfer

4.2.1. Notation

RHR (Arithmetic) Roughness:

$$RHR = \frac{1}{L} \cdot \int_0^L |g(x)| dx \qquad \text{Eq. 4-6}$$

RMS (Root Mean Square) Roughness:

$$RMS = \left[\frac{1}{L} \cdot \int_0^L g^2(x) dx \right]^{1/2} \qquad \text{Eq. 4-7}$$

where

g(x) : deviation from the average roughness, and

L : probed length.

ISM Interfacial Surface Morphology: the ISM characterizes the condition of the fuel and cladding surfaces and are given below in units of RMS roughness.

ISM I: average fuel roughness : 14.4 µm,
average clad roughness : 4.5 µm,
combined roughness : **15.08** µm.

ISM II: average fuel roughness : 1.6 µm,
average clad roughness: 0.4 µm,
combined roughness : 1.65 µm.

ISM III: average fuel roughness : 0.25 µm,
average clad roughness: 0.17 µm,
combined roughness : 0.30 µm.

Definitions

a_1, a_2	fuel and clad accommodation coefficients
A	visual fuel (or clad) surface area
Ag	projected gap surface area
g_1, g_2	fuel and cladding temperature jump lengths
h_c	contact conductance
h_{gas}	gaseous conductance
h_{gap}	total gap conductance
h_r	thermal radiation conductance
k	fitting coefficient (function of contact pressure and hardness)
m	mean asperity slope
H_M	Meyer hardness
M	molecular weight
M_i	molecular weight of the i^{th} gas species
n	number of different gas species
P	total gas pressure
P_i	partial pressure of the i^{th} gas species
P_{con}	contact pressure
P_{pl}	contact pressure (transition elastic-plastic)
R	ideal gas constant
R_i	roughness factor
T	gas temperature
T_f, T_c	fuel and clad temperatures

x_i mole fraction for the i^{th} gas species

X heat transfer gap multiplier

Y gap between surface mean planes

δ gap between two smooth flat surfaces

$\varepsilon_f, \varepsilon_c$ fuel and clad emissivity

Φ_{ij} gas mixture coefficient

γ ratio of specific heats

Γ_i thermal conductivity factor for the i^{th} gas species

λ gas thermal conductivity

λ_i thermal conductivity for the i^{th} gas species

λ_f, λ_c fuel and cladding thermal conductivity

λ_{mix} gas mixture thermal conductivity

λ_{avg} [e.] thermal conductivity

[e.] Eq. 4-8

σ effective surface roughness

$$\sigma = \sqrt{\sigma_{fuel}^2 + \sigma_{clad}^2} \quad \text{Eq. 4-9}$$

σ_{rad} Stefan Boltzmann constant

Ω_i sum of fuel and cladding dimensionless temperature jump lengths for the i^{th} gas species

4.2.2. Phenomena

Heat transferred across the pellet-cladding gap includes the following thermal phenomena:

- thermal radiation,
- gaseous conductance,
- contact conductance during pellet-cladding contact.

The total gap conductance is the sum of these three contributions:

$$h_{gap} = h_r + h_{gas} + h_c \quad \text{Eq. 4-10}$$

4.2.3. Pellet-Cladding Gap Conductance Model

4.2.3.1. Thermal Radiation

The thermal radiation heat transfer coefficient is given by the classical equations:

$$h_r = K \cdot \frac{T_f^4 - T_c^4}{T_f - T_c} \qquad \text{Eq. 4-11}$$

$$K = \sigma_{rad} \cdot \frac{\varepsilon_f \cdot \varepsilon_c}{\varepsilon_f + \varepsilon_c - (\varepsilon_f \cdot \varepsilon_c)} \qquad \text{Eq. 4-12}$$

where

σ_{rad} : Stefan-Boltzmann constant,

ε_f, ε_c : fuel and clad emissivities, and

T_f, T_c : fuel and cladding surface temperatures.

4.2.3.2. Gaseous Conductance

The COPERNIC gaseous conductance model is taken from the work of WESLEY and YOVANOVICH (Ref. 4-1). The model accounts for the fact that the pellet-cladding gap size can be of the same order of magnitude as the molecular mean free path (KNUDSEN range). In this case, the temperature discontinuity effects at the pellet and cladding surfaces result in a fictional gap widening through the extrapolation (temperature jump) lengths. The exchange coefficient can then be written:

$$h_{gas} = \frac{\lambda}{\delta + g_1 + g_2} \qquad \text{Eq. 4-13}$$

The temperature jump lengths are evaluated by applying the kinetic theory of gases. The relationship obtained from the KNUDSEN theory gives the following expression:

$$g_1 + g_2 = \frac{\lambda}{P} \cdot \left(\frac{a_1 + a_2 - a_1 a_2}{a_1 a_2} \right) \cdot \left(\frac{\gamma - 1}{\gamma + 1} \right) \cdot \left(8\pi \frac{MT}{R} \right)^{1/2} \qquad \text{Eq. 4-14}$$

Although these equations are common for pure gases, it is difficult to extend them to gaseous mixtures. The approach selected for gaseous mixtures relies on techniques developed to estimate

the thermal conductivity of gaseous mixtures:

$$\lambda_{mix} = \sum_{i=1}^{n} \frac{x_i \cdot \lambda_i}{\Gamma_i} \qquad \text{Eq. 4-15}$$

where

$$\Gamma_i = \sum_{j \neq i}^{n} x_j \cdot \Phi_{ij} \qquad \text{Eq. 4-16}$$

Φ_{ij} is a function of the thermal conductivities and molecular weights.

[e.] Eq. 4-17

where

[e.] Eq. 4-18

and

[e.] Eq. 4-19

The thermal conductivity of a gas can be related to the sum of the energies of the molecules that pass through a fictional plane. By extending this viewpoint to gaseous mixtures, equation 4-15 effectively partitions the energy passing through the plane into components of $x_i \lambda_i / \Gamma_i$. These components are applied directly to the pure gas temperature jump equations to obtain the components of heat conductance. The sum of these conductances in parallel represents the total conductance of a gaseous mixture. This approach was used by HAGRMAN (Ref. 4-2) to obtain the heat exchange coefficient of a gaseous mixture:

$$h_{gas} = \sum_{i=1}^{n} \frac{\left(\frac{x_i \cdot \lambda_i}{\Gamma_i}\right)}{\left[\frac{\lambda_i}{P \cdot \Gamma_i}\left(\frac{a_1 + a_2 - a_1 a_2}{a_1 a_2}\right)_i \left(\frac{\gamma - 1}{\gamma + 1}\right)_i \left(8\pi \frac{M_i T}{R}\right)^{1/2} + \delta\right]} \qquad \text{Eq. 4-20}$$

The above equation is valid for smooth surfaces.

All surfaces, however, have some roughness. An approach taken to account for roughness consists

of modeling the two rough surfaces with a single rougher surface and a smooth flat surface.

The roughness of the combined rougher surface is:

$$\sigma = \sqrt{\sigma_1^2 + \sigma_2^2} \qquad \text{Eq. 4-21}$$

where

σ_1, σ_2: roughnesses of each surface.

The heat transfer between the surfaces is assumed to be confined to parallel flux tubes that span the surfaces. This one-dimensional approximation is justified because the asperities of the rough surfaces typically have included angles that are greater than 160 degrees.

It can be shown for two surfaces that are separated by a gap of size Y, the area of the flux tubes with lengths between t and t + dt is:

$$da = \frac{A}{\sqrt{2\pi}} \cdot \exp\left[-\frac{\left(\frac{Y}{\sigma} - \frac{t}{\sigma}\right)^2}{2}\right] \cdot d\left(\frac{t}{\sigma}\right) \qquad \text{Eq. 4-22}$$

This expression is valid for surfaces in contact as well as those not in contact.

The overall heat transfer coefficient between the surfaces is obtained by summing the individual contributions from all flux tubes. This discrete summation can be replaced by an integral:

$$h_{gas} = \frac{1}{A} \cdot \int_0^{A_g} \frac{\lambda}{t + g_1 + g_2} da \qquad \text{Eq. 4-23}$$

The projected gap surface A_g is equal to the visible surface A when the surfaces are not in contact. When the surfaces are in contact, A_g is less than A.

The correlation for gaseous conductance is obtained by incorporating equations 4-20 and 4-22 into equation 4-23, non-dimensionalizing, and applying the proper limits.

$$h_{gas} = \frac{1}{\sigma \cdot \sqrt{2\pi}} \cdot \sum_{i=1}^{n} \frac{x_i \cdot \lambda_i}{\Gamma_i} \cdot \int_0^{\infty} \frac{\exp\left[-\left(\frac{Y}{\sigma} - \frac{t}{\sigma}\right)^2 / 2\right]}{\frac{t}{\sigma} + \Omega_i} d\left(\frac{t}{\sigma}\right) \qquad \text{Eq. 4-24}$$

where

$$\Omega_i = \frac{\lambda_i}{\sigma P \Gamma_i} \left(\frac{a_1 + a_2 - a_1 a_2}{a_1 a_2}\right)_i \left(\frac{\gamma - 1}{\gamma + 1}\right)_i \left(8\pi \frac{M_i T}{R}\right)^{1/2} \qquad \text{Eq. 4-25}$$

An exact solution of the above integral is not trivial. Furthermore, the numerical evaluation of this integral in a fuel rod analysis code would be too time consuming. Therefore, the roughness effects

were isolated from the above equation by rewriting the equation as:

$$h_{gas} = \sum_{i=1}^{n} \left(\frac{x_i \cdot \lambda_i}{\sigma \Gamma_i} \right) \cdot \left[\frac{R_i}{\frac{Y}{\sigma} + \Omega_i} \right] \qquad \text{Eq. 4-26}$$

where

$$R_i = \frac{\frac{Y}{\sigma} + \Omega_i}{\sqrt{2\pi}} \cdot \int_0^{\infty} \frac{\exp\left[-\left(\frac{Y}{\sigma} - \frac{t}{\sigma} \right)^2 / 2 \right]}{\frac{t}{\sigma} + \Omega_i} d\left(\frac{t}{\sigma} \right) \qquad \text{Eq. 4-27}$$

R_i is the roughness factor which depends only on the Y/σ and Ω_i dimensionless variables. Since R_i is a function of dimensionless variables, the R_i values can be calculated in advance and stored in the code. The roughness factor R_i is shown in Figure 4-1 plotted as a function of the dimensionless gap (Y/σ) and the dimensionless temperature-jump lengths (Ω_i).

Note that roughness effects disappear rapidly when the dimensionless gap increases and may be ignored when the dimensionless gap exceeds ten ($Y/\sigma > 10$).

The thermal conductivities of the various gases used in the gaseous conductance expression are:

$$\lambda(T) = a_\lambda \cdot T^{b_\lambda} \qquad \text{Eq. 4-28}$$

$\lambda(T)$ is expressed in W/(m.K) and T in K.

The values of a_λ and b_λ for the various gases are:

- Helium a_λ= [b., d., e.] b_λ = [b., d., e.]
- Argon a_λ= [b., d., e.] b_λ =[b., d., e.]
- Krypton a_λ= [b., d., e.] b_λ = [b., d., e.]
- Xenon a_λ= [b., d., e.] b_λ = [b., d., e.]
- Nitrogen a_λ= [b., d., e.] b_λ = [b., d., e.]

4.2.3.3. Contact Conductance

The COPERNIC contact conductance model is based on the work of MIKIC (Ref. 4-3) and TODREAS (Ref. 4-4). The model contains two expressions that were derived from GARNIER's data (Ref. 4-5):

Eq. 4-29

Eq. 4-30

[e.] Eq. 4-31

Eq. 4-32

Eq. 4-33

Eq. 4-34

4.2.3.4. COPERNIC Model Implementation

The pellet-clad gap conductance model described above was input into COPERNIC with the following adaptations.

The radial gap between the pellet and the clad (Y), defined as the average of the local distances between the two surfaces, is calculated by:

[e.] Eq. 4-35

where

X : gap multiplier (see: Heat transfer gap closure page 4-17),

R_{ic} : clad inner radius (including various deformations),

R_{of} : pellet outer radius (including various deformations with the relocation of the fuel fragments),

σ : combined roughness of the fuel and cladding,

k : coefficient that is a function of [e.]:

[e.] Eq. 4-36

and

[e.] Eq. 4-37.

During irradiation, the fuel fractures due to thermal stresses. This fracturing and relocation of the fuel fragments closes the fuel-clad gap. The average gap reduction is given by the relocation model (Fractured Fuel Relocation chapter, page 6-1).

4.2.4. Calibration Database

The database used to validate the gap conductance model is that of GARNIER and BEGEJ (Ref. 4-5 and Ref. 4-6). All of this data was obtained from bench top experiments.

Two test techniques were employed:

- the modified laser flash technique or MPD (Modified Pulsed Design) for slight contact pressures (about 1000 Pa),
- the heat flow method or MLD (Modified Longitudinal Design) for high contact pressures (up to 14.5 MPa).

The test samples consisted of uranium dioxide (UO_2) and Zircaloy-4.

Three different surface morphologies referenced under the abbreviations ISM I, II and III (Interfacial Surface Morphology) were tested:

- a «very rough» state with the fuel and cladding roughnesses that were 14.4 and 4.5 µm, respectively (ISM I),
- a «medium» state corresponding to surfaces typical of fuel rods with fuel and cladding roughnesses that were 1.6 and 0.4 µm, respectively (ISM II),
- a «smooth» state with roughnesses of 0.25 and 0.17 µm, respectively (ISM III).

A variety of fuel and cladding gap sizes were tested (from 2.7 to 33.0 µm) with and without contact.

Two types of gaseous environments were used during the tests: pure gases and gas mixtures. The gas mixtures consisted of either helium and argon (with relative percentages of 51.8 and 48.2), or helium and xenon (with compositions (89:11), (51:49), (89.8:10.2) and (89.4:10.6)).

4.2.5. Experimental Validation and Uncertainties

4.2.5.1. Gaseous Conductance

The gaseous conductance predictions were successively validated with measurements both at atmospheric pressure and at higher pressures.

Atmospheric Pressure

All of the data that were obtained with the MPD technique were used for the validation (Ref. 4-5). This included [b., d., e.] data points that cover a wide experimental database:

- materials : UO_2-Zr4
- roughnesses: fuel : from 0.25 to 14.4 µm
  clad : from 0.17 to 4.5 µm
- temperature of gas : from 293 to 873 K
- nature of gases : He, Ar, He-Ar, He-Xe
- gas pressure : 0.103 MPa
- gap size : from [b., d., e.]

A comparison between the predicted and measured conductances is presented in Figure 4-2. The dotted lines represent the +/-12.5% uncertainty for experimental data. This value, however, does not contain the uncertainty for the gap size which ranges from 7.3 to 62.0%.

The measured to predicted (M/P) mean for these [b., d., e.].

Table 4-1 groups all the measured and predicted values.

Most points lie within the range ± 12.5% and the [b., d., e.]:

- [b., d., e.], nearly all the points correspond to a gap size of 8.6 µm, irrespective of gas composition [b., d., e.],

- [b., d., e.], most of the points correspond to [b., d., e.].

The measured and predicted conductances are shown in Figures 4-3 to 4-8 for 6 different gaseous mixtures.

The mean and standard deviations for these mixtures are listed below:

Gaseous Mixture	$(M/P)_{mean}$	$\sigma(M/P)$
Helium	[b., d., e.]	[b., d., e.]
Argon	[b., d., e.]	[b., d., e.]
He:Xe (89:11)	[b., d., e.]	[b., d., e.]
He:Xe (89.8:10.2)	[b., d., e.]	[b., d., e.]

He:Xe (51:49)	[b., d., e.]	[b., d., e.]
He:Ar (51.8:48.2)	[b., d., e.]	[b., d., e.]

Based on the measured to predicted (M/P) mean values, these predictions are satisfactory for the various helium-based gas mixtures and are slightly less accurate for Argon.

High Gas Pressures

The raw data were obtained from GARNIER and BEGEJ (Ref. 4-6).

A gap conductance bench top experiment was conducted with UO_2 and Zircaloy-4 at various gas pressures, gaseous mixture compositions (He(100); Ar(100); He:Ar(51.79:48.21) and He:Xe(89.4:10.6)) and gap sizes (5.9 µm for slight contact and 21.3 µm with open gap). A single ISM II surface condition was used.

The uncertainty in the measurements was estimated to be more than 12%.

Table 4-2 groups all the measured and predicted values.

Slight Contact (gap size of 5.9 µm)

The Figures 4-9 and 4-10 show the measured and predicted heat transfer coefficients for all of the gaseous compositions at temperatures of [b., d., e.]. The M/P mean of [b., d., e.], respectively.

The COPERNIC model produces better predictions [b., d., e.], respectively.

Open Gap (gap size of 21.3 µm and pure helium)

Figures 4-11 and 4-12 show the measured and predicted gap conductance versus gas pressure for temperatures of [b., d., e.].

The accuracy is better at the [b., d., e.]. It should be noted, however, that the average uncertainties in the measurements are [b., d., e.].

At [b., d., e.], for example, this uncertainty is [b., d., e.].

Contact Conductance

The data were obtained from the measurements of GARNIER and BEGEJ (Ref. 4-5). Only measurements taken under vacuum conditions were used. The measurements were taken from samples with two different surface conditions (ISM I and II).

The test conditions are:

- gas temperature : 630 to 736 K
- contact pressure : 0.04 to 14.65 MPa
- average mean-plane gap (due to surface roughnesses): 3.6 and 21.8 μm

4.2.6. Adaptation to Mixed Fuels

The pellet-cladding gap conductance model used for MOX and UO_2-Gd_2O_3 fuel is identical to the UO_2 fuel model.

4.2.7. Model Development Data Range

The pellet-cladding gap conductance model was developed from data which covers the following range of test conditions:

Gas pressure	:[b., d., e.]
Contact pressure	: [b., d., e.]
Fuel surface roughness	: 0.25 - 14.4 μm
Clad surface roughness	: 0.17 - 4.5 μm
Diametral gap	: [b., d., e.]
Gas temperature	: [b., d., e.]
Gas composition	: [b., d., e.]

Its scope encompasses operating conditions normally encountered for fuel rods under irradiation.

The thermal models in the code are validated globally with the centerline temperature measurements. The IFA rod irradiation program at HALDEN (see Global experimental validation page 4-21) includes rods that have a maximum diametral gap of 381 μm and are pressurized with different gas mixtures.

4.3. Fuel Thermal Conductivity

4.3.1. Phenomenon

The thermal conductivity for fully dense unirradiated fuel is a function of temperature (HARDING and MARTIN, Ref. 4-7). Currently, thermal conductivity degradation is taken into account in fuel performance codes by adding resistivity terms for the burnup effect (VAN VLIET and PIRON, Ref. 4-8; LUCUTA, Ref. 4-9; and WIESENACK for the HALDEN project, Ref. 4-10). More recently, LUCUTA proposed a new thermal conductivity law which includes the effects of radiation damage (LUCUTA, Ref. 4-11). The effect of porosity is also taken into account in most thermal conductivity relationships proposed in the literature (J.C. VAN CRAEYNEST, Ref. 4-12).

4.3.2. Model

4.3.2.1. Degradation with Burnup and Radiation Damage

The COPERNIC thermal conductivity relationship for fully dense fuel is derived from the above considerations and has the following form:

[b., e.] Eq. 4-38

where

[b., e.],
[b., e.],
[b., e.], and
[b., e.].

[b., e.]

[b., e.]

The COPERNIC thermal conductivity relationship for fully dense fuel is then:

[b., e.] Eq. 4-39

where

[b., e.],

[b., e.],

[b., e.],

[b., e.], and

[b., e.].

4.3.2.2. Porosity and RIM Model

The correction for porosity is a function of temperature as follows (Ref. 4-12):

$$\lambda_{POR}^{Bu} = \lambda_{100}^{Bu} \cdot (1 - \alpha \cdot POR) \qquad \alpha = 2.58 - 5.8 \cdot 10^{-4} \cdot T_c \qquad \text{Eq. 4-40}$$

where

T_c : temperature (°C), and

POR : porosity fraction.

Fuel rims have been observed on fuel pellet peripheries when the local rim burnup exceeds a value of approximately [e.] or when the average pellet burnup exceeds a value of approximately [e.]. The rim porosity has also been observed [e.]. The following rim model was selected based upon these observations:

[b., e.] Eq. 4-41

where

B_S : [b., e.],

B_A : average pellet burnup,

C_3 : [b., e.], and

C_4 : [b., e.].

and

[b., d.] Eq. 4-42

where

POR : porosity fraction,
r : [b., e.]
r_S : [b., e.], and
C_5 : [b., e.].

[b., e.] Eq. 4-43

4.3.3. Adaptation to Mixed Fuels

The COPERNIC UO_2 thermal conductivity relationship has been adapted to mixed oxide and gadolinia fuels with the following modifications.

4.3.3.1. MOX

[b., d.] Eq. 4-44

where

x = 2.00 - O/M,
F(y) = [b., d.],
F(y) = [b., d.],
O/M : oxygen to metal ratio, and
y : Pu content (weight fraction).

4.3.3.2. UO_2-Gd_2O_3

The ratio of the thermal conductivity of gadolinia bearing fuel to UO_2 fuel [r (z,T) = $\lambda(UGd)UO_2$ / $\lambda(UO_2)$] is:

[b., d.] Eq. 4-45

where

z : Gadolinium content (weight%),

T_k : temperature (K), and

D is given by the following expression:

[b., d.] Eq. 4-46

4.3.4. Experimental Validation

The fuel thermal conductivity model was validated with the COPERNIC centerline temperature predictions from the experimental validation database (see Global experimental validation, page 4-21).

4.3.5. Validity Range

The validity range of this model corresponds to the code benchmarking ranges described in chapter 1.

4.4. Heat Transfer Gap Closure

4.4.1. Phenomenon

As the fuel rod is initially brought up to power, the fuel pellets crack and breakup. The pellet fragments move outward opening up internal gaps and closing the diametral gap between the pellets and cladding. There is a random nature to this initial relocation with some fragments moving outward very little or moving only in conjunction with their neighbors while others move outward until constrained by the cladding. The newly created free surfaces of the pellet fragments bulge due the radial thermal gradient (WALTON and MATHESON, Ref. 4-14). This phenomenon is modelled by an [b., d.].

The thermal gap is then:

[b., d.] Eq. 4-47

4.4.2. Model

A comparison of open gap COPERNIC centerline temperature predictions and measurements

indicated that a [b., d., e.]. This observation lead to the following empirical relationship:

[b., d., e.] Eq. 4-48

where

[b., d., e.],

[b., d., e.],

[b., d., e.].

The heat transfer gap multiplier X is shown versus the mechanical radial hot gap in Figure 4-13.

4.4.3. Adaptation to Mixed Fuels

The heat transfer gap multiplier X used for MOX and UO_2-Gd_2O_3 fuels is identical to the UO_2 fuel model.

4.4.4. Experimental Validation

The heat transfer gap multiplier X is validated by comparing the COPERNIC centerline temperature predictions with measurements from the experimental validation database (see Global Experimental Validation, page 4-21).

4.4.5. Validity Range

The validity range of this model corresponds to the code benchmarking ranges described in chapter 1.

4.5. Fuel Pellet Radial Power Profiles

4.5.1. Phenomenon

The thermal power produced within the fuel corresponds to the volumetric distribution of fissions. The latter depends on the initial isotopic distribution within the fuel and the irradiation conditions (temperature, power, environment, ...). These conditions establish the radial distribution for both the neutron flux and the resulting isotopic composition. The primary phenomena involved are:

- attenuation of the neutron flux towards the pellet center due to self-shielding and capture,
- fissile atom depletion within the pellet,
- the progressive enrichment of a fine Pu peripheral layer through captures in U238,
- burnout of a burnable absorber like gadolinium.

4.5.2. Model

The radial power distributions within the pellet were determined separately with the APOLLO2 neutronic transport code (Ref. 4-15). These predictions produced tabulated data which were incorporated in COPERNIC.

Sensitivity studies were run to define the calculational basis for UO_2 fuel. These are:

- an infinite medium cell layout,
- a uniform temperature for all isotopes (except U238),
- a radial temperature profile for U238, and
- a self-shielding calculation at BOL.

The radial mesh must be sufficiently fine towards the pellet outer edge to correctly represent the peripheral rim effect. Better accuracy at high burnups is obtained with 20 rings.

4.5.3. Available Options

4.5.3.1. Generic Tables for UO_2

The generic tables for UO_2 were established for:

[d., e.]

4.5.3.2. Tables for MOX

MOX generic tables were established for:

[d., e.]

4.5.3.3. Tables for UO_2-Gd_2O_3

[d., e.]

4.5.4. Experimental Validation

The radial burnup distributions obtained with the APOLLO2 tables were validated with radial Neodymium profiles which were obtained with Electron Probe Micro Analyses (EPMA). The rods used are given in Table 4-3.

The validation of the generic UO_2 tables was performed with a number of samples from PWR rods that had two initial enrichments and a variety of burnups (Figures 4-14 to 4-26). Good agreement between measurements and predictions is observed in these figures.

The measured to predicted comparison for the MOX generic tables was performed [e.]. No allowance is made for the scatter in the radial power due to the presence of Pu-rich spots and the fuel is assumed to be homogeneous in the calculations. Therefore, the measured to predicted comparison has a wide scatter; however, the temperature benchmark results for MOX fuel are satisfactory as shown later in the last section describing the global experimental validation. Note that the periphery effect for MOX is much smaller than UO_2 at a comparable burnup (Figure 4-27).

4.5.5. Range of Application

- UO_2 generic tables:	U235 enrichment [d., e.]
	Burnup [d., e.]
- MOX generic tables:	Pu content [d., e.]
	Burnup [d., e.]
- UO_2-Gd_2O_3 specific tables:	Gd_2O_3 content [d., e.]
	User specified input

4.6. Global Experimental Validation

An accurate estimate of fuel temperatures is needed to assess the thermal/mechanical behavior of a fuel rod. A global validation performed by comparing the COPERNIC centerline temperature predictions with measurements ensures that the thermal models are interacting satisfactorily. The global validation takes into account all of the following thermal models and physical phenomena:

- heat transfer between the coolant and fuel rod outside surface (page 4-1),
- heat flow through the cladding waterside corrosion (page 8-1),
- heat transfer across the pellet-cladding gap (page 4-2),
- fuel thermal conductivity (page 4-13),
- heat transfer gap closure (page 4-17), and
- radial power profile in the pellet (page 4-19).

4.6.1. Results on the Experimental Validation Database for UO_2 Fuels

4.6.1.1. FRAMATOME Database

The characteristics of these rods are given in Table 4-4.

[b., d.]

[b., d.]

- HBC [e.]:

Task 3 of the HBC program (Ref. 4-22) included [e.] with UO_2 fuel of a BELGONUCLEAIRE design (powder UO_2/ADU) that had been irradiated to a burnup of [d.] in the BR3 reactor. [e.].

Figure 4-34 shows the predicted radial temperature profile at [e.].

4.6.1.2. US/NRC Database

The characteristics of the rods from HALDEN fuel assemblies IFA 431, IFA 432, IFA 513, IFA 527 and IFA 562, are listed in Table 4-5. [e.].

- Assembly IFA 431:

The IFA 431 assembly was designed in July 1974 to test the effects of gap size, pellet density, and densification on fuel temperatures. This assembly was irradiated from June 1975 to February 1976 and attained a burnup of 4300 MWd/tU. Each rod of this assembly contained a thermocouple at the top and bottom of the fuel stack.

Each rod was designed to test a specific parameter:

Rod 1: Reference rod (94.6% TD, stable fuel, 228.6 µm diametral gap, 1 atmosphere helium).

Rod 2: Fuel densification. This rod was designed with a large gap to simulate rapid densification (94.6% TD, stable fuel, 381 µm diametral gap, 1 atmosphere helium).

Rod 3: Small initial gap and high powers. These two parameters produce rapid pellet-clad gap closure leading to high gap conductances which minimize the pellet-clad temperature differences (94.6% TD, stable fuel, 50.8 µm diametral gap, 1 atmosphere helium).

Rod 5: Impact of a low initial density on a low densifying fuel (91.1% TD, stable fuel, 228.6 µm diametral gap, 1 atmosphere helium).

Rod 6: Study of densification kinetics (91.44% TD, 228.6 µm diametral gap, 1 atmosphere helium). The fuel of this rod densified approximately 3%. This was confirmed by density measurements and fuel stack length and pellet diameter reductions. Despite this large densification, the temperatures remained practically identical to Rod 1 which had little densification (Ref. 4-25). These relatively low temperatures were confirmed with the measured fission gas release which was very small (0.25% at 4300 MWd/tU).

Figures 4-35 to 4-44 show the measured and predicted centerline temperatures for the inlet and outlet thermocouples for each of the IFA 431 rods.

Temperatures at both thermocouples are [b., e.] for rods 1, 2, and 5. Rod 6 (low density) and Rod 3 (small initial gap) temperatures are [b., e.].

The measured to predicted (M/P) means and standard deviations (SD) for the IFA 431 data are presented in the following table:

FA ID	Thermocouple	M / P Mean	Std Dev
IFA 431-1	INLET	[b., d.]	[b., d.]
IFA 431-1	OUTLET	[b., d.]	[b., d.]
IFA 431-2	INLET	[b., d.]	[b., d.]

FA ID	Thermocouple	M / P Mean	Std Dev
IFA 431-2	OUTLET	[b., d.]	[b., d.]
IFA 431-3	INLET	[b., d.]	[b., d.]
IFA 431-3	OUTLET	[b., d.]	[b., d.]
IFA 431-5	INLET	[b., d.]	[b., d.]
IFA 431-5	OUTLET	[b., d.]	[b., d.]
IFA 431-6	INLET	[b., d.]	[b., d.]
IFA 431-6	OUTLET	[b., d.]	[b., d.]

- Assembly IFA 432:

Assembly IFA-432 was similar to assembly IFA-431, but the power levels were higher. IFA-432 reached a burnup of 46000 MWd/tU. Each fuel rod contained one parameter (gap size, initial density, densification) that was modified. The instrumentation included thermocouples that were located at the top and bottom of each rod (Ref. 4-26).

The condition of the rods following irradiation was consistent with the power-temperature histories. The fission gas releases, estimated from sorbed gas analysis and ceramographic examinations, are Rod 2: 30% (+/-10%), Rod 3: 10% (+/-10%), and Rod 5: 30% (+/-10%).

Figures 4-45 to 4-52 present the measured and predicted centerline temperatures for the inlet and outlet thermocouples of the IFA 432 Rods. Rod 1 [b., e.]. This rod is similar to the IFA 431-1 Rod which is [b., e.]. The power levels at the inlet thermocouple of Rod IFA 432-1 and the outlet thermocouple of Rod IFA 431-1 are approximately equal.

The inlet temperatures of Rod 2, which had a large as fabricated gap, [b., e.].

Both thermocouples of Rod 3 [b., e.]. This rod is similar to IFA 431 Rod-3 which is [b., e.].

Rod 5 is [b., e.]]. Both thermocouples of Rod 6 are [b., e.]. The characteristics of Rod 6 are identical to Rod 5, except for the densification kinetics; Rod 6 is unstable while Rod 5 is stable.

The measured to predicted (M/P) means and standard deviations (SD) for the IFA 432 rods are listed in the following table:

FA ID	Thermocouple	M/P Mean	Std Dev
IFA 432-1	INLET	[b., d.]	[b., d.]
IFA 432-1	OUTLET	[b., d.]	[b., d.]
IFA 432-2	INLET	[b., d.]	[b., d.]
IFA 432-3	INLET	[b., d.]	[b., d.]
IFA 432-3	OUTLET	[b., d.]	[b., d.]
IFA 432-5	INLET	[b., d.]	[b., d.]
IFA 432-6	INLET	[b., d.]	[b., d.]
IFA 432-6	OUTLET	[b., d.]	[b., d.]

- Assemblies IFA 513 & 527:

The IFA 513 & 527 tests were designed primarily to:

. obtain additional data on the effect of gas mixtures (at various pressures), and the fracturing and relocation of pellet fragments on fuel temperatures,

. and to quantify possible deviations between rods of the same design that are operating under similar conditions (Ref. 4-27).

To achieve these goals,

. IFA 513 Rod 1 was identical to IFA 431 and IFA 432 Rod 1 (95% TD, UO_2 stable, 9% U235 enrichment, 100% helium at 1 atmosphere and 226 µm diametral gap),

. IFA 513 Rod 2 and IFA 513 Rod 6 are identical to IFA 513 Rod 1, except that the initial composition of the gaseous mixture differed as shown below:

* IFA 513 Rod 2: 3 atmospheres - helium (100%),

* IFA 513 Rod 6: 1 atmosphere - helium (77%) / xenon (23%),

. IFA 527 Rod 1 was identical to IFA 431 and IFA 432 Rod 1 except that the initial composition of the gaseous mixture was 1 atmosphere, xenon (100%).

The IFA 513 assembly was irradiated from November 1978 to January 1980 and the IFA 527 assembly from July 1980 and April 1981.

The measured and predicted centerline temperatures for both thermocouples of the IFA 513 and IFA 527 rods are shown in Figures 4-53 to 4-59.

The measured temperatures of the IFA 513 rods are [b., e.]. The xenon filled IFA 527 Rod 1 measured temperatures are [b., e.].

The measured to predicted (M/P) means and standard deviations (SD) for the IFA 513 and 527 rods are listed in the following table:

FA ID	Thermocouple	M/P Mean	Std Dev
IFA 513-1	INLET	[b., d.]	[b., d.]
IFA 513-1	OUTLET	[b., d.]	[b., d.]
IFA 513-2	INLET	[b., d.]	[b., d.]
IFA 513-6	INLET	[b., d.]	[b., d.]
IFA 513-6	OUTLET	[b., d.]	[b., d.]
IFA 527-1	INLET	[b., d.]	[b., d.]
IFA 527-1	OUTLET	[b., d.]	[b., d.]

4.6.1.3. HALDEN PROJECT Database

The characteristics of these rods, from HALDEN fuel assemblies IFA [b.] and IFA [b.], are listed in Table 4-5. The radial power profile tables were generated to match the irradiation conditions in the HALDEN reactor.

- Assembly IFA [b.]:

[b.]. Rod 1 was irradiated in the Halden reactor, up to a burnup of [b.] (Ref. 4-28).

Figure 4-60 presents the measured and predicted centerline temperatures for [b.]. If the data at a power level greater than [b., d.] are considered, [b., d.].

- Assembly IFA [b.]:

[b., d.]

4.6.2. Validation of Mixed Oxide Fuels

4.6.2.1. MOX

[b., d.]

4.6.2.2. UO_2-Gd_2O_3

The COPERNIC gadolinia centerline temperature predictions were benchmarked with the measurements from 2 rods of the GDGRIF program: one rod that was ramped to fuel melt and another rod from the HALDEN project [e.].

- [e.]:

[b., d.]

- HBC [e.]:

[b., d.]

- IFA [e.]:

[b., d.]

4.6.3. Uncertainties

4.6.3.1. FRAMATOME Database

Figure 4-69 presents the measured to predicted centerline fuel temperature ratio (M/P ratio) versus burnup for the [b., d.].

4.6.3.2. US/NRC Halden Database

Further examination of the IFA 431 and 432 experiments reveals that the fuel that is not representative of currently produced fuel [b, e.]. This fuel includes the 431-2 & 432-2 large gap rods and the 431-5, 431-6, 432-5 & 432-6 low density rods. IFA 527 rod 1 (100% xenon at 1 atmosphere) is also not representative of fuel currently produced.

Excluding these 12 rods, results in the following database:

FA ID	Thermocouple 1	Thermocouple 2
IFA 431-1	INLET	OUTLET
IFA 431-3	INLET	OUTLET
IFA 432-1	INLET	OUTLET
IFA 432-3	INLET	OUTLET
IFA 513-1	INLET	OUTLET
IFA 513-2	INLET	
IFA 513-6	INLET	OUTLET

Figure 4-70 presents the measured to predicted (M/P) ratios for these 13 IFA rods [b., e.]. The measured temperatures range from [b., e.], with linear power levels up to [b., d., e.] kW/m and a peak burnup of [b., d., e.].

4.6.3.3. HALDEN PROJECT Database

The measured to predicted (M/P) ratios versus burnup [b.] are presented in Figure 4-71. The measured temperatures range from [b.], with linear powers of up to [b., d., e.] kW/m and a peak burnup of [b.]. The 822 points for assembly [e.] yield a [b., d.].

4.6.3.4. Summary

• The measured to predicted (M/P) centerline fuel temperature means and standard deviations (SD) are listed in the following table:

Rod ID	Comments	Number of points	M/P Mean	Std Dev
[b., d., e.]				

• Figures 4-72 and 4-73 show the measured to predicted (M/P) ratios for the [b., d., e.] points as a function of the rod average burnup and linear heat generation rate: the trend is excellent. The measured and predicted centerline fuel temperatures for these data are shown plotted in Figure 4-74. The above table and Figure 4-72 show that [b., e.].

•

[b., e.]

This is discussed in more detail in chapter 12.

This page intentionally left blank.

REFERENCES

Ref. 4-1 D. WESLEY et M. YOVANOVICH, *A New Gaseous Gap Conductance Relationship*, Nuclear Technology, Vol. 72, Jan. 1986, 70-74.

Ref. 4-2 D.L. HAGRMAN, Matpro-Version 11 (Rev. 2), *A Handbook of Materials Properties for Use in the Analysis of Light Water Reactor Fuel Rod Behavior*, NUREG/CR0497, TREE-1280, Rev. 2, US NRC (Aug. 1981).

Ref. 4-3 B.B. MIKIC, *Thermal Contact Conductance: Theoretical Considerations*, Int. J. Heat Mass Transfer, vol. 17, 1973.

Ref. 4-4 G. JACOBS et N. TODREAS, *Thermal Contact Conductance in Reactor Fuel Elements*, Nuclear Science and Engineering, Vol. 50, 1973.

Ref. 4-5 J.E. GARNIER et S. BEGEJ, *Ex-reactor Determination of Thermal Gap and Contact Conductance Between Uranium Dioxide : Zircaloy-4 Interfaces*, Stage I : Low Gas Pressure, NUREG/CR-0300 (1979) Vol. 1.

Ref. 4-6 J.E. GARNIER et S. BEGEJ, *Ex-reactor Determination of Thermal Gap and Contact Conductance Between Uranium Dioxide: Zircaloy-4 Interfaces*, Stage II: High Gas Pressure, NUREG/CR-0300 (1980) Vol. 2.

Ref. 4-7 J.H. HARDING, D.G. MARTIN, *A Recommendation for the Thermal Conductivity of UO2*, JNM 166 (1989), pp 223-226.

Ref. 4-8 J. VAN VLIET, J.P. PIRON, *Fuel Properties at High Burnup*, HBC Task 4 Theoretical Support, Part I, HBC 89/08 (March 1989).

Ref. 4-9 P.G. LUCUTA, Hj. MATZKE, R.A. VERALL, H.A. TASMAN, *Thermal conductivity of SIMFUEL*, JNM 188 (1992), pp 198-204.

Ref. 4-10 W. WIESENACK, *Assessment of UO_2 conductivity degradation based on in-pile temperature data*, OECD HALDEN reactor project, Report HWR 469, 1996.

Ref. 4-11 P.G. LUCUTA, HJ. MATZKE, IJ. HASTINGS, *A pragmatic approach to modelling thermal conductivity of irradiated UO_2 fuel: review and recommendations*, JNM 232 (1996), pp 166-180.

Ref. 4-12 J.C. VAN CRAEYNEST, J.P. STORA, *Effet de la porosité sur la variation de la conductibilité thermique du bioxyde d'uranium en fonction de la température*, JNM 37 (1970), pp 153-158.

Ref. 4-13 ME. CUNNINGHAM, MD. FRESHLEY, DD. LANNING, *Development and characteristics of the RIM region in high burnup UO_2 fuel pellets*, JNM 188, 1992, pp 19-27.

Ref. 4-14 LA. WALTON, J.E MATHESON, *Fumac - A New Model for Light Water Reactor fuel Relocation and pellet-cladding Interaction*, Nuclear Technology, Vol. 64, February 1984.

Ref. 4-15 BAW-10228P, *SCIENCE, Topical Report*, February 1998.

Ref. 4-16 M. CHARLES et al., *Utilization of "Contact" Experiments to Improve the Fission Gas Release Knowledge in PWR Fuel Rods*, IAEA Specialists' meeting - Preston 1982.

Ref. 4-17 M. BRUET, *Contact 1 and 2 Experiments: Behaviour of PWR Fuel Rod up to 15000 MWd/tU*, IAEA - Specialist's meeting - Blackpool 1980.

Ref. 4-18 M. CHARLES, *Mechanisms of Fission Gas Release from Different Types of Fuel Rods During Normal Operation, Results and Analysis of Contact Experiments*, ANS Topical Meeting on LWR Fuel Performance, April 1985.

Ref. 4-19 D. HOSTEIN, *Compte-rendu de l'irradiation "BOSS 09"*, IRDI/DERPE/SPS/SERI/87-106, Avril 1987.

Ref. 4-20 E. PORROT, *Thermal behavior and FGR of MOX Fuel - Comparision with UO2 in the THERMOX and GRIMOX experimental programs*, IAEA Technical Commitee on Recycling of Plutonium and Uranium in Water Reactor Fuels, Cadarache (FRANCE), November 1989.

Ref. 4-21 A. CHOTARD, *Out-of-Pile Physical Properties and In-Pile Thermal Conductivity of $(U, Gd)O_2$*, IAEA - Technical Committee meeting, Vienna, October 1986.

Ref. 4-22 P. BLANPAIN, *HBC Task* [d.] , HBC 89/10, April 1989.

Ref. 4-23 [d.].

Ref. 4-24 [d.].

Ref. 4-25 C. NEALLEY, D.D. LANNING, M.E. CUNNINGHAM, C.R. HANN, *Post-Irradiation Data Analysis for NRC/PNL Halden Assembly IFA-431*, NUREG/CR-0797 PNL-2975 R3, October 1979.

Ref. 4-26 D.D. LANNING, *Irradiation History and Final Postirradiation Data for IFA-432*, NUREG/CR-4717 PNL-5971 R3, November 1986.

Ref. 4-27 E.R. BRADLEY, M.E. CUNNINGHAM, D.D. LANNING, R.E. WILLIFORD, *Data Report for the Instrumented Fuel Assembly IFA-513*, NUREG/CR-1838 PNL-3637 R3, August 1981.

Ref. 4-28 M.T. ALVAREZ, M. HIRAI, W. WIESENACK, *Analysis of the thermal behaviour of Gd-Bearing Fuel in IFA-515.10*, HWR-470 (OECD HALDEN Reactor Project).

Ref. 4-29 P. LOSONEN, *Early-In-Life Irradiation of IFA-562.2 (The Ultra High Burn-up Experiment)*, HWR-247 (OECD HALDEN Reactor Project).

Ref. 4-30 L. MERTENS, *HBC Topical Report, Task 3, HBC-5* [d.], HBC 94/47, November 94.

This page intentionally left blank.

FIGURES

FIGURE 4-1 ROUGHNESS FACTOR VERSUS DIMENSIONLESS GAP FOR DIFFERENT DIMENSIONLESS TEMPERATURE JUMP LENGTHS

[b.]

FIGURE 4-2 COMPARISON OF MEASURED AND PREDICTED GASEOUS CONDUCTANCES

[b.]

FIGURE 4-3 COMPARISON OF MEASURED AND PREDICTED GASEOUS CONDUCTANCES [b.]

[b.]

FIGURE 4-4 COMPARISON OF MEASURED AND PREDICTED GASEOUS CONDUCTANCES [b.]

[b.]

FIGURE 4-5 COMPARISON OF MEASURED AND PREDICTED GASEOUS CONDUCTANCES [b.]

[b.]

FIGURE 4-6 COMPARISON OF MEASURED AND PREDICTED GASEOUS CONDUCTANCES [b.]

[b.]

FIGURE 4-7 COMPARISON OF MEASURED AND PREDICTED GASEOUS CONDUCTANCES [b.]

[b.]

FIGURE 4-8 COMPARISON OF MEASURED AND PREDICTED GASEOUS CONDUCTANCES [b.]

[b.]

FIGURE 4-9 COMPARISON OF MEASURED AND PREDICTED GAP CONDUCTANCES [b.]

[b.]

FIGURE 4-10 COMPARISON OF MEASURED AND PREDICTED GAP CONDUCTANCES [b.]

[b.]

FIGURE 4-11 MEASURED AND PREDICTED GAP CONDUCTANCES VS PRESSURE [b.]

[b.]

FIGURE 4-12 MEASURED AND PREDICTED GAP CONDUCTANCE VS PRESSURE [b.]

[b.]

FIGURE 4-13 HEAT TRANSFER GAP MULTIPLIER X VS RADIAL MECHANICAL HOT GAP

[b.]

FIGURE 4-14 COMPARISON OF MEASURED (NEODYMIUM) AND PREDICTED RADIAL POWER PROFILES [b.]

[b.]

FIGURE 4-15 COMPARISON OF MEASURED (NEODYMIUM) AND PREDICTED RADIAL POWER PROFILES [b.]

[b.]

FIGURE 4-16 COMPARISON OF MEASURED (NEODYMIUM) AND PREDICTED RADIAL POWER PROFILES [b.]

[b.]

FIGURE 4-17 COMPARISON OF MEASURED (NEODYMIUM) AND PREDICTED RADIAL POWER PROFILES [b.]

[b.]

FIGURE 4-18 COMPARISON OF MEASURED (NEODYMIUM) AND PREDICTED RADIAL POWER PROFILES [b.]

[b.]

FIGURE 4-19 COMPARISON OF MEASURED (NEODYMIUM) AND PREDICTED RADIAL POWER PROFILES [b.]

[b.]

FIGURE 4-20 COMPARISON OF MEASURED (NEODYMIUM) AND PREDICTED RADIAL POWER PROFILES [b.]

[b.]

FIGURE 4-21 COMPARISON OF MEASURED (NEODYMIUM) AND PREDICTED RADIAL POWER PROFILES [b.]

[b.]

FIGURE 4-22 COMPARISON OF MEASURED (NEODYMIUM) AND PREDICTED RADIAL POWER PROFILES [b.]

[b.]

FIGURE 4-23 COMPARISON OF MEASURED (NEODYMIUM) AND PREDICTED RADIAL POWER PROFILES [b.]

[b.]

FIGURE 4-24 COMPARISON OF MEASURED (NEODYMIUM) AND PREDICTED RADIAL POWER PROFILES [b.]

[b.]

FIGURE 4-25 COMPARISON OF MEASURED (NEODYMIUM) AND PREDICTED RADIAL POWER PROFILES [b.]

[b.]

FIGURE 4-26 COMPARISON OF MEASURED (NEODYMIUM) AND PREDICTED RADIAL POWER PROFILES [b.]

[b.]

FIGURE 4-27 COMPARISON OF MEASURED (NEODYMIUM) AND PREDICTED RADIAL POWER PROFILES - MOX [b.]

[b.]

FIGURE 4-28 MEASURED AND PREDICTED FUEL TEMPERATURES VS BURNUP [b.]

[b.]

FIGURE 4-29 MEASURED AND PREDICTED FUEL TEMPERATURES VS BURNUP [b.]

[b.]

FIGURE 4-30 MEASURED AND PREDICTED FUEL TEMPERATURES VS BURNUP [b.]

[b.]

FIGURE 4-31 MEASURED AND PREDICTED FUEL TEMPERATURES VS BURNUP [b.]

[b.]

FIGURE 4-32 MEASURED AND PREDICTED FUEL TEMPERATURES VS BURNUP [b.]

[b.]

FIGURE 4-33 MEASURED AND PREDICTED FUEL TEMPERATURES VS TIME [b.]

[b.]

FIGURE 4-34 [e.]

[b.]

FIGURE 4-35 MEASURED AND PREDICTED FUEL TEMPERATURES VS BURNUP (IFA 431-1, INLET)

[b.]

FIGURE 4-36 MEASURED AND PREDICTED FUEL TEMPERATURES VS BURNUP (IFA 431-1, OUTLET)

[b.]

FIGURE 4-37 MEASURED AND PREDICTED FUEL TEMPERATURES VS BURNUP (IFA 431-2, INLET)

[b.]

FIGURE 4-38 MEASURED AND PREDICTED FUEL TEMPERATURES VS BURNUP (IFA 431-2, OUTLET)

[b.]

FIGURE 4-39 MEASURED AND PREDICTED FUEL TEMPERATURES VS BURNUP (IFA 431-3, INLET)

[b.]

FIGURE 4-40 MEASURED AND PREDICTED FUEL TEMPERATURES VS BURNUP (IFA 431-3, OUTLET)

[b.]

FIGURE 4-41 MEASURED AND PREDICTED FUEL TEMPERATURES VS BURNUP (IFA 431-5, INLET)

[b.]

FIGURE 4-42 MEASURED AND PREDICTED FUEL TEMPERATURES VS BURNUP (IFA 431-5, OUTLET)

[b.]

FIGURE 4-43 MEASURED AND PREDICTED FUEL TEMPERATURES VS BURNUP (IFA 431-6, INLET)

[b.]

FIGURE 4-44 MEASURED AND PREDICTED FUEL TEMPERATURES VS BURNUP (IFA 431-6, OUTLET)

[b.]

FIGURE 4-45 MEASURED AND PREDICTED FUEL TEMPERATURES VS BURNUP (IFA 432-1, INLET)

[b.]

FIGURE 4-46 MEASURED AND PREDICTED FUEL TEMPERATURES VS BURNUP (IFA 432-1, OUTLET)

[b.]

FIGURE 4-47 MEASURED AND PREDICTED FUEL TEMPERATURES VS BURNUP (IFA 432-2, INLET)

[b.]

FIGURE 4-48 MEASURED AND PREDICTED FUEL TEMPERATURES VS BURNUP (IFA 432-3, INLET)

[b.]

FIGURE 4-49 MEASURED AND PREDICTED FUEL TEMPERATURES VS BURNUP (IFA 432-3, OUTLET)

[b.]

FIGURE 4-50 MEASURED AND PREDICTED FUEL TEMPERATURES VS BURNUP (IFA 432-5, INLET)

[b.]

FIGURE 4-51 MEASURED AND PREDICTED FUEL TEMPERATURES VS BURNUP (IFA 432-6, INLET)

[b.]

FIGURE 4-52 MEASURED AND PREDICTED FUEL TEMPERATURES VS BURNUP (IFA 432-6, OUTLET)

[b.]

FIGURE 4-53 MEASURED AND PREDICTED FUEL TEMPERATURES VS BURNUP (IFA 513-1, INLET)

[b.]

FIGURE 4-54 MEASURED AND PREDICTED FUEL TEMPERATURES VS BURNUP (IFA 513-1, OUTLET)

[b.]

FIGURE 4-55 MEASURED AND PREDICTED FUEL TEMPERATURES VS BURNUP (IFA 513-2, INLET)

[b.]

FIGURE 4-56 MEASURED AND PREDICTED FUEL TEMPERATURES VS BURNUP (IFA 513-6, INLET)

[b.]

FIGURE 4-57 MEASURED AND PREDICTED FUEL TEMPERATURES VS BURNUP (IFA 513-6, OUTLET)

[b.]

FIGURE 4-58 MEASURED AND PREDICTED FUEL TEMPERATURES VS BURNUP (IFA 527-1, INLET)

[b.]

FIGURE 4-59 MEASURED AND PREDICTED FUEL TEMPERATURES VS BURNUP (IFA 527-1, OUTLET)

[b.]

FIGURE 4-60 MEASURED AND PREDICTED FUEL TEMPERATURES VS BURNUP (IFA [b.])

[b.]

FIGURE 4-61 MEASURED AND PREDICTED FUEL TEMPERATURES VS BURNUP (IFA [b.])

[b.]

FIGURE 4-62 MEASURED AND PREDICTED FUEL TEMPERATURES VS BURNUP (IFA [b.])

[b.]

FIGURE 4-63 MEASURED AND PREDICTED FUEL TEMPERATURES VS BURNUP [b.]

[b.]

FIGURE 4-64 MEASURED AND PREDICTED FUEL TEMPERATURES VS BURNUP [b.]

[b.]

FIGURE 4-65 MEASURED AND PREDICTED FUEL TEMPERATURES VS BURNUP [b.]

[b.]

FIGURE 4-66 MEASURED AND PREDICTED FUEL TEMPERATURES VS BURNUP [b.]

[b.]

FIGURE 4-67 [e.]

[b.]

FIGURE 4-68 MEASURED AND PREDICTED FUEL TEMPERATURES VS BURNUP (IFA [b.])

[b.]

FIGURE 4-69 MEASURED/PREDICTED FUEL CENTERLINE TEMPERATURE RATIO VS BURNUP (FRAMATOME DATABASE)

[b.]

FIGURE 4-70 MEASURED/PREDICTED FUEL CENTERLINE TEMPERATURE RATIO VS BURNUP (US/NRC DATABASE)

[b.]

FIGURE 4-71 MEASURED/PREDICTED FUEL CENTERLINE TEMPERATURE RATIO VS BURNUP (HALDEN PROJECT DATABASE)

[b.]

FIGURE 4-72 MEASURED/PREDICTED FUEL CENTERLINE TEMPERATURE RATIO VS BURNUP (ALL DATA)

[b.]

FIGURE 4-73 MEASURED/PREDICTED FUEL CENTERLINE TEMPERATURE RATIO VS LHGR (ALL DATA)

[b.]

FIGURE 4-74 PREDICTED VS MEASURED FUEL CENTERLINE TEMPERATURES

[b.]

This page intentionally left blank.

TABLES

TABLE 4-1 MEASURED AND PREDICTED GAP CONDUCTANCES (ATMOSPHERIC PRESSURE)

[b.]

[b.]

[b.]

[b.]

TABLE 4-2 MEASURED AND PREDICTED GAP CONDUCTANCES (HIGH GAS PRESSURE)

[b.]

[b.]

[b.]

[b.]

[b.]

[b.]

[b.]

[b.]

TABLE 4-3 NEODYNIUM RADIAL PROFILES

Reactor	Rod ID	Number of Cycles	Enrichment (%)	Axial Location (from bottom of column)	Local Burnup

[b.]

TABLE 4-4 FRAMATOME MEASURED FUEL CENTERLINE TEMPERATURE DATABASE (UO_2)

Rod ID	Burnup (MWd/tU)	Diametral Gap (µm)	Gas Composition	Density (%TD)	Enrichment (%)	Pellet Diameter (mm)	LHGR (KW/m)	Clad Temperature (°C)	System Pressure (bar)
[b.]									

(*): Constant during the irradiation

(**): Mother rod

TABLE 4-5 US/NRC & HALDEN MEASURED FUEL CENTERLINE TEMPERATURE DATABASE (UO_2)

Rod ID	Burnup (MWd/tU)	Diametral Gap (μm)	Gas Composition	Density (%TD)	Enrichment (%)	Pellet Diameter (mm)	LHGR (kW/m)	Clad Temperature (°C)	System Pressure (bar)
IFA 431-1	4509	228.6	He (100%) - 1 atm	94.56	9	10.681	2.6 - 36.0	237.2	34.47
IFA 431-2	4681	381	He (100%) - 1 atm	94.56	9	10.528	2.7 - 36.0	237.2	34.47
IFA 431-3	4887	50.8	He (100%) - 1 atm	94.56	9	10.859	2.6 - 39.0	237.2	34.47
IFA 431-5	4517	228.6	He (100%) - 1 atm	91.1	9	10.681	2.7 - 35.0	237.2	34.47
IFA 431-6	4447	228.6	He (100%) - 1 atm	91.44	9	10.681	2.6 - 35.0	237.2	34.47
IFA 432-1	10647	228.6	He (100%) - 1 atm	94.87	9	10.681	2.5 - 45.0	237.2	34.47
IFA 432-2	13973	381	He (100%) - 1 atm	95	9	10.528	2.7 - 41.0	237.2	34.47
IFA 432-3	43000	76.2	He (100%) - 1 atm	94.87	9	10.833	2.7 - 42.0	237.2	34.47
IFA 432-5	44000	228.6	He (100%) - 1 atm	92	9	10.681	2.7 - 42.0	237.2	34.47
IFA 432-6	14186	228.6	He (100%) - 1 atm	92	9	10.681	2.7 - 45.0	237.2	34.47
IFA 513-1	10544	226	He (100%) - 1 atm	95.02	9	10.683	3.2 - 42.0	237.2	34.47
IFA 513-2	5928	226	He (100%) - 3 atm	95.02	9	10.683	3.2 - 33.0	237.2	34.47
IFA 513-6	10290	226	He:Xe (77:23%) - 1 atm	95.04	9	10.683	3.2 - 42.0	237.2	34.47

Rod ID	Burnup (MWd/tU)	Diametral Gap (µm)	Gas Composition	Density (% TD)	Enrichment (%)	Pellet Diameter (mm)	LHGR (kW/m)	Clad Temperature (°C)	System Pressure (bar)
IFA 527-1	376	228.6	Xe (100%) - 1 atm	95.04	9	10.681	2.5 - 18.0	237.2	34.47

[b.]

This page intentionally left blank.

5. FISSION GAS RELEASE

5.1. Phenomenon

The fission of atoms within UO_2 fuel pellets creates noble gas atoms: primarily Xenon and to a lesser extent Krypton. These gas atoms are released from the UO_2 fuel pellets by several mechanisms which can be classified in two main groups: an athermal release and a thermal release. The mechanisms involved in the fission gas release are many and complex (Ref. 5-1). Only the phenomena contained in the COPERNIC fission gas release model are described in the following paragraphs.

Athermal release is the result of the displacement of the gas atoms by recoil and knockout and their escape from the pellet through free surfaces (cracks, open pores). This release, which is always present, is temperature-independent and increases with burnup and open porosity. Its amplitude remains small, with [e.].

As its name indicates, thermal release is activated at elevated fuel temperatures. It only occurs above an experimentally observed temperature threshold which decreases with burnup. This phenomenon can be explained by the presence of inter-granular gas, most often observed in the form of lens-shaped intergranular bubbles. Gas atoms migrate from the inside of UO_2 grains to the grain boundaries at a speed which increases with temperature. Initially, these atoms build up at the grain boundaries and there is no release outside the pellet. When the surface density of these atoms at the grain boundaries reaches an incubation threshold value, release occurs. The presence of intergranular gas induces another phenomenon: fission spikes will result in some of the intergranular atoms returning to solution. This induces a "re-solution flow" which partly counteracts the diffusion flow.

The re-solution phenomenon also acts inside the grains. The intragranular atoms recombine into fine intragranular bubbles comprising a few atoms which have a radius on the order of a nanometer. These bubbles are redissolved by the fission spikes. An equilibrium condition exists between recombination and re-solution.

5.2. Model

5.2.1. General Principle

The fractional fission gas release (F) is given by:

$$F = F_{ATH} + F_{TH} \qquad \text{Eq. 5-1}$$

where:

F : ratio of fission gas atoms released from the pellet to the total generated,

F_{ATH} : athermal component, and

F_{TH} : thermal component.

The thermal release is subdivided into steady state release when the irradiation conditions change slowly and transient release when these conditions change rapidly.

5.2.2. Athermal Release

Athermal release arises from the contributions of the recoil/knockout mechanisms [b., e.]. The recoil contribution is negligible. Therefore F_{ATH} is of the form (Ref. 5-1):

$$F_{ATH} = C_1 \cdot \left(\frac{S}{V}\right) \cdot B \qquad \text{Eq. 5-2}$$

where:

C_1 : model parameter,

$\frac{S}{V}$: specific surface of the fuel, and

B : local burnup (MWd/tM).

The following form was chosen:

Eq. 5-3

[b., e.]

C_1 and C_2 have been adjusted to best fit experimental data where [b., e.] (they are, of course, eventually qualified using the whole database):

C_1 = [b., d.], and

C_2 = [b., d.].

[b., e.]:

[b., e.] Eq. 5-4

[b., e.] Eq. 5-5

where:

r : distance [e.],

r_S : pellet radius, and

C_5 : model parameter.

The C_3, C_4 and C_5 constants have been adjusted to obtain a best fit with experimental data where [b., d.]:

C_3 = [b., d.],

C_4 = [b., d.], and

C_5 = [b., d.].

5.2.3. Thermal Release

5.2.3.1. Diffusion Coefficient

The Turnbull, et al. (Ref. 5-2 and Ref. 5-3) relationship is the basis for the diffusion coefficient. The diffusion coefficient D is the sum of three components: D_1, D_2 and D_3. The D_1 term represents the intrinsic diffusion in the absence of irradiation. The D_2 and D_3 terms represent the irradiation induced thermal and athermal contributions. A correction due to the re-solution of the intra-granular atoms is also input (Ref. 5-1 and Ref. 5-4):

$$D = \frac{D_{1+2+3}}{1 + g/b'} \quad \text{Eq. 5-6}$$

where:

$$D_{1+2+3} = D_1 + D_2 + D_3 \qquad \text{Eq. 5-7}$$

and:

g : probability of trapping atoms in the intragranular bubbles, and

b' : probability of re-solution of the intragranular atoms.

The random path relationship (Ref. 5-1) yields:

$$g = D_{1+2+3}/L^2 \qquad \text{Eq. 5-8}$$

where:

L : average path between two coalescences.

From the preceeding equations:

$$D = \frac{1}{\frac{1}{D_{1+2+3}} + \frac{1}{L^2 b'}} \qquad \text{Eq. 5-9}$$

The previous expression shows that the coefficient D saturates at a value equal to $L^2\, b'$ at high temperature.

The expressions for the terms of the diffusion coefficient are:

$$D_1 = D_{01} \cdot exp\left(\frac{-T_{01}}{T_K}\right) \qquad \text{Eq. 5-10}$$

$$D_2 = D_{02} \cdot exp\left(\frac{-T_{02}}{T_K}\right) \cdot \sqrt{\frac{P'}{20}} \qquad \text{Eq. 5-11}$$

$$D_3 = D_{03} \cdot \frac{P'}{20} \qquad \text{Eq. 5-12}$$

where:

D : diffusion coefficient (m^2/s),

P' : linear heat rate of the axial slice (kW/m),

T_K : temperature (K),

and where:

D_{01} = $7.6\ 10^{-10}\ m^2/s$,

T_{01} = 35000 K,

D_{02} = $1.77\ 10^{-15}$ m²/s,

T_{02} = 13800 K,

D_{03} = 2×10^{-21} m²/s, and

$L^2 b'$ = 10^{-15} m²/s.

Figure 5-1 shows the variation in diffusion coefficient D with temperature for P' = 40 kW/m. Four temperature zones can be observed: at low temperatures - athermal irradiation induced diffusion (D_3), at intermediate temperatures - thermal irradiation induced diffusion (D_2), at high temperatures - intrinsic diffusion (D_1). At very high temperatures, there is saturation of the diffusion coefficient D.

5.2.3.2. Incubation Threshold

The incubation threshold expression for thermal release is obtained from the previous diffusion coefficient expression and is based on the article by Dowling, White and Tucker (Ref. 5-5). The fission spikes return some of the gas contained in the intergranular bubbles to solution. The corresponding re-solution flux, J_{rs}, is:

$$J_{rs} = (bN)/2 = D\frac{dc}{dr} \approx D\frac{c_\delta}{\delta} \qquad \text{Eq. 5-13}$$

where:

b : probability of re-solution of the intergranular atoms,

N : surface density at the grain boundaries,

c_δ : average concentration at the grain boundaries, and

δ : thickness of the re-solution zone at the grain boundaries.

Hence:

$$c_\delta = (bN\delta)/(2D) \qquad \text{Eq. 5-14}$$

In addition, it is assumed (Ref. 5-4) that the flux exiting the grain takes the form:

$$J = J_1(1 - c_\delta/(\beta t)) \qquad \text{Eq. 5-15}$$

and:

$$J_1 = \frac{1}{4\pi a^2}\frac{d}{dt}\left[\frac{4}{3}\pi a^3 \beta t F\right] \qquad \text{Eq. 5-16}$$

where:

β : creation rate,

F : fractional gas release,

a : radius of grain (modeled as a sphere), and

t : time.

The Booth diffusion model (Ref. 5-6) yields a best-estimate solution for low releases:

$$F \sim \frac{4}{\sqrt{\pi}}\sqrt{\frac{Dt}{a^2}} \qquad \text{Eq. 5-17}$$

Finally, the surface density trend obeys the following equation:

$$\frac{d}{dt}N' = 4\beta\sqrt{\frac{Dt}{\pi}}\left(1-\frac{Nb\delta}{2D\beta t}\right) \qquad \text{Eq. 5-18}$$

The incubation time t_i is given by the solution of this equation for $t_i = t\,(N_{SAT})$ where N_{SAT} is the surface density threshold value. Two asymptotic solutions of this equation at high and low temperature are obtained for D being constant versus time.

$$T \text{ low: } t_i \sim (bN_{SAT}\delta)/(2D\beta) \qquad \text{Eq. 5-19}$$

$$T \text{ high: } t_i \sim \left(\frac{9}{8\pi}\right)^{1/3}\left(\frac{N_{SAT}}{\beta}\right)^{2/3}\frac{1}{D^{1/3}} \qquad \text{Eq. 5-20}$$

By means of the diffusion coefficient expression, the incubation threshold expression $B_i \sim \beta\, t_i / (6.9 \times 10^{21})$ is deduced. Toward low temperatures,

$$B_i \sim \frac{bN\delta}{2(D_2+D_3)} \qquad \text{Eq. 5-21}$$

and at high temperatures,

$$B_i \sim \left(\frac{9}{8\pi}\right)^{1/3}(N_{SAT})^{2/3}(\beta)^{1/3}\left(\frac{1}{D_1}+L^2b'\right)^{1/3} \qquad \text{Eq. 5-22}$$

Two important observations enabled the authors to combine these two asymptotic expressions into a single expression. First,

$$T_{02} \sim T_{01}/3 \qquad \text{Eq. 5-23}$$

and second, there is a large uncertainty associated with the variables b, δ and N_{SAT}, and hence, with their combination. Therefore, a release threshold solution of the following form is desired:

$$B > B_i \quad \text{where} \quad B_i = \frac{B_1}{\exp\left(-\frac{T_1}{T_K}\right)+\frac{(T_K-T_2)}{T_3}} + B_2 \quad \text{and} \quad T_C > T_4 \qquad \text{Eq. 5-24}$$

where:

T_K : local temperature (K),

T_C : local temperature (°C),

and where:

T_1 = 13800 K,

T_2 = 603 K,

T_3 = 1.59 10^7 K,

T_4 = 650 °C,

B_1 = 1.2 MWd/tM, and

B_2 = 2500.0 MWd/tM.

The model parameters B_1, B_2, T_2, T_3 are used to obtain a fit with the experimental database. The initial values of these parameters were obtained from the average values of the parameters b, δ and N_{SAT}, that were taken from the literature [e.].

Figure 5-2 presents a graphical representation of this threshold. Furthermore, Eq. 5-24 is a very good approximation to the numerical solution of this problem (Ref. 5-7).

5.2.3.3. Steady-state Release

Steady-state release is characterized by migration of gas atoms from the inside of the grain to the grain boundary. This phenomenon is represented by the classical model with an equivalent sphere of radius a, and uses:

- the diffusion equation inside the grain,
- the boundary condition given by Eq. 5-13, and
- the gas created equals the gas inside the grain plus the gas on grain boundary plus the gas released.

The diffusion equation is written:

$$\frac{\partial c}{\partial t} = \beta + div(D \cdot grad(c)) \qquad \text{Eq. 5-25}$$

where:

$c(r,t)$: local concentration (r being the space variable) in atoms of gas per unit volume,

β : creation rate, and

D : diffusion coefficient.

The work of Dowling, White and Tucker (Ref. 5-5) is followed in which the diffusion equation

is numerically solved by the finite difference method. The method allows for the re-solution effect at the grain boundaries. The grain is sub-divided into 2 zones, I and II, in which the creation rates are, respectively:

$$\beta_I = \beta \qquad \text{Eq. 5-26}$$

and:

$$\beta_{II} = \beta + bN/(4\delta) \qquad \text{Eq. 5-27}$$

The boundary condition is:

$$c(a, t) = 0 \qquad \text{Eq. 5-28}$$

The re-solution phenomenon is limited to the peripheral zone II with a thickness of 2δ that surrounds the internal zone I with a radius of $a - 2\delta$. In zone II, a re-solution flux contribution is added to the gas creation by the fission process. The constant b is the probability of re-solution of the intergranular bubbles.

A best-estimate analytical solution to the numerical solution is also proposed by Dowling, White and Tucker (Ref. 5-5). The solution starts from the incubation time and uses an approximation obtained from Ref. 5-8 of the diffusion equation with the following boundary conditions:

$$t = t_i: c(r, t_i) = c_i = constant \qquad \text{Eq. 5-29}$$

and:

$$c(a, t_i) = c_\delta \qquad \text{Eq. 5-30}$$

In terms of the steady state fractional fission gas release, this approximation is written:

$$F_{ss} = \left(1 - \frac{B_i}{B}\right) \cdot F_I(x) + \frac{c_i - c_\delta}{\beta t_i}\left(\frac{t_i}{t}\right) F_{II}(x) \qquad \text{Eq. 5-31}$$

where:

$$x = \frac{D(t - t_i)}{a^2} \qquad \text{Eq. 5-32}$$

$$c_{ss} = (1 - F_{ss}) \cdot \beta t \qquad \text{Eq. 5-33}$$

c_{ss} is the averaged steady-state concentration on the grain and c_i is the concentration at time t_i:

$$c_i = \beta t_i - \frac{3N_{sat}}{2a} \qquad \text{Eq. 5-34}$$

The functions F_I and F_{II} are the two solutions to the Booth equation (Ref. 5-6):

$$x<0.1 \qquad F_I = 4\cdot\sqrt{\frac{x}{\pi}} - \frac{3}{2}x \qquad \text{Eq. 5-35}$$

$$x>0.1 \qquad F_I = \left[1 - \frac{\frac{90}{\pi^4}\cdot exp(-\pi^2\cdot x)}{15x}\right] \qquad \text{Eq. 5-36}$$

$$x<0.1 \qquad F_{II} = 6\cdot\sqrt{\frac{x}{\pi}} - 3x \qquad \text{Eq. 5-37}$$

$$x>0.1 \qquad F_{II} = 1 - \frac{6}{\pi^2}\cdot exp(-\pi^2\cdot x) \qquad \text{Eq. 5-38}$$

The following important observation enables equation Eq. 5-31 to be simplified. The expression which contains the function F_{II} is generally negligible compared to the expression which contains the function F_I. Therefore, the expression of the fractional release value is given by expression Eq. 5-31, neglecting the term F_{II}.

Figures 5-3 and 5-4 show the variations in the steady state local fission gas release fraction (F_{ss}) with local burnup for various temperatures and with temperature for various local burnups, respectively.

F is the <u>total</u> fission gas release fraction (inside the grain <u>and</u> at the grain boundary). The evolution of the grain boundary gas is approximately given by Eq. 5-18. As a simplification, [b., e.]:

[b., e.] Eq. 5-39

where:

c_B^2 : grain boundary concentration at the beginning of burnup interval ΔB,

c_B^1 : grain boundary concentration at the end of burnup interval ΔB, and

N_{SAT} : fitted model parameter based on experimental observations of [b., e.] during a transient; N_{SAT} = [b. ,d.].

5.2.3.4. Transient Release

Transient is understood to mean a rapid increase in power with respect to time. The evolution of the concentration during the transient is [b., e.]. Diffusion is described by the solution of the diffusion equation when the [b., e.].

The equation has a best-estimate solution (Ref. 5-6):

$$\omega < 0.1 \qquad F_{TR} = 6\sqrt{\frac{\omega}{\pi}} - 3\omega \qquad \text{Eq. 5-40}$$

$$\omega > 0.1 \qquad F_{TR} = 1 - \frac{6}{\pi^2} \cdot exp(-\pi^2 \omega) \qquad \text{Eq. 5-41}$$

where:

$$\omega = \int_{t_0} \frac{D dt}{a^2} \qquad \text{Eq. 5-42}$$

and:

F_{TR} : fractional transient fission gas release due to diffusion.

[b., e.].

Eventually, during a transient, the total concentration takes the form:

[b., e.] Eq. 5-43

where:

c_0 : total concentration at time t_0,

c_{B0} : grain boundary concentration at time t_0, and

τ_R : fitted model parameter based on experimental observations of [b., e.] during a transient; τ_R = [b. ,d.].

5.2.3.5. Algorithm for Variable Conditions

The switchover from the steady state model to the transient state model is determined as follows:

Eq. 5-44

[b., e.]

Eq. 5-45

Figure 5-5 illustrates the variation in the total concentration of fission product gases (within and at grain boundary) versus burnup. The [b., e.] at values P_1, $P_2 > P_1$ and, again, at P_1 at the 3 burnup intervals $B < B_1$, $B_1 < B < B_2$ and $B > B_2$. The concentrations corresponding to these burnup intervals are c_1, c_2 and c_3. The curve c_2 is given by equation Eq. 5-43. From burnup B_2, the curve c_3 is given by the curve c_1 from the equivalent burnup B'_2 such that $c_1(B'_2) = c_3(B_2)$. Figure 5-5 also shows the evolution of the gas at grain boundary. For $B > B_2$, Eq. 5-39 is used.

In all the cases, the fractional thermal fission gas release is recalculated from [b., d.]:

[b., e.] Eq. 5-46

5.3. Adaptation to Mixed Fuels

5.3.1. MOX

The fission gas release phenomena occurring in UO_2 fuel are also present in MOX fuel. MOX fuel is heterogeneous, in contrast to UO_2 fuel. PuO_2 is present in the matrix mainly in the form of Pu-rich agglomerates and, to a lesser extent, as a solid solution. The burnup and fission product concentrations are therefore much higher in these heterogeneities than in the rest of the fuel matrix. The fission products can migrate to the outside of the heterogeneities in which they were created, afterwards diffusing and following the release laws of the surrounding fuel matrix. This

phenomenon, however, may lead to partial release of these fission products to the outside of the fuel by free paths. [e.].

[b., e.]

[b., e.] Eq. 5-47

where:

$C_6 < 1$: model parameter.

C_6 is adjusted on the MOX steady-state database:

C_6 = [b., d.].

The incubation curve for MOX is shown on Figure 5-2.

[e.].

5.3.2. UO_2-Gd_2O_3

The phenomena controlling the release of fission gas in UO_2-Gd_2O_3 fuel are the same as UO_2 fuel except for two differences. The temperature of the gadolinia fuel is higher because the thermal conductivity is less than that of UO_2. [b., e.]

[b., e.] Eq. 5-48

where:

T'_C : temperature [e.],

T_C : calculated local temperature,

P_{GD} = [b.], and

P_{GADO} : gadolinium weight fraction.

5.4. Experimental Database

5.4.1. Steady-state

The UO_2 steady-state model was calibrated with [b.] rods irradiated in PWRs (Table 5-1) or in test reactors and have been punctured and the fractional gas release was measured at end of irradiation. Likewise, the model was calibrated for [b.] MOX rods (Table 5-2) and [b.] gadolinia rods (Table 5-3).

The qualification range for UO_2 extends to a linear heat rate of [b.] kW/m and a rod average burnup of [b.] GWd/tM. The maximum fractional release (averaged over the rod) is [b.]. The open porosity varied from [b.].

The qualification range for MOX extends to a linear heat rate of [b.] kW/m and a rod average burnup of [b.] GWd/tM. The maximum fractional release value is [b.]. The open porosity varied from [b.].

The qualification range for gadolinia extends to a linear heat rate of [b.] kW/m and a rod average burnup of [b.] GWd/tM. The maximum value of the fractional release is [b.]. The open porosity varied from [b.].

The grain size varied from [b.], including all fuels.

5.4.2. Transient

The UO_2 transient model was calibrated with [b.] measurements from rods irradiated in experimental reactors. Less data was available for MOX fuel ([b.] measurements) and gadolinia fuel ([b.] measurements) (Table 5-4).

The range is as follows:

- linear heat rate during the transient up to [b., d.] kW/m (UO_2), [b., d.] kW/m (MOX), [b., d.] kW/m (Gd_2O_3),

- rod average burnup up to [b.] GWd/tM (UO_2), [b.] GWd/tM (MOX), [b.] GWd/tM (Gd_2O_3),

- transient duration between [b.] (UO_2), [b.] (MOX), [b.] (Gd_2O_3),

- ramp rate up to [b.] kW/m per min.

5.5. Qualification and Uncertainties

5.5.1. Best Estimate Models

5.5.1.1. Steady-state

The results for UO_2 fuel rods are presented in Figure 5-6 and Table 5-1. The mean value of the (M/P) ratios is equal to [b.] with a standard deviation (SD) equal to [b.].

The results for MOX fuel rods are presented in Figure 5-7 and Table 5-2. The mean value of the (M/P) ratios is [b.] with a SD equal to [b.].

The results for gadolinia fuel rods are presented in Figure 5-8 and Table 5-3. The mean value of the (M/P) ratios is [b.] with a SD equal to [b.].

Figures 5-9 and 5-10 show the dependence of the (M/P) ratios with burnup and measured fission gas release respectively for the three fuel types. There is no significant bias of the fit to the data.

5.5.1.2. Transient

The results are presented in Figure 5-11 and Table 5-4 for the three fuel types. For UO_2, the mean value of the (M/P) ratios is [b.] with a SD of [b.]. The number of samples is too small for the MOX and gadolinia samples for the means and SDs to be significant.

Figure 5-12 shows the comparison between the evolution of the predicted fission gas release and the measured fission gas release in the HATAC-C2 in-pile experiment (Ref. 5-9). In this experiment, a rodlet was re-fabricated from a rod irradiated for [b.] cycles in the French Fessenheim 2 PWR (average burnup of approximately [b.] GWd/tM) and re-irradiated in the French SILOE experimental reactor. The rodlet was irradiated over [b.] years with a base load of approximately [b.] kW/m and ramped [b.] times. The ramping powers ranged from [b.] kW/m and the hold times ranged from [b.]. There is [b.] between the predictions and measurements. In particular, one observes a [b.] during the first transient, which is well reproduced by the model predictions.

5.5.2. Upper-Bound Models

The Upper-Bound models are obtained by overpredicting a large number (approximately 95%) of the data points used to calibrate the Best-Estimate models:

[b., e.].

5.5.2.1. Steady-state

The comparisons between the UO_2 steady-state measured and calculated fission gas release with the Upper-Bound model are shown in Figure 5-13 which corresponds to Table 5-1. The bounding steady-state release model [b., e.].

The bounding model for UO_2 is used for the MOX and gadolinia rods. The M/P comparisons are given in Figure 5-14 and Table 5-2 for MOX rods and in Figure 5-15 and Table 5-3 for gadolinia rods. The bounding steady-state release model [b., e.].

5.5.2.2. Transient

Figure 5-16 and Table 5-4 show the M/P comparison. On a basis of [b., e.].

5.5.3. Validity Range

The validity range of this model corresponds to the code benchmarking ranges described in chapter 1.

This page intentionally left blank.

REFERENCES

Ref. 5-1 D. R. OLANDER, *Fundamental Aspects of Nuclear Reactor Fuel Elements*, TID-26711-P1 (1974).

Ref. 5-2 J.A. TURNBULL, C.A. FRISKNEY, J.R. FINDLAY, F.A. JOHNSON, A.J. WALTER, *The Diffusion Coefficients of Gaseous and Volatile Species During the Irradiation of Uranium Dioxide*, J. Nuclear Mater., 107 (1982) 168.

Ref. 5-3 J.A. TURNBULL, R.J. WHITE, C. WISE, *The Diffusion Coefficient for Fission Gas Atoms in Uranium Dioxide*, IAEA Tech. Com. Meeting on Water Reactor Fuel Element Computer Modelling in Steady State, Transient and Accident Conditions, Preston, (1988).

Ref. 5-4 M.V. SPEIGHT, *A Calculation of the Migration of Fission Gas in Material Precipitation and ReSolution of Gas Atoms under Irradiation*, Nucl. Sci. Eng., 31 (1969) 180.

Ref. 5-5 D.M. DOWLING, R.J. WHITE, M.O. TUCKER, *The Effect of Irradiation-Induced Re-Solution in Fission Gas Release*, J. Nuclear Mater., 110 (1982) 37.

Ref. 5-6 A.H. BOOTH, *A Method of Calculating Fission Gas Diffusion From UO_2 Fuel and its Application to the X-2-f Loop Test*, Rapport Atomic Energy of Canada Limited CRDC-721 (1957).

Ref. 5-7 L.C. BERNARD and E. BONNAUD, *Finite Volume Method for Fission Gas Release Modeling*, J. Nucl. Mat., 244 (1997) 75.

Ref. 5-8 J.A. TURNBULL, *The Effect of Grain Size on the Swelling and Gas Release Properties of UO_2 during Irradiation*, J. Nucl. Mat., 50 (1974) 62.

Ref. 5-9 E. PORROT, M. CHARLES, J.P. HAIRON, C. LEMAIGNAN, C. FORAT, F. MONTAGNON, *Fission Gas Release during Power Transients at high Burnup*, International Topical Meeting on LWR Fuel Performance, Avignon, France, April 1991.

This page intentionally left blank.

FIGURES

FIGURE 5-1 DIFFUSION COEFFICIENT [b.]

[b.]

FIGURE 5-2 THERMAL INCUBATION THRESHOLD

[b.]

FIGURE 5-3 LOCAL STEADY-STATE FRACTIONAL RELEASE VS. LOCAL BURNUP

[b.]

FIGURE 5-4 LOCAL STEADY-STATE FRACTIONAL RELEASE VS. LOCAL TEMPERATURE

[b.]

FIGURE 5-5 TRANSIENT ALGORITHM: LOCAL FISSION GAS RELEASE CONCENTRATION VS. LOCAL BURNUP

[b.]

FIGURE 5-6 BEST ESTIMATE PREDICTED VS. MEASURED STEADY-STATE FISSION GAS RELEASE FOR UO_2 FUEL

[b.]

FIGURE 5-7 BEST-ESTIMATE PREDICTED VS. MEASURED STEADY-STATE FISSION GAS RELEASE FOR MOX FUEL

[b.]

FIGURE 5-8 BEST-ESTIMATE PREDICTED VS. MEASURED STEADY-STATE FISSION GAS RELEASE FOR UO_2-Gd_2O_3 FUEL

[b.]

FIGURE 5-9 MEASURED-TO-PREDICTED FISSION GAS RELEASE VS. BURNUP

[b.]

FIGURE 5-10 MEASURED TO PREDICTED FISSION GAS RELEASE VS. MEASURED DATA

[b.]

FIGURE 5-11 BEST-ESTIMATE PREDICTED VS. MEASURED TRANSIENT FISSION GAS RELEASE FOR UO2, MOX, AND UO_2-Gd_2O_3 FUELS

[b.]

FIGURE 5-12 HATAC-C2 MULTIPLE TRANSIENT EXPERIMENT: COMPARISON BETWEEN MEASURED AND PREDICTED FISSION GAS RELEASE

[b.]

FIGURE 5-13 UPPER-BOUND PREDICTED VS. MEASURED STEADY-STATE FISSION GAS RELEASE FOR UO_2 FUEL

[b.]

FIGURE 5-14 UPPER-BOUND PREDICTED VS. MEASURED STEADY-STATE FISSION GAS RELEASE FOR MOX FUEL

[b.]

FIGURE 5-15 UPPER-BOUND PREDICTED VS. MEASURED STEADY-STATE FISSION GAS RELEASE FOR UO_2-Gd_2O_3 FUEL

[b.]

FIGURE 5-16 UPPER-BOUND PREDICTED VS. MEASURED TRANSIENT FISSION GAS RELEASE FOR UO_2, MOX, AND UO_2-Gd_2O_3 FUELS

[b.]

This page intentionally left blank.

TABLES

TABLE 5-1 COMPARISON BETWEEN STEADY-STATE MEASURED AND PREDICTED FISSION GAS RELEASES - UO_2

Fuel Rod Name	Program	Burnup (MWd/tM)	MEAS. FGR (%)	PRED. FGR (B.E.)	PRED. FGR (U.B.)	M/P (B.E.)	M/P (U.B.)

[b.]

Fuel Rod Name	Program	Burnup (MWd/tM)	MEAS. FGR (%)	PRED. FGR (B.E.)	PRED. FGR (U.B.)	M/P (B.E.)	M/P (U.B.)

[b.]

Fuel Rod Name	Program	Burnup (MWd/tM)	MEAS. FGR (%)	PRED. FGR (B.E.)	PRED. FGR (U.B.)	M/P (B.E.)	M/P (U.B.)

[b.]

Fuel Rod Name	Program	Burnup (MWd/tM)	MEAS. FGR (%)	PRED. FGR (B.E.)	PRED. FGR (U.B.)	M/P (B.E.)	M/P (U.B.)

[b.]

Fuel Rod Name	Program	Burnup (MWd/tM)	MEAS. FGR (%)	PRED. FGR (B.E.)	PRED. FGR (U.B.)	M/P (B.E.)	M/P (U.B.)

[b.]

Fuel Rod Name	Program	Burnup (MWd/tM)	MEAS. FGR (%)	PRED. FGR (B.E.)	PRED. FGR (U.B.)	M/P (B.E.)	M/P (U.B.)

[b.]

Fuel Rod Name	Program	Burnup (MWd/tM)	MEAS. FGR (%)	PRED. FGR (B.E.)	PRED. FGR (U.B.)	M/P (B.E.)	M/P (U.B.)

[b.]

Fuel Rod Name	Program	Burnup (MWd/tM)	MEAS. FGR (%)	PRED. FGR (B.E.)	PRED. FGR (U.B.)	M/P (B.E.)	M/P (U.B.)

[b.]

Fuel Rod Name	Program	Burnup (MWd/tM)	MEAS. FGR (%)	PRED. FGR (B.E.)	PRED. FGR (U.B.)	M/P (B.E.)	M/P (U.B.)
[b.]							

TABLE 5-2 COMPARISON BETWEEN STEADY-STATE MEASURED AND PREDICTED FISSION GAS RELEASES - MOX

Fuel Rod Name	Program	Burnup (MWd/tM)	MEAS. FGR (%)	PRED. FGR (B.E.)	PRED. FGR (U.B.)	M/P (B.E.)	M/P (U.B.)

[b.]

Fuel Rod Name	Program	Burnup (MWd/tM)	MEAS. FGR (%)	PRED. FGR (B.E.)	PRED. FGR (U.B.)	M/P (B.E.)	M/P (U.B.)

[b.]

Fuel Rod Name	Program	Burnup (MWd/tM)	MEAS. FGR (%)	PRED. FGR (B.E.)	PRED. FGR (U.B.)	M/P (B.E.)	M/P (U.B.)
[b.]							

TABLE 5-3 COMPARISON BETWEEN STEADY-STATE MEASURED AND PREDICTED FISSION GAS RELEASES - UO_2-Gd_2O_3

Fuel Rod Name	Program	Burnup (MWd/tM)	MEAS. FGR (%)	PRED. FGR (B.E.)	PRED. FGR (U.B.)	M/P (B.E.)	M/P (U.B.)
[b.]							

TABLE 5-4 COMPARISON BETWEEN MEASURED AND PREDICTED TRANSIENT FISSION GAS RELEASES FOR UO_2, MOX, AND UO_2-Gd_2O_3 FUEL

Fuel Rod	Program	Vendor	Oxide	Pmax (W/cm)	Computed Burnup (GWd/tM)	Holding Time	Peaking Factor at Pmax	Grain Size (µm)	Measured FGR (%)	BE Predicted FGR (%)	UB Predicted FGR (%)	M/P (BE)	M/P (UB)
[b.]													

Fuel Rod
Program
Vendor
Oxide
Pmax (W/cm)
Computed Burnup (GWd/tM)
Holding Time
Peaking Factor at Pmax
Grain Size (µm)
Measured FGR (%)
BE Predicted FGR (%)
UB Predicted FGR (%)
M/P (BE)
M/P (UB)

[b.]

Fuel Rod	Program	Vendor	Oxide	Pmax (W/cm)	Computed Burnup (GWd/tM)	Holding Time	Peaking Factor at Pmax	Grain Size (µm)	Measured FGR (%)	BE Predicted FGR (%)	UB Predicted FGR (%)	M/P (BE)	M/P (UB)
[b.]													

This page intentionally left blank.

6. PELLET STRAINS

6.1. Fractured Fuel Relocation

6.1.1. Phenomenon

Fuel pellets crack at BOL from thermal stresses as soon as the linear heat generation rate (LHGR) [b., e.]. The existence of a void volume in the rod, initially consisting of the fuel-cladding gap, allows a shifting of the various fuel fragments and therefore volume redistribution occurs between the outer gap and the cracks. This **initial fragment shift** phenomenon effectively increases the pellet radius.

After contact with the cladding, **rearrangement** occurs due to the effect of the stresses exerted by the interaction between the pellet and the cladding. Thus, the cladding outer diameter continues to decrease slowly due to creep even after pellet-cladding contact and then remains stable for a period of time. Finally, the pellet pushes out on the cladding increasing its diameter.

The mechanical equations of the COPERNIC code are solved assuming a solid pellet. The consequence is a slight underestimation of the pellet thermal expansion. This phenomenon is enhanced in transient conditions. To correct this effect of **cracked pellet thermal expansion** as compared to solid pellet, an additional term is added to fuel relocation strain.

6.1.2. Model

Total relocation strain is written as:

[b., e.] Eq. 6-1

where:

[b., e.]

The initial outwards shift model (ε_{shift}) reflects the pellet radius increase due to the shifting of the fragments:

[b., e .] Eq. 6-2

where:

[b., e .], and

[b., e .].

The post-contact model accounts for the rearrangement of the fuel fragments resulting from gap closure:

[b., e .] Eq. 6-3

[b., e.]

[b., e .] Eq. 6-4

6.1.3. Calibration Database

6.1.3.1. Initial Outwards Shift Model

This model was developed using cold gap measurements (optical method) on PWR rod ceramographies. Table 6-1 lists the cold gap measurements for 2 UO_2 PWR fuel rods irradiated for one cycle in the CRUAS 2 reactor on which ceramographies were performed. The measured cold values (minimum, maximum and average) are compared with the values predicted at the corresponding axial elevations. The agreement between measured and predicted values is good, taking into account the uncertainties associated with these measurements.

Examination of the profilometries of these 2 PWR rods irradiated in the CRUAS 2 reactor revealed incipient contact at the end of the first cycle. This is consistent with the code prediction and confirms the amount of the initial outwards shift of the fuel fragments as calculated by the COPERNIC relocation model.

6.1.3.2. Rearrangement Model

This model was developped using profilometries of 24 PWR fuel rods that were irradiated from [b., d., e.] in the GRAVELINES and BUGEY reactors. Figure 6-1 shows the measured and predicted clad diameter variations versus burnup for these fuel rods. The tendancy curves are also presented for both measured and predicted values. They correspond to the 3 following zones:

[b., d., e.]

The predicted cladding diameters shown in Figure 6-1 agree well with measurements when the experimental uncertainties are taken into account.

6.1.3.3. Cracked Pellet Thermal Expansion Model

The cracked pellet thermal expansion phenomenon is enhanced in transient conditions. Therefore, this model was developed using profilometries obtained before and after power ramp tests. Two ramp tests on the J12-2 rod (Ref. 6-2), that were conducted in the OSIRIS reactor, were choosen to calibrate this model because they were characterized by a very short hold time, that minimized gaseous swelling effects. Figures 6-2 and 6-3 show the measured and predicted cladding diameter variations versus axial elevation before and after ramping. Good agreement between measurements and predictions is shown in these figures.

6.1.4. Validation Database

The model for fractured fuel relocation has been globally qualified with a validation database that includes the:

- RECOR experiment (Ref. 6-3),
- profilometries measured on 1 to 5 cycle rods that operated in base load or load follow (Figures 7-3 to 7-19),
- profilometries of ramp tested fuel rods (Figures 7-41 to 7-44).

This is a global validation because it includes the mechanical interaction with the cladding. Thus, the measured to predicted comparisons are reported in chapter 7, except for the RECOR experiment.

The RECOR experiment (Ref. 6-3) consisted of performing in-pile diameter measurements on an initially fresh fuel rod while varying the LHGR. The as-fabricated pellet to clad gap of the test rod used in this program was reduced to be representative of a 2 cycle fuel rod. Figure 6-4 shows the measured and predicted fuel rod diameters at the mid-pellet location. The measured to predicted

agreement can be considered good, because the experimental conditions may not be perfectly representative of PWR conditions.

However, the agreement between the measured to predicted data obtained from the profilometries of the 1 to 5 cycle and ramp tested fuel rods is good.

6.1.5. Adaptation to Mixed Oxide Fuels

No specific adaptation is needed to correctly predict Gadolinia or MOX fuel behavior.

Table 6-2 lists one MOX rod irradiated for one cycle in the SAINT-LAURENT B1 reactor on which ceramographies were performed. The measured diametral cold gap values (minimum, maximum and average) are compared with values predicted at the corresponding axial elevations. The agreement is as good as for UO_2 fuel rods.

The measured to predicted profilometry comparison for the 1 cycle MOX rods (Figures 7-23 to 7-28) is good and validates the initial outwards shift model.

6.1.6. Validity Range

[e.]

6.2. Densification-Solid Swelling

6.2.1. Phenomenon

During irradiation, the fuel simultaneously undergoes two phenomena with opposite effects: densification and solid swelling.

* The in-pile densification is an irradiation-induced and thermally activated phenomenon: it consists of the elimination of fine porosity. Initially, small-sized pores (< 1 μm) are eliminated and those of intermediate size (on the order of 1 to 3 μm) are then gradually eliminated. It is assumed that the variation in larger-sized pores is negligible. As a result, the shape of the pellet pore size distribution will determine the densification behavior (Ref. 6-4).

The densification phase results in an increase in fuel density (or decrease in volume).

The UO_2 standard FRAGEMA product (powder produced by Integrated Dry Route, with the addition of a pore former during pelletizing) has the feature of being very stable with respect to the densification phenomenon (Ref. 6-5): the volume proportion of small-sized pores is very small, so densification is small. For this type of oxide, a variety of test results have shown that the density variation observed under irradiation was close to that obtained during a 24 h out of pile test at 1700°C, even if the mechanisms involved are different. This observation is the basis for the guidelines issued by the NRC (Ref. 6-6).

The use of other UO_2 powders may lead to different densification results:

[b.]

* The accumulation of fission products in the matrix during irradiation leads to "solid swelling". This phenomenon results in a decrease in density (or increase in volume). Studies have shown that solid swelling can be approximated as a [e.]. Note that a small fraction of matrix swelling can be accommodated by medium-sized pores and therefore solid swelling may differ depending on the type of oxide.

6.2.2. Models and Calibration Database for UO_2

Two different models, corresponding to two types of UO_2 powders [e.], were specifically developed for the FRAGEMA fuel product. FCF fuel is currently made with either the [e.] process. In view of their similar behaviors, [e.] are represented by the same [e.] model.

6.2.2.1. [e.] Model and Calibration Database

6.2.2.1.1. Hypotheses

This model combines two terms, one representative of in-pile densification based on the NRC recommendations (Ref. 6-6), and the other that describes the increase in volume due to solid swelling.

The model was based on the following hypotheses:

H1 - pure densification is a term varying logarithmically with burnup,

H2 - the maximum density (densification + swelling) is equal to the resintering test results,

H3 - the variation in volume by solid swelling [e.].

6.2.2.1.2. Equations

The expression that results from these hypotheses is:

[b., d.], Eq. 6-5

[b., d.], Eq. 6-6

where:

$\Delta\rho$: fuel density variation (% TD),

ρ_0 : initial density (% TD),

BU : local fuel burnup (MWd/tM),

α : fuel solid swelling rate (fission/cm^3)$^{-1}$,

k_0 : conversion constant:

$$k_0 = \beta \cdot \rho_{UO_2} \cdot \rho_0 \cdot \frac{m_U}{m_{UO_2}}, \qquad \text{Eq. 6-7}$$

β : fission transposition factor in MWd ($2.696.10^{21}$ for a fission energy of 200 MeV),

ρ_{UO2} : theoretical density of UO_2,

m_U : molar mass of uranium, and

m_{UO2} : molar mass of uranium oxide.

The boundary conditions enable [e.].

The solid swelling rate for UO_2 was determined from density measurements on [e.].

This model is illustrated in Figure 6-5.

6.2.2.2. [e.] Model and Calibration Database

6.2.2.2.1. Hypotheses

A separate model was developed for [e.] because the densification-swelling phenomenon for this powder is significant, particularly for heat transfer and rod internal gas pressure predictions. The FRAGEMA experience with this type of fuel is limited and consists [e.]. The model was taken from the literature (Ref. 6-8) and fitted to available FRAGEMA data.

6.2.2.2.2. Equations

The model is as follows:

$$\Delta\rho = \Delta\rho_{densification} + \Delta\rho_{solid-swelling} \qquad \text{Eq. 6-8}$$

where:

$$\Delta\rho_{densification} = \rho_0 \cdot a \cdot (1 - \exp(b \cdot BU)) \qquad \text{Eq. 6-9}$$

and:

$$\Delta\rho_{solid-swelling} = -\rho_0 \cdot k_0 \cdot \alpha \cdot BU \qquad \text{Eq. 6-10}$$

Eq. 6-11

[b., e.]

Eq. 6-12

6.2.3. Validation Database and Uncertainties

6.2.3.1. Validation Database

The UO_2 model [e.] was benchmarked with data obtained from a program directed by EPRI (Ref. 6-9), and a densification program conducted by FRAMATOME and the CEA: FRAMBOISE (Ref. 6-10 and Figure 6-7).

Figure 6-8 shows a measured and predicted comparison of the densities for the UO_2 database; each of the rods was evaluated with the densification and swelling model for the particular powder selected during manufacturing.

The predictive quality of the model can also be validated with cladding diameter (see Figure 6-1 in the strong pellet-clad contact zone) and fuel stack length predictions. Although less accurate than by direct comparison of measured and predicted fuel densities, this process provides a larger experimental database, because these variables are readily measured. Figure 6-9 thus shows the measured and predicted comparison of fuel stack length variations for the PWR UO_2 rods (Table 9-1).

6.2.3.2. Uncertainties

The solid swelling rate and associated uncertainties are:

[b., e.]

6.2.4. Adaptation to Mixed Oxide Fuels

6.2.4.1. MOX

Overall, the presence of plutonium leaves the UO_2 matrix practically unchanged relative to the densification phenomenon (Ref. 6-8). As a first approximation, plutonium-bearing fuel is assumed to follow the same densification model developed for the UO_2 fuel matrix. This assumption was verified with the results from an international program that was directed by EPRI in the 1970's (Ref. 6-11). [e.].

Figures 6-10 shows the measured and predicted comparison of the [e.] fuel densities. Figure 6-11 shows the measured and predicted comparison of fuel stack length variations for the PWR (U-Pu)O_2 experimental database (Table 9-2).

6.2.4.2. UO_2-Gd_2O_3

The fuel stack irradiation-induced elongation measurements, together with the density measurements taken from gadolinia rods irradiated in PWR reactors, or in test reactors, highlight a densification behavior [b.].

Densification is a phenomenon induced by irradiation and thermally activated: the lower number of fissions in the gadolinia fuel and the low temperatures reached throughout irradiation for depleted matrix rods, and during at least one cycle for enriched matrix rods, [b.].

On the basis of these experimental observations and in agreement with the literature on this topic (Ref. 6-12), [b.].

Figure 6-12 shows a measured and predicted comparison of fuel column length variations for (UO_2-Gd_2O_3) fuel rods (Table 9-3).

6.2.5. Validity Range

The validity range of the densification and solid swelling model corresponds to the code benchmarking ranges described in chapter 1.

6.3. Gaseous Swelling

6.3.1. Phenomenon

The gaseous swelling phenomenon is related to the production of gas atoms (primarily Xenon and Krypton) by the fission process. These atoms form inter- and intra-granular porosities which contribute to that portion of the fuel swelling referred to as «gaseous swelling». This phenomenon is complex and includes, among other factors, the generation, growth, coalescence and interconnection of bubbles and their impact on UO_2 creep and deformation. Gaseous swelling and fission gas release are closely linked. Therefore, some characteristics are common to both models. For example, gaseous swelling is subdivided into [e.].

Gaseous swelling test results are still relatively scarce. Therefore, a semi-empirical expression that includes the main experimental observations has been applied. There is no gaseous swelling below a temperature close to the threshold temperature for thermal fission gas release. Above this threshold, gaseous swelling increases with temperature due to the bubble kinetics. This effect is mitigated by fuel redensification at high temperatures. As a net effect, [e.].

6.3.2. Model

6.3.2.1. Steady-state Gaseous Swelling Model

The fraction of the fuel volume due to gaseous swelling, POR_G, is given by

Eq. 6-13

[b., e.] Eq. 6-14

Eq. 6-15

f_1 : [b.],

f_2 : [b.],

T : local temperature (°C),

T_i : [b., e.],

BU : local burnup (MWd/tM),

[b., d.],

[b., d.], and

[b., d.].

This set of parameters implies that the fuel [b.]. Figure 6-13 schematically shows the gaseous porosity variation with temperature according to the previous expression. [b.].

6.3.2.2. Transient Gaseous Swelling Model

Recent experimental measurements Ref. 6-13 show that transient gaseous swelling kinetics are qualitatively similar to transient gas release kinetics and quantitatively faster. Thus, during a transient, POR_G is defined by:

Eq. 6-16

[b., e.] Eq. 6-17

where:

[b.]

6.3.3. Calibration Database

6.3.3.1. Steady-state Gaseous State Swelling

The model qualification was primarily based on detailed observations and measurements of gaseous porosity that were performed for the NFIR program (Ref. 6-14 and Ref. 6-15). Six rods were irradiated in the BR3 reactor at Mol in Belgium. The irradiation characteristics are given in Table 6-3. Five rods (A1 to A5) were constructed by Belgonucléaire [e.] and the sixth rod (B1) was constructed by FRAGEMA [e.]. Measurements were performed on samples taken at several heights along these fuel rods: in the middle (A11, A21, A31, A41, A51 and B11), between the end and middle (A22, A32, A42, A52) or at the end (A23, A33, B13). Rods type A and B also differed in gas release as indicated in Table 6-3: the release was large for rods A and small for rod B.

Figure 6-14 shows a typical porosity measurement [b.]. Four zones can be defined from the outside to the center of the pellet:

- zone I [e.],
- zone II [e.],
- zone III [e.], and
- zone IV [e.].

Samples from rod B do not exhibit a zone IV region, in agreement with their low fission gas release which is probably below the thermal release threshold. Zone III is, therefore, a transition zone where [e.].

The average gaseous porosity measurement for the pellet is the difference between the average total porosity and the porosity of the densified fuel evaluated as the average of the porosity in zone II. Whereas the rod B samples are not considered to exhibit gaseous swelling, samples from rod A exhibit a maximum porosity that ranges from [b.] for peak power burnups that range from [e.].

Figure 6-15 and Table 6-3 show the measured and predicted values of gaseous swelling. The mean value of the measured to predicted differences is [b.] and the standard deviation of these differences is [b.].

Figure 6-16 shows the measured and predicted radial porosity profiles of [b.].

6.3.3.2. Transient Gaseous Swelling

The transient gaseous swelling model was benchmarked with GONCOR experimental data (Ref. 6-16) and data from 6 rodlets ramped at STUDSVIK (Ref. 6-17). The hold times of the STUDSVIK rodlets ranged from [e.] at a peak power slightly above [e.] (see Table 6-4). These rodlets were fabricated from rods that were irradiated from [e.] in PWR reactors. The STUDSVIK data consisted of profilometry measurements performed after the ramp. The GONCOR experiment, however, was specially designed to measure clad strains during the ramp. In this experiment, a rodlet was fabricated from a rod that was irradiated in a PWR reactor for [e.]. This rodlet was irradiated for [e.] at approximately [e.].

The measured and predicted diameter variations (diameter during the test minus diameter before the test) of the GONCOR irradiation are shown in Figure 6-17. The diameters were measured at mid-pellet locations because pellet ends are affected by dish-filling during ramping. This 3D effect is not modeled here. Note that the pre-ramp conditions are included in this figure.

Figure 6-17 shows that the GONCOR measured and predicted diameter variations agree remarkably well except towards the end of the ramp. The diameter then decreases due to redensification. The redensification kinetics have not been modeled at this time.

The measured and predicted diameter variations (diameter after the test minus diameter before the test) for the STUDSVIK tests are shown in Figures 6-18 and 6-19. The model predictions [b.] with data for the burnups, powers and hold times presented.

6.3.4. Validation Database

The gaseous swelling model is globally validated with the experimental database used to validate the COPERNIC code.

6.3.5. Adaptation to Mixed Fuels

The UO_2 gaseous swelling model is also applied to MOX and gadolinia fuels.

6.3.6. Validity Range

[b.]

REFERENCES

Ref. 6-1 L.A. WALTON, J.E. MATHESON, *Fumac - A new model for light water reactor fuel relocation and pellet-cladding interaction*, Nuclear Technology, Vol. 64, pp 127-138, February 1984.

Ref. 6-2 P. COUFFIN, *Compte rendu d'irradiation crayon J12-2, Cycle F144*, CEA Report, C.Ri 98-0036, Avril 1998.

Ref. 6-3 L. CAILLOT, G. DELETTE, B. JULIEN, J.C. COUTY, *Impact of fuel pellet fragmentation on pellet-cladding interaction in a PWR fuel rod: results of the RECOR experimental programme*, 14th International Conference on Structural Mechanics in Reactor Technology, SMiRT 14, Lyon, France, August 17-22, 1997.

Ref. 6-4 H. ASSMAN, H. STEHLE, *Thermal and In-Reactor Densification of UO_2: Mechanisms and Experimental Results*, Nuclear Engineering and Design 48 (1978), p 49-67.

Ref. 6-5 A. CHOTARD, A. LEDAC, M. BERNARDIN, *Fabrication, Characteristics and In-Pile Performance of Pellets Prepared from Dry Route Powder*, International Symposium on Advanced Ceramics, Bombay (India), November 26-30 1990.

Ref. 6-6 *Regulatory Guide 1*, 126, Revision 1, March 1978.

Ref. 6-7 G. MAIER, H. ASSMANN, W. DORR, *Resinter Testing in Relation to In-Pile Densification*, Journal of Nuclear Materials, 153, p. 213-220, 1988.

Ref. 6-8 F.U. SCHLEMMER, H.P. FUCHS, R. MANZEL, *Status of Irradiation Experience with Recycled Fuel Materials in the FGR for Siemens/KWU Type Fuel Assemblies*, IAEA - Technical Committee Meeting on Recycling of Plutonium and Uranium in Water Reactor Fuels. Cadarache (France), November 13-16 1989.

Ref. 6-9 D.W. BRITE and al., *EEI/EPRI - Fuel Densification Program*, Final Report, EPRI 13, June 1975.

Ref. 6-10 J. JOUAN, *Fabrication of Water Reactor Fuel Elements*, IAEA - Specialist's meeting - Vienna 1979.

Ref. 6-11 M.D. FRESHLEY, D.W. BRITE, J.L. DANIEL, P.E. HART, R.K. MARSHALL, *Plutonia Fuel Study - Project 356 - Final Report*, EPRI NP-637, January 1978.

Ref. 6-12 R. MANZEL, W.O. DOERR, *Manufacturing and Irradiation Experience with UO_2/ Gd_2O_3 Fuel*, American Ceramic Society Bulletin, Vol. 59 (1980).

Ref. 6-13 I. ZACHARIE et al., *Thermal treatment of uranium oxide irradiated in pressurized water reactor: swelling and release of fission gases*, Journal of Nuclear Materials 255, pp 85-91 (1998).

Ref. 6-14 P. BLANPAIN, M. LIPPENS, D. HAAS, *Properties of UO_2 irradiated to high burnups*, Project X101-5, Final Report EPRI NP-5191-LD (1987).

Ref. 6-15 P. BLANPAIN, M. LIPPENS, D. HAAS, C. BAKER, J.A. TURNBULL, *Properties of UO_2 irradiated to high burnups*, Projects X101-5, -7, EPRI Report NP-5189-LD (1987).

Ref. 6-16 L. CAILLOT, *GONCOR : étude de la contribution du gonflement gazeux à la déformation d'un crayon en transitoire. Synthèse finale.*, CEA Report CR DTP/ SECC 96/102A (1996).

Ref. 6-17 K. MALEN, *Ramp test on a FRAGEMA PWR fuel fabricated by the Fabrice process. Non destructive examinations*, STUDSVIK Report N(H) - 94/58, 1994; *Post-ramp examinations of rodlets A04/2, A04/3 and A15/3*, STUDSVIK Report N(H) - 95/07, 1995; *Post-ramp non destructive examinations of rodlets A10/5 and A09/5*, STUDSVIK Report N(H) - 95/54, 1995.

Ref. 6-18 E. PORROT, F. LEFEBVRE, M. CHARLES, C. LEMAIGNAN, *Mechanisms of cladding deformation and fission gas release during power transients at high burnup*, ANS Topical Meeting on LWR Fuel performance, Williamsburg, 1988.

FIGURES

FIGURE6-1 TIME EVOLUTION OF THE CLADDING DIAMETER OF PWR RODS

[b.]

FIGURE 6-2 MEASURED AND PREDICTED CLADDING DIAMETERS VARIATIONS (J12-2 FIRST RAMP)

[b.]

FIGURE 6-3 MEASURED AND PREDICTED CLADDING DIAMETERS VARIATIONS (J12-2 SECOND RAMP)

[b.]

FIGURE 6-4 MEASURED AND PREDICTED CLADDING DIAMETERS (RECOR EXPERIMENT)

[b.]

FIGURE 6-5 [e.] FUEL DENSIFICATION MODEL

[b.]

FIGURE 6-6 [c.] FUEL DENSIFICATION MODEL

[b.]

FIGURE 6-7 MEASURED AND PREDICTED DENSITY INCREASE (FRAMBOISE PROGRAM)

[b.]

FIGURE 6-8 MEASURED AND PREDICTED DENSITY (UO_2)

[b.]

FIGURE 6-9 MEASURED AND PREDICTED FUEL COLUMN GROWTH (UO_2)

[b.]

FIGURE 6-10 MEASURED AND PREDICTED DENSITY (MOX)

[b.]

FIGURE 6-11 MEASURED AND PREDICTED FUEL COLUMN GROWTH (MOX)

[b.]

FIGURE 6-12 MEASURED AND PREDICTED FUEL COLUMN GROWTH (UO_2-Gd_2O_3)

[b.]

FIGURE 6-13 GASEOUS SWELLING MODEL

[b.]

FIGURE 6-14 MEASURED POROSITY RADIAL DISTRIBUTION

[b.]

[b.]

FIGURE 6-15 MEASURED AND PREDICTED GASEOUS SWELLING

[b.]

FIGURE 6-16 MEASURED AND PREDICTED RADIAL POROSITY PROFILE FOR [b.]

[b.]

FIGURE 6-17 MEASURED AND PREDICTED CLADDING DIAMETER VARIATIONS (GONCOR EXPERIMENT)

[b.]

FIGURE 6-18 MEASURED AND PREDICTED CLADDING DIAMETER VARIATIONS (AO4_3, AO9_5, IO8_5 RAMPS)

[b.]

FIGURE 6-19 MEASURED AND PREDICTED CLADDING DIAMETER VARIATIONS (M13_5, G11_5, I14_5 RAMPS)

[b.]

TABLES

TABLE 6-1 MEASURED AND PREDICTED COLD GAP (UO_2)

Reactor	Fuel Rod	Nb. of Cycles	Local Burnup (MWd/tU)	Axial Elevation (mm)	Min. Measured (µm)	Max. Measured (µm)	Avg. Measured (µm)	Predicted Cold Gap (µm)
[b.]								

TABLE 6-2 MEASURED AND PREDICTED COLD GAP (MOX)

Reactor	Fuel Rod Nbr.	Nb. of Cycles	Rod Burnup (MWd/tM)	Axial Elevation (mm)	Min. Measured (µm)	Max. Measured (µm)	Avg. Measured (µm)	Predicted (µm)
[b.]								

TABLE 6-3 MEASURED AND PREDICTED GASEOUS SWELLING MODEL

Fuel Rod Nbr.	Sample	Pmax kW/m	EOL Burnup GWd/tU	Pmax Burnup GWd/tU	Fuel Rod FGR %	Max. Porosity %	Avg. Porosity after Densification % (a)	Measured Avg. Gas Porosity (b)	Predicted Avg. Gas Porosity
[b.]									

[b.]

TABLE 6-4 CHARACTERISTICS OF STUDSVIK RAMP TESTS

Name of Ramps	Number of Cycles	Burnup (MWd/tM)	Peak Power (kW/m)	Hold Time (hours)
[b.]				

This page intentionally left blank.

7. CLADDING STRAINS

7.1. Irradiation Creep

7.1.1. Phenomenon

The creep of a material subjected to stresses is a time-dependent plastic strain phenomenon that can be considered as flow activated either thermally or by irradiation, or both simultaneously.

For a given material (same chemical composition, microstructure, manufacturing process), strain can be expressed as a function of:

- σ : stress,
- T : temperature,
- t : time, and
- ϕ : fast neutron flux.

7.1.2. Stress-Relieved Zircaloy-4 Model

7.1.2.1. Model

A creep model (FRA 97) for FRAGEMA Zircaloy-4 stress-relieved (standard and AFA 2G process) cladding has been developed. The primary and secondary creep states are distinguished in the model. The external circumferential strain ε (fractional) is given by:

[b.] Eq. 7-1

where:

- $\sigma = \sigma_{\theta\theta} - \sigma_{rr}$,
- $\sigma_{\theta\theta}$: clad hoop stress (MPa),
- σ_{rr} : clad radial stress (MPa),
- t : time (h),
- T_K : clad temperature (K),
- ϕ : fast neutron flux (E>1 MeV) in 10^{14} n/cm^2/s,
- A_1 = [b., d.],
- A_2 = [b., d.],
- A_3 = [b., d.],
- A_4 = [b., d.],

B_1 = [b., d.],

B_2 = [b., d.],

B_3 = [b., d.],

B_4 = [b., d.], and

B_5 = [b., d.].

Based on the analysis of a long duration test [b.], FRA 97 includes the effects of irradiation hardening: a decrease of the secondary creep rate with increasing irradiation (Figure 7-1).

This model represents the outer diameter variation and must be corrected so that it can be applied locally at each radial node in the cladding. The following relationship is applied, [e.]:

[b.] Eq. 7-2

where:

[b.]

The computational process used to determine the cumulative creep strain during a time step is incremental, [b., e.]:

[b.] Eq. 7-3

[b.] Eq. 7-4

[b.]

[b., d.]

7.1.2.2. Calibration Database

7.1.2.2.1. Irradiated Tubes

The irradiation campaigns ZS07 / ZS14 / ZS15 / ZS16 / ZS17 conducted by the CEA on stress-relieved Zircaloy-4 clad sections in the SILOE test reactor enabled the irradiation creep relationships to be determined under the following conditions:

- temperature : [b., d.]
- fast neutron flux (E>1 MeV) : [b., d.]
- hoop stress : [b., d.]
- irradiation time : [b., d.]
- fast neutron fluence : [b., d.]

The tests were run with helium or argon pre-pressurized sealed specimens in a NaK medium that provided freedom from the corrosion phenomenon.

The tubes used in the tests were selected from a Zircotube-manufactured lot (AFA 2G process) exhibiting average thermal creep [b., d.] relative to the standard test [b., d.].

Table 7-1 summarizes the test matrix.

The fast flux levels were determined with copper detectors that were placed at the tube mid-height location. These levels ranged from [b., d.].

Three temperature levels [b., d.] with an accuracy of +/- 2°C, and several stress levels [b., d.] were chosen to test the dependence of in-pile deformation on these two parameters.

7.1.2.2.2. Rods Irradiated in PWR Reactors

The creep model database also includes results obtained from FRAGEMA fuel rods irradiated in power reactors.

The following criteria for these fuel rods were verified:

- no pellet-cladding contact and the absence of ridges on the cladding. These criteria ensured free creep of the cladding under external pressure effects. This typically limited the rods to one cycle of irradiation.

- external cladding corrosion was characterized by measuring the oxide thickness after irradiation in order to account for corrosion in the outer diameter variations.

Finally, four well characterized UO_2 rods of the FRAGEMA database were taken into account (Table 7-1). These rods were irradiated for one cycle in either the CRUAS 2 or GRAVELINES 5 EDF nuclear reactors. Their claddings were manufactured by Zircotube with a stress-relieved (standard and AFA 2G process) Zircaloy-4.

The operating conditions for each of these rods (FRAGEMA power histories) are available, as well as the results of the initial characterizations and the PIEs that gave:

- the outer diameters, and

- the oxide thicknesses.

7.1.2.3. Validation Database and Uncertainties

7.1.2.3.1. Irradiated Tubes

Figure 7-2 shows a measured to predicted comparison of cladding diametral reductions based upon [b.] tube sample irradiation tests.

7.1.2.3.2. Rods Irradiated in PWRs and Test Reactors

The model predictive quality was evaluated by comparing the measured cladding outer diameter variations (without corrosion) with those predicted by the COPERNIC code. Generally, the diameter measurements were profilometry measurements that were taken axially along two lines 90 degrees apart. Helical diameter measurements were also taken for some rods (CRUAS).

Figures 7-3 to 7-10 illustrate the creep model predictive quality for [e.] with FRAGEMA Zircaloy-4 stress-relieved cladding (standard and AFA 2G process) irradiated in PWRs or a test reactor (CAP). The diametral reductions predicted by COPERNIC are compared with the corrected mean measured values. These rods are identified in Table 7-2.

The PIE on these rods demonstrated the absence of pellet-cladding contact at the end of irradiation. The cladding of these rods, therefore, operated in a free creep environment without interference from pellet-induced effects.

Figures 7-11 to 7-19 show the measured versus predicted outer diameter variation for [e.] with the FRAGEMA Zircaloy-4 stress-relieved cladding that were irradiated for [e.] in a PWR. The values obtained after pellet-clad contact enable the COPERNIC pellet strain models, including the relocation model, to be verified.

Figure 7-20 shows the creep model predictions for the rods with FRAGEMA Zircaloy-4 stress-relieved cladding (standard and AFA 2G process) irradiated [e.] in a PWR or in a test reactor (CAP). The COPERNIC predicted diametral reductions are compared with measured data in this figure.

Figure 7-21 presents a measured to predicted comparison of [e.] in PWRs or in a test reactor (CAP) with FRAGEMA Zircaloy-4 stress-relieved cladding (standard and AFA 2G process).

7.1.2.3.3. Uncertainties

The related uncertainty range for overpredicting or underpredicting 95% of the measured data points (Figure 7-22) is defined by the following bounds:

[e.]

All of the PWR rods referenced in Table 7-2 were retained with the exception of the [b., d.] rod *which was not characterized before irradiation and was located close to gadolinia rods.*

7.1.2.4. Adaptation to Mixed Fuels

The results acquired for mixed oxide rods showed that the cladding dimensional variations are [e.]. This model therefore is applied to MOX fuel rods by using a [b.]. Figures 7-23 to 7-28 present the creep model predictions for 6 rods with FRAGEMA Zircaloy-4 stress-relieved cladding [b., d.] irradiated for [e.] in a PWR. Three types of fuel are used: [e.]. The creep values predicted with COPERNIC are compared with diametral mean measured values (corrosion absent). These rods are identified in Table 7-3.

Figure 7-29 shows the creep model predictions for [b., d.] rods with FRAGEMA Zircaloy-4 stress-relieved cladding [b., d.] in a PWR. The diametral reductions predicted with COPERNIC that are compared with measured diametral reductions show similar agreement to the results obtained for the UO_2 rods.

7.1.2.5. Validity Range of the FRA 97 Model

This model was benchmarked under the following conditions:

- stress-relieved Zircaloy-4 cladding,
- UO_2, UO_2-Gd_2O_3, and MOX fuel rods [e.],
- temperature range: [b., d.]. (The creep tests on tube samples ranged from [b., d.]. The average clad temperature of the PWR fuel rods investigated varied from [b., d.]. The analysis of test data with a temperature as low as [b., d.] did not show any significant drift, so the temperature

band was extended to [b., d.]),

- stress range: [b., d.], corresponding to the average hoop stresses obtained under normal operating conditions. [b., d.],

- fast flux range [b., d.]. (The calibration database used to adjust the creep model ranged from [b., d.]. The analysis of test data with fast neutron flux as low as [b., d.] did not show any significant drift, therefore the fast flux band was extended to[b., d.]).

7.1.3. Alloy 5 Cladding Model

7.1.3.1. Model

The (M5_98) creep model for alloy 5 cladding is based upon the hypothesis that the external circumferential strain ε is a function of the thermal creep ε_{th} and the irradiation creep ε_{irr} (Ref. 7-1).

This model can be expressed as follows:

Eq. 7-5

[b.] Eq. 7-6

Eq. 7-7

and where:

$\dot{\varepsilon}$: total diametral creep rate (%/s),

$\dot{\varepsilon}_{th}$: thermal creep rate (%/s),

$\dot{\varepsilon}_{irr}$: irradiation creep rate (%/s),

B_1 = [b., d.],

B_2 = [b., d.],

B_3 = [b., d.],

a_D = [b., d.],

c_D = [b., d.],

Φ : [b., d.],

t : [b., d.],

a_{irr} : [b., d.],

n_j = [b., d.],

p_i = [b., d.],

Q_i = [b., d.],

σ = $\sigma_{\theta\theta} - \sigma_{rr}$,

$\sigma_{\theta\theta}$: clad hoop stress (MPa),

σ_{rr} : clad radial stress (MPa),

ϕ : fast neutron flux E > 1 MeV ($n/m^2/s$), and

T : mean fiber temperature (K).

- The thermal creep component ε_{th} was determined with a Soderberg type of pre-irradiation thermal creep relationship, consisting of two terms:

* a primary term $\varepsilon_{th\ P}$ not affected by irradiation that is limited to BOL calculations, and

* a secondary term $\varepsilon_{th\ SD}$ affected by irradiation-induced hardening.

Given the loadings typically sustained by rods during operation, the thermal creep contribution is small compared with the total strain.

- The irradiation creep component ε_{irr} was determined by substracting the thermal creep component ε_{th} from the total strain; ε_{irr} is modelled in accordance with the classical Norton type of relationship. The irradiation creep model thus obtained is characterized by:

* [b., d.],

* [b., d.], and

* [b., d.].

Irradiation creep is a major contributor to the total diametral strain of the fuel rod cladding.

This model represents the outer diameter variation and must be corrected so that it can be applied locally at each radial node in the cladding. The following relationship is applied, based upon the conservation of volume for plastic strain:

[b., d.] Eq. 7-8

[b., d.]

Eq. 7-9

Eq. 7-10

7.1.3.2. Calibration Database

The low-stress diametral creep model for alloy 5 cladding was derived from experience feedback gained from creep tests on irradiated and non-irradiated cladding tubes and on PWR rod diameter measurements obtained in the hot cell or on site.

7.1.3.2.1. Thermal Creep Calibration Database

The tests performed by CEA-SRMA on non-irradiated alloy 5 tubes enabled the primary thermal creep term $\varepsilon_{th\ P}$ and the secondary thermal creep term $\varepsilon_{th\ SD}$ to be determined under the following conditions:

- temperature : [b., d.],
- hoop stress : [b., d.],
- irradiation time : [b., d.].

Table 7-4 summarizes the test matrix.

The tubes used in the tests came from Zircotube-manufactured lots with an average thermal creep of ε_{th}=[b., d.] relative to the standard test [b., d.]. The standard thermal creep tests [b., d.] performed on sections of irradiated and non-irradiated tubes enabled the hardening parameters a_D and c_D of the secondary thermal creep term $\varepsilon_{th\ SD}$ to be determined.

The irradiated tubes used to define the irradiation induced hardening parameters are listed in Table 7-5. The high fluence secondary thermal creep rate is independent of the alloy. Therefore, this test matrix includes recrystallized (RXA) and stress-relieved (SRA) Zircaloy-4 cladding tubes that were irradiated for [b.] cycles in PWR reactors.

7.1.3.2.2. Irradiation Creep Calibration Database

The alloy 5 irradiation creep model database includes data that was obtained from irradiated FRAGEMA fuel rods. These rods were used to calibrate the irradiation creep component ε_{irr} obtained by substracting the thermal creep component from the total diametral creep strain ε.

The following criteria were verified for these fuel rods:

- no pellet-cladding contact and absence of ridges (< 10 µm). This ensured free creep of the cladding due to external pressure effects and typically limited the rods to [b.] of irradiation.

- external cladding corrosion was characterized by measuring the oxide thickness after irradiation in order to account for corrosion in the outer diameter variations.

[b.] alloy 5 rods were included in the FRAGEMA database (Table 7-6). [b.] of these rods were irradiated for [b.] in the GRAVELINES 5 reactor, and the other [b.] rods were irradiated for [b.] in the CATTENOM 2 reactor. The profilometries of rods irradiated in GRAVELINES 5 were measured in a hot cell, while the profilometries of rods irradiated in CATTENOM 2 were measured on-site. The power histories for each of these rods are available, together with the results of the post-irradiation examinations.

Overall, the PWR database includes:

- [b., d.],

- [b., d.],

- [b., d.], and

- [b., d.].

7.1.3.3. Validation Database and Uncertainties

The model predictive quality was evaluated by comparing the measured cladding outer diameter variations (without corrosion) with those predicted by the COPERNIC code.

Figures 7-30 to 7-35 provide a comparison of the profilometries that were measured in the hot cell or on-site to the predicted profilometries from the [b.] alloy 5 rods irradiated in GRAVELINES 5 or CATTENOM 2. The values measured on-site are less accurate than the values measured in the hot cell. There is a [b.] measured to predicted agreement.

Note that:

- the creep strain at the rod ends is [b.], which implies a [b.] for the fast neutron flux effects,

- the test profilometries show a slight diameter decrease with rod elevation. This trend is [b.] due to the low activation energy of the irradiated creep model.

Figures 7-36 and 7-37 contain the measured and predicted outer diameters for [b.] other alloy 5

rods that were irradiated for [b.] cycles in the GRAVELINES 5 reactor. The shape of the curves shown in the figures indicates that pellet-cladding contact is established. The [b.] agreement between the predicted and measured outer diameters also supports the pellet strain models, and in particular the relocation model.

The related uncertainty range for overpredicting or underpredicting 95% of the measured data points is defined by the following bounds:

[e.]

Figure 7-38 presents the measured to predicted comparison of the alloy 5 rods irradiated for [b.] in PWR reactors, with the upper and lower bounds. All of the PWR rod data referenced in Table 7-6 were retained in this comparison.

7.1.3.4. Validity Range

The validity range of the alloy 5 cladding model is as follows:

- UO_2, UO_2-Gd_2O_3 and MOX rods [e.],
- temperature range : [b., d.],
- hoop stress range : [b., d.],
- fast flux (E > 1 MeV) : [b., d.].

7.2. High Stress Creep and Relaxation

7.2.1. Phenomenon

Cladding strain during strong mechanical interaction with the pellet is a combination of elastic-plastic strain and creep strain, inducing stress relaxation. The share of each strain (plasticity and creep) depends on the loading encountered.

Stress relaxation is controlled by the cladding short-term creep properties. The rod creep is [e.] for high stress levels.

[e.] for a given material is a function of:

- time,
- stress,
- temperature, and
- fluence.

7.2.2. Stress-Relieved Zircaloy-4 Model

7.2.2.1. Model

The high-stress creep model for stress-relieved Zircaloy-4 cladding is [e.].

The high-stress creep relationship for the stress-relieved Zircaloy-4 model is the following:

[b.] Eq. 7-11

where:

ε	:	creep strain (fractional),
σ	:	stress (MPa); $\sigma = \sigma_{\theta\theta} - \sigma_{rr}$,
$\sigma_{\theta\theta}$	:	cladding hoop stress (MPa),
σ_{rr}	:	cladding radial stress (MPa),
T_K	:	temperature (K),
t	:	time (h),
Φ	:	fluence (10^{21} n/cm^2),
B_0	=	[b., d.],
B_1	=	[b., d.],
B_2	=	[b., d.],
B_3	=	[b., d.],
B_4	=	[b., d.],
B_5	=	[b., d.], and
B_6	=	[b., d.].

This relationship was benchmarked within the following ranges:

[b., d.] < σ < [b., d.]
[b., d.] < T < [b., d.]
[b., d.] <Φ < [b., d.]

This relationship was incorporated into the COPERNIC code with an incremental computation process of [b.]:

[b.] Eq. 7-12

[b.] Eq. 7-13

The strain at time t_1 is calculated from the strain at time t_0 with the following relationship:

[b.] Eq. 7-14

where [b.].

Before the power transient, the cladding creep is simulated with the base-load creep model (FRA 97). Changeover from one relationship to the other is as follows:

Eq. 7-15

[b.]

Eq. 7-16

Eq. 7-17

7.2.2.2. Calibration Database

Creep and relaxation tests were performed with non-irradiated specimens and samples obtained from sections of fuel rods that were irradiated in PWR reactors. The stress was calculated during data acquisition with [e.].

7.2.2.2.1. *Non-Irradiated Material*

Creep and relaxation tests were performed on stress-relieved low tin Zircaloy-4 cladding at [b., d.]:

- primary creep data were obtained at an average stress ranging from [b., d.],
- relaxation data were obtained from [b., d.].

7.2.2.2.2. Irradiated Material

High-stress primary creep tests were performed with material that was obtained from rods

7.2.2.2.2. Irradiated Material

High-stress primary creep tests were performed with material that was obtained from rods irradiated in the GRAVELINES 5 reactor for [b.] attaining an average fluence of [b., d.] under the following conditions:

- [b., d.] with stresses varying from [b., d.].

Tests were also performed on standard [e.] rods that were irradiated in the GRAVELINES reactors under the following conditions:

- [b., d.], and

- [b., d.].

These tubes attained an average fluence of [b.].

7.2.2.3. Validation Database and Uncertainties

7.2.2.3.1. Relaxation Tests

Relaxation tests performed at [b.] on non-irradiated tubes were simulated with COPERNIC. The measured and predicted stresses obtained at [b.] shown in Figure 7-39 agree [b.].

The maximum recorded deviation between the measured and predicted stresses was [b.].

7.2.2.3.2. High-stress Creep Tests

Figure 7-40 shows a measured to predicted comparison of the [b.] experimental data points that comprise the test base for irradiated tubes.

7.2.2.3.3. Power Ramps on PWR Fuel Rods

Permanent cladding strain was measured by comparing fuel rod profilometries before and after a ramp test to reflect the creep/relaxation phenomenon present at high power.

Power ramps performed on PWR fuel rods can be used to validate the high stress clad creep model by comparing the measured and predicted clad strains before and after ramps. This, however, is a global validation of several models including pellet strain phenomena such as gaseous swelling, creep, crack healing, etc.

Ramp tests were conducted in the OSIRIS or STUDSVIK R2 reactors with rodlets refabricated from PWR fuel rods. Most of these rods had been irradiated for [e.]. These ramps were primarily characterized by a ramping rate and hold time. The pellet time dependent phenomena were minimized with fast ramp rates and short hold times.

Figures 7-41 to 7-43 show the measured and predicted strains versus axial elevation before and after ramping for three of these ramps performed in the OSIRIS reactor: two 2 cycle rods and one 4 cycle rod. There is good agreement between measurements and predictions.

Figure 7-44 shows the measured and predicted diameter variations versus peak LHGR for four rodlets (Q11/1 , Q11/3, Q12/2 and M17/3) ramped in the TRANSRAMP IV program (Ref. 7-1). These ramp tests were characterized by a high ramping rate [d.] and, with the exception of rodlet M17/3 [d.], a short hold time [d.]. The agreement between measurements and predictions is good for rodlets Q11/3 and M17/3. It is not as good for rodlets Q11/1 and Q12/2. This may be due to the uncertainty in the experimental power level: the cladding deformation should be the same for a given power level and hold time because the burnup level was almost identical for all rodlets.

7.2.2.3.4. Uncertainties

The uncertainty range that contains [b.] is defined by unilateral bounds of [b.] (Figure 7-40).

7.2.2.4. Validity Range

The model was benchmarked within the following ranges:

[b., d.]< σ < [b., d.],
[b., d.]< T < [b., d.], and
[b., d.]< Φ < [b., d.].

The creep rate is determined with linear interpolation between the high and low stress creep model predictions in the transition range [b., d.].

7.2.3. *Alloy 5 Cladding Model*

7.2.3.1. Model

The high-stress creep model for the alloy 5 cladding was developed based upon (short-term) thermal creep tests performed on claddings irradiated for one and two cycles. The comparison of strain test data obtained from rods irradiated for 1 and 2 cycles does not show any significant difference versus fluence (Figure 7-45). Consequently, the relationship adopted for the irradiated material does not depend on fluence. This relationship, established on the basis of creep tests performed on material irradiated 1 and 2 cycles, is applicable only for [b.]:

[b.] Eq. 7-18

where:

[b., d.],

[b., d.],

[b., d.],

[b., d.],

σ : stress (MPa), $\sigma = \sigma_{\theta\theta} - \sigma_{rr}$,

$\sigma_{\theta\theta}$: clad hoop stress (MPa),

σ_{rr} : clad radial stress (MPa),

T : temperature (K), and

t : time (s).

An extension of this relationship to [b.] was established based upon long term tests performed on non-irradiated specimens. The relationship in this fluence range is:

[b., d.] Eq. 7-19

where:

ε : creep strain (fractional),

[b., d.],

[b., d.],

[b., d.],

[b., d.],

σ : stress (MPa), $\sigma = \sigma_{\theta\theta} - \sigma_{rr}$,

$\sigma_{\theta\theta}$: clad hoop stress (MPa),

σ_{rr} : clad radial stress (MPa),

T : temperature (K), and

t : time (s).

This relationship was incorporated into the COPERNIC code with the incremental computation process of [b]:

[b.] Eq. 7-20

[b.] Eq. 7-21

The strain at time t_1 is calculated from the strain at time t_0 with the following relationship:

[b.] Eq. 7-22

where [b.]. This equivalent time is determined with a Newton algorithm.

Before the power transient, the cladding creep is simulated with the base-load creep model (M5_98). Changeover from one relationship to the other is as follows:

Eq. 7-23

[b., d.]

Eq. 7-24

Eq. 7-25

7.2.3.2. Calibration Database

Creep tests were performed with non-irradiated specimens and samples taken from sections of fuel rods that were irradiated in PWR reactors.

The high-stress creep relationship is based upon short-term [e.] creep tests under the conditions listed in Table 7-7. The irradiated material tests were performed with samples from rods that were irradiated in Gravelines 5 for [e.].

Figure 7-46 shows the measured to predicted agreement for the alloy 5 high stress creep calibration database of irradiated materials.

The extension of this relationship to fluences less [b., d.] was established based upon long term tests performed on non-irradiated material [b., d.] (Table 7-7). The measured and predicted strains for these specimens are compared in Figure 7-47.

7.2.3.3. Validation Database and Uncertainties

The validation database consists of all the short-term creep test data available from irradiated material (Table 7-8) and power ramp data from an alloy 5 PWR rod (F10_4).

The irradiated material tests were performed on cladding sections from rods that were irradiated in Gravelines 5 for one and two cycles, with average fluences of [b., d.], respectively. The measured and predicted strains for these tests are compared in Figure 7-48.

The power ramp test F10_4 was conducted in the OSIRIS reactor. This test was performed under the following conditions with a rodlet constructed from a [e.] PWR rod:

- ramp rate : [b., d.], and
- hold time : [b., d.].

Plots of the measured and predicted strains before and after ramping are shown in Figure 7-49. Note the good agreement between predictions and measurements.

The uncertainty range is defined with unilateral bounds at [d.] (Figure 7-48). This [d.] uncertainty was defined without taking into account the strains less than [d.] (corresponding to the measurement uncertainty).

7.2.3.4. Validity Range

The validity range of the alloy 5 high-stress creep model for fluences less than or equal to [b., d.] is:

- temperature : [b., d.], and
- stress : [b., d.].

The validity range of the high-stress creep model for fluences greater than or equal to [b., d.] is:

- temperature : 350 to 380°C, and
- stress : 250 MPa to 470 MPa.

7.3. Irradiation Growth

7.3.1. Phenomenon and Modelling Principle

The irradiation free growth of a material is linked to an increase in volume, due to the vacancies and interstitials caused by fast neutrons. In Zirconium alloys, growth is positive in the direction of maximum strain during manufacturing and negative in the other directions according to the preferential grain orientation (Ref. 7-2 and Ref. 7-3).

The elongation of a fuel rod during its in-reactor irradiation results from the sum of the free growth phenomenon and the axial strains resulting from the in-service stress condition. The primary hypotheses related to the modelling are:

- the growth before pellet-clad contact is modelled by using a calibration database that includes rods that were irradiated [e.];

- the stress condition is calculated with the COPERNIC mechanical model with the 1D1/2 hypotheses: the mechanical approach is formulated with an axisymmetrical cylindrical

geometry using a generalized plane hypothesis (one-dimensional radial solution and uniform axial strain), and fuel-clad axial coupling effects are taken into account after gap closure;

- the following axial loads are not explicitly considered: interaction with the assembly structure and bearing force of the fuel column holddown spring. However, modelling of the growth before pellet-cladding contact implicitly accounts for the small axial forces induced by the fuel column holddown spring and the interactions with the structure.

With these hypotheses, rod elongation before pellet-clad results only from the growth model. When the gap is closed, fuel stack-cladding interaction changes the axial stress and creates an axial component.

7.3.2. Low Tin Stress-Relieved Zircaloy-4 Model

7.3.2.1. Model

Growth for low tin stress-relieved Zircaloy-4 rods before pellet-clad contact is predicted with an empirical relationship that is a function of [b.]. This relationship was established from on-site rod elongation measurements for [b., e.] before fuel stack-cladding interaction.

This relationship has the following form:

[b., d.] Eq. 7-26

where:

a	:	[b., d.],
b	:	[b., d.],
$\Delta L/L_0$	:	rod length variation (%),
L_0	:	initial length (m), and
Φ	:	fast fluence (E > 1 MeV) expressed in n/cm^2.

7.3.2.2. Calibration Database

This growth model was developed from on-site measurements of standard ZIRCOTUBE FRAGEMA UO_2 rods that were irradiated for [e.] in commercial reactors. This data included [e.] points from low tin AFA 2G cladding. The fluence of these rods did not exceed [b., d.]. The low fluence made it possible to exclude fuel-cladding interaction effects. The comparison of this relationship with experimental data is shown in Figure 7-50.

7.3.2.3. Validation Database

The rod elongations predicted by COPERNIC were compared with hot cell measurements for all FRAGEMA PWR UO_2 database rods irradiated for [e.]. The measured to predicted comparison of this data (Table 9-1) is presented in Figure 7-51. The measured to predicted agreement is [b.] for all of these PWR UO_2 rods.

This is a global validation of several models for rods irradiated [e.]. This is due to fuel-stack cladding interaction that includes pellet strain phenomena such as solid swelling or relocation.

7.3.2.4. Adaptation to Mixed Fuels

The test results from mixed oxide rods showed that the cladding dimensional variations are identical to those observed for UO_2 rods under equivalent conditions.

7.3.2.4.1. MOX

The growth model before pellet-clad contact uses the fast fluence of rods with E > 1 MeV as a parameter. [b.].

The rod elongations predicted by COPERNIC were compared with hot cell measurements for all FRAGEMA PWR MOX fuel rods. The measured to predicted comparison of these data (Table 9-2) is presented in Figure 7-52. The measured to predicted agreement is [b.] for all of these MOX fuel rods.

Again, this is a global validation of several models for rods irradiated [e.]. This is due to fuel-stack cladding interaction that includes pellet strain phenomena such as solid swelling or relocation.

7.3.2.4.2. UO_2-Gd_2O_3

Figure 7-53 shows a comparison of the measured and predicted elongations (Table 9-3) of all the gadolinia rods, allowing for the fluence of the surrounding UO_2 rods.

7.3.2.5. Validity Range

The validity range of this model corresponds to the code benchmarking ranges described in chapter 1.

7.3.3. Alloy 5 Cladding Model

7.3.3.1. Model

The alloy 5 growth before pellet-clad contact is modelled with an empirical relationship that is dependent on fast fluence (E >1 MeV). This relationship has the following form:

[b., d.] Eq. 7-27

where:

$\frac{\Delta L}{L_0}$: elongation (%),

L_0 : initial length (m), and

Φ : fast fluence (E > 1 MeV), (n/cm^2).

7.3.3.2. Calibration Database

This alloy 5 growth model before pellet-clad contact was developed with measurements taken on site from rods that were irradiated [b.] in PWR reactors. This made it possible to exclude [e.].

Table 7-9 summarizes the content of this database.

The comparison of the relationship with this experimental data is presented in Figure 7-54.

7.3.3.3. Validation Database

The rod elongations predicted by COPERNIC were compared with hot cell measurements for all of the alloy 5 database PWR rods that were irradiated for up to [e.]. The measured to predicted comparison of this data (Table 9-1) is presented in Figure 7-55. The measured to predicted agreement is [b.] for all of these alloy 5 PWR rods.

For rods irradiated [e.], this is a global validation. This is due to the fuel stack- cladding interaction that includes pellet strain phenomena such as solid swelling or relocation.

7.3.3.4. Validity Range

The validity range of this model corresponds to the code benchmarking ranges described in chapter 1.

REFERENCES

Ref. 7-1 S.DJURLE et al, *The influence of non-penetrating cladding crack on rod behaviour under transient operating conditions. Data from international TRANS-RAMPIV Project at Studsvik,* OCDE Specialist Meeting on Nuclear Fuel and Control Rods, Madrid, Spain, 5-7 November 1996. Studsvik Report NF(R)-97/018.

Ref. 7-2 R.B ADAMSON, *Irradiation Growth of Zircaloy,* American Society for Testing and Materials, 1977, p. 326-343.

Ref. 7-3 D.G. FRANKLIN, *Zircaloy-4 Cladding Deformations during Power Reactor Irradiation,* American Society for Testing and Materials, 1982, p. 235-267.

This page intentionally left blank.

FIGURES

FIGURE 7-1 LONG DURATION TEST [b.] - A1 TUBE

[b.]

FIGURE 7-2 MEASURED AND PREDICTED CREEP COMPARISON UNDER IRRADIATION

[b.]

FIGURE 7-3 MEASURED AND PREDICTED CLADDING DIAMETERS [b.]

[b.]

FIGURE 7-4 MEASURED AND PREDICTED CLADDING DIAMETERS [b.]

[b.]

FIGURE 7-5 MEASURED AND PREDICTED CLADDING DIAMETERS [b.]

[b.]

FIGURE 7-6 MEASURED AND PREDICTED CLADDING DIAMETERS [b.]

[b.]

FIGURE 7-7 MEASURED AND PREDICTED CLADDING DIAMETERS [b.]

[b.]

FIGURE 7-8 MEASURED AND PREDICTED CLADDING DIAMETERS [b.]

[b.]

FIGURE 7-9 MEASURED AND PREDICTED CLADDING DIAMETERS [b.]

[b.]

FIGURE 7-10 MEASURED AND PREDICTED CLADDING DIAMETERS

[b.]

[b.]

FIGURE 7-11 MEASURED AND PREDICTED CLADDING DIAMETERS

[b.]

[b.]

FIGURE 7-12 MEASURED AND PREDICTED CLADDING DIAMETERS

[b.]

[b.]

FIGURE 7-13 MEASURED AND PREDICTED CLADDING DIAMETERS

[b.]

[b.]

FIGURE 7-14 MEASURED AND PREDICTED CLADDING DIAMETERS

[b.]

[b.]

FIGURE 7-15 MEASURED AND PREDICTED CLADDING DIAMETERS

[b.]

[b.]

FIGURE 7-16 MEASURED AND PREDICTED CLADDING DIAMETERS

[b.]

[b.]

FIGURE 7-17 MEASURED AND PREDICTED CLADDING DIAMETERS

[b.]

[b.]

FIGURE 7-18 MEASURED AND PREDICTED CLADDING DIAMETERS

[b.]

[b.]

FIGURE 7-19 MEASURED AND PREDICTED CLADDING DIAMETERS

[b.]

[b.]

FIGURE 7-20 MEASURED AND PREDICTED CREEP COMPARISON [b.]

[b.]

FIGURE 7-21 MEASURED AND PREDICTED CREEP COMPARISON [b.]

[b.]

FIGURE 7-22 UNCERTAINTIES (CREEP UNDER IRRADIATION)

[b.]

FIGURE 7-23 MEASURED AND PREDICTED CLADDING DIAMETERS

[b.]

[b.]

FIGURE 7-24 MEASURED AND PREDICTED CLADDING DIAMETERS

[b.]

[b.]

FIGURE 7-25 MEASURED AND PREDICTED CLADDING DIAMETERS

[b.]

[b.]

FIGURE 7-26 MEASURED AND PREDICTED CLADDING DIAMETERS

[b.]

[b.]

FIGURE 7-27 MEASURED AND PREDICTED CLADDING DIAMETERS

[b.]

[b.]

FIGURE 7-28 MEASURED AND PREDICTED CLADDING DIAMETERS

[b.]

[b.]

FIGURE 7-29 MEASURED AND PREDICTED CREEP COMPARISON [b.]

[b.]

FIGURE 7-30 MEASURED AND PREDICTED CLADDING DIAMETERS

[b.]

[b.]

FIGURE 7-31 MEASURED AND PREDICTED CLADDING DIAMETERS

[b.]

[b.]

FIGURE 7-32 MEASURED AND PREDICTED CLADDING DIAMETERS

[b.]

[b.]

FIGURE 7-33 MEASURED AND PREDICTED CLADDING DIAMETERS

[b.]

[b.]

FIGURE 7-34 MEASURED AND PREDICTED CLADDING DIAMETERS

[b.]

[b.]

FIGURE 7-35 MEASURED AND PREDICTED CLADDING DIAMETERS

[b.]

[b.]

FIGURE 7-36 MEASURED AND PREDICTED CLADDING DIAMETERS

[b.]

[b.]

FIGURE 7-37 MEASURED AND PREDICTED CLADDING DIAMETERS

[b.]

[b.]

FIGURE 7-38 MEASURED AND PREDICTED CREEP COMPARISON AND UNCERTAINTIES (ALLOY 5 RODS)

[b.]

FIGURE 7-39 MEASURED AND PREDICTED RELAXATION TEST (ZIRCALOY-4)

[b.]

FIGURE 7-40 MEASURED AND PREDICTED HIGH STRESS CREEP COMPARISON (ZIRCALOY-4)

[b.]

FIGURE 7-41 MEASURED AND PREDICTED CLADDING DIAMETERS (B09_2 RAMP)

[b.]

FIGURE 7-42 MEASURED AND PREDICTED CLADDING DIAMETERS (K08_3 RAMP)

[b.]

FIGURE 7-43 MEASURED AND PREDICTED CLADDING DIAMETERS (I14_5 RAMP)

[b.]

FIGURE 7-44 MEASURED AND PREDICTED CLADDING DIAMETER VARIATIONS (TRANSRAMP IV RAMP)

[b.]

FIGURE 7-45 HIGH STRESS CREEP DATA COMPARISON AFTER 1 AND 2 CYCLES (ALLOY 5)

[b.]

FIGURE 7-46 MEASURED AND PREDICTED COMPARISON OF THE IRRADIATED MATERIAL CALIBRATION DATABASE

[b.]

FIGURE 7-47 MEASURED AND PREDICTED COMPARISON OF THE NON IRRADIATED MATERIAL CALIBRATION DATABASE

[b.]

FIGURE 7-48 MEASURED AND PREDICTED HIGH STRESS CREEP AND UNCERTAINTIES ON IRRADIATED MATERIALS (ALLOY 5)

[b.]

FIGURE 7-49 MEASURED AND PREDICTED CLADDING DIAMETERS

(F10_4 RAMP)

[b.]

FIGURE 7-50 GROWTH BEFORE PELLET-CLAD CONTACT

(ZIRCALOY-4)

[b.]

FIGURE 7-51 MEASURED AND PREDICTED COMPARISON OF THE FUEL ROD GROWTH (UO_2)

[b.]

FIGURE 7-52 MEASURED AND PREDICTED COMPARISON OF THE FUEL ROD GROWTH (MOX)

[b.]

FIGURE 7-53 MEASURED AND PREDICTED COMPARISON OF THE FUEL ROD GROWTH (UO_2-Gd_2O_3)

[b.]

FIGURE 7-54 GROWTH BEFORE PELLET-CLAD CONTACT (ALLOY 5)

[b.]

FIGURE 7-55 MEASURED AND PREDICTED COMPARISON OF THE FUEL ROD GROWTH (ALLOY 5)

[b.]

TABLES

TABLE 7-1 CALIBRATION DATABASE FOR ZIRCALOY-4 CLADDING LOW STRESS CREEP

ZS Irradiation Tests					
Test	Campaign	Duration, h	Tempera-ture, °C	Stress, MPa	Fluence, 10^{21} n/cm^2
[b.]					
PWR Fuel Rods					
Rod	Reactor	Duration, h	Tempera-ture, °C	Stress, MPa	Fluence, 10^{21} n/cm^2
[b.]					

TABLE 7-2 LIST OF UO_2 ZIRCALOY 4 RODS [e.]

Reactor	Rod Name or Position	Origin of Stress-Relieved Zy-4	Number of Cycles	Remarks
[b.]				

TABLE 7-3 LIST OF MOX RODS [e.]

Reactor	Rod Name or Position	Campaign	Number of Cycles	Type of Powder	Remarks
[b.]					

TABLE 7-4 CALIBRATION DATABASE FOR PRIMARY AND SECONDARY THERMAL CREEP ON NON IRRADIATED TUBES (ALLOY 5)

Stress (MPa)	Number of Experiments Temperature (°C)			
	320	350	380	400
	[b.]			

TABLE 7-5 CALIBRATION DATABASE FOR THERMAL SECONDARY CREEP HARDENING (ALLOY 5)

Rod Number	Alloy	Number of Cycles	Fluence (10^{25} n/m^2)
[b.]			

TABLE 7-6 CALIBRATION DATABASE FOR IRRADIATION CREEP (ALLOY 5)

PWR Fuel Rods							
Rod Name	Reactor	Number of Cycles	Duration, h	Temperature, °C	Stress, MPa	Fluence, 10^{25} n/m^2	Number of Axial Nodes
[b.]							

TABLE 7-7 CALIBRATION DATABASE FOR ALLOY 5 HIGH STRESS MODEL

Calibration Database on Irradiated Material						
Rod Name	Cycle	Span	Experiment Name	Temperature (°C)	Stress (MPa)	Fluence 10^{25} n/m^2
[b.]						

Calibration Database on Non-Irradiated Material		
Temperature (°C)	Stress (MPa)	Number of Experiments
[b.]		

TABLE 7-8 VALIDATION DATABASE FOR ALLOY 5 HIGH STRESS MODEL FOR IRRADIATED MATERIALS

Rod Name	Cycle	Span	Experiment Name	Temperature (°C)	Stress (MPa)	Fluence 10^{25} n/m^2
[b.]						

TABLE 7-9 CALIBRATION DATABASE FOR GROWTH BEFORE PELLET-CLAD CONTACT (ALLOY 5)

Reactor	Array	Cycle 1		Cycle 2	
		Number of Rods	Average Rod Burnup (GWd/tU)	Number of Rods	Average Rod Burnup (GWd/tU)
[b.]					

8. CLADDING CORROSION/HYDRIDING

The oxide module in COPERNIC determines the growth of the oxide layer that forms on the outer surface of the fuel rod cladding as a function of environmental conditions. The purpose of this module is to provide:

- the oxide layer thickness and the hydrogen concentration of the cladding in order to compare these predictions with operational criteria,
- the loss of cladding wall available to carry pressure and pellet contact loads and to absorb hydrogen,
- the increase in the cladding and internal gas and fuel temperatures as a consequence of the thermal resistance of the oxide layer.

There are a number of factors that are used by the oxide module to determine these changes. These are:

- the rate of oxide formation for a specific cladding type and a given temperature,
- the fraction of hydrogen released by the zirconium water reaction that is absorbed by the cladding,
- the thermal conductivity of the oxide layer,
- the ratio of the volume between the base metal consumed by the oxidation reaction and the oxide formed.

8.1. Corrosion

8.1.1. Phenomenon

The zirconium corrosion reaction with water (or steam) can be broadly represented by the following relationship:

$$Zr + 2H_2O \rightarrow ZrO_2 + 2H_2 \qquad \text{Eq. 8-1}$$

The corrosion reaction is characterized by a two-phase process:

* during the first phase, the metal is covered with a dense, adherent zirconia layer. The reaction is considered to be controlled by the diffusion of anion species through the oxide. The first phase is expressed [e.].

* the corrosion growth continues until the increase in stresses within the oxide layer causes the film to break. The oxide is characterized by a dense inner layer and a cracked outer layer in which there is a rise in the rate of migration of the oxidizing species towards the metal. The growth kinetics is [e.].

A fraction of the hydrogen released by the reaction described in Eq. 8-1 is absorbed in the cladding. The hydrogen is in dissolved form as long as the solubility limit at the relevant temperature is not reached. Beyond this limit, the hydrogen precipitates into the metal in the form of fine platelets.

8.1.2. Low Tin Stress-Relieved Zircaloy-4 Cladding Model

8.1.2.1. Model

The cladding external oxidation occurs in two phases:

- a pre-transition phase, modelled with a cubic corrosion expression, and
- a post-transition phase, that approximately follows a linear corrosion expression.

* Pre-transition:

The pre-transition phase is governed by the diffusion of oxygen in the zirconium. [b., d.]:

[b., d.] Eq. 8-2

and

[b., d.] Eq. 8-3

where

ΔS : increase in oxide thickness during the calculation time span (m),
S_0 : oxide thickness at time t_0 (m),
[b., d.],
[b., d.],
R : ideal gas constant ($J.mol^{-1}.K^{-1}$),
T_i : metal/oxide interface temperature (K),
T_s : oxide surface temperature (K),
FLUX : surface heat flux ($W.m^{-2}$),
[b., d.], and
S : oxide thickness (m).

During this phase, the oxide thickness is calculated over a time span:

$$\Delta t = t_1 - t_0 \quad \text{Eq. 8-4}$$

and

$$S_1 = S_0 + \Delta S \quad \text{Eq. 8-5}$$

where

Δt : time step (s),

t_0 : initial time (s),

t_1 : final time (s),

ΔS : increase in oxide thickness during the calculation time span (m),

S_1 : oxide thickness at time t_1 (m), and

S_0 : oxide thickness at time t_0 (m).

Pre-transition is complete when the time reaches:

[b.] Eq. 8-6

where

[b.]

The values that best predict the experimental results are:

[b., d.]

R =8.3144 J.mol^{-1}.K^{-1}, and
[b., d.].

Recent studies have shown that the thermal conductivity of zirconia is greater than values used in the past for the COROS02 code. A new thermal conductivity relationship was therefore developed that takes into account the oxide layer thickness and the thermal dependence of the oxide layer.

The thermal conductivity of the oxide layer is:

[b., d.]

* Post-transition:

The post-transition phase is also governed by the diffusion of oxygen in the zirconium, but this

phase is expressed with a [b.]:

[b.] Eq. 8-7

This model is based upon the STEHLE model (Ref. 8-1).

The increase in oxide thickness during the calculation time span (Δt) is determined with:

$$S_1 = S_0 + \Delta S \quad \text{Eq. 8-8}$$

and

[b.] Eq. 8-9

where

[b.] Eq. 8-10

[b.] Eq. 8-11

[b.] Eq. 8-12

ΔS	:	increase in oxide thickness during $\Delta t = t_1 - t_0$ (m),
S_0	:	oxide thickness at time t_0 (m),
S_1	:	oxide thickness at time t_1 (m),
FLUX	:	surface heat flux ($W.m^{-2}$),
[b.],		
T_i	:	metal/oxide interface temperature (K),
T_s	:	oxide surface temperature (K),
R	:	ideal gas constant (8.3144 $J.mol^{-1}.K^{-1}$),
[b.],		
[b.], and		
t	:	time (s).

The thermal conductivity relationship is the same as that used for the pre-transition phase.

The Q_{post} and K_{post} values were established as described below.

8.1.2.2. Calibration Database

8.1.2.2.1. Choice of Benchmarking Rods

Extensive experience is now available with low tin Zircaloy-4. The oxide thicknesses of approximately [b.] rods that have been measured on site are shown in Figure 8-1. The oxide data from the [b.] have been distinguished from the others in the figure. Figure 8-2 shows only the data from the [b.] and Figure 8-3 shows the remainder of the data. Average curves for the data are shown in both Figure 8-2 and 8-3. [b., e.].

8.1.2.2.2. Benchmarking Method

The rod was subdivided into [e.] axial increments. The thermal-hydraulic data shown in the following table was utilized.

Reactor	Coolant Inlet Temperature (°C)	Coolant Mass Flux ($kg.m^{-2}.s^{-1}$)	Equivalent Heating Diameter of the Flow Channel (mm)
[b., d.]			

[b., d.].

8.1.2.2.3. Determination of Post-Transition Constants

By analyzing data obtained in autoclaves, test loops, and reactors, the CEA has shown that the [b., e.]:

[b., e.].

The post-transition kinetic constant was determined by comparing [e.] with the measurements given in Table 8-1.

[e.]:

[b., d.].

8.1.2.2.4. Results

The maximum average azimuthal oxide thicknesses predicted for the [e.] given above are listed in Table 8-2 and the comparison between the measurements and the predictions is shown in Figure 8-5.

The [e.] pairing provided an accurate evaluation of the [e.] oxidation rate, allowing for the scatter in the measurements (Figure 8-4).

8.1.2.3. Validation Database and Uncertainties

8.1.2.3.1. At the Peak Corrosion Level

Figure 8-6 represents a comparison between the predictions and measurements for the low tin Zircaloy-4 experience acquired to date across the entire range of reactors.

8.1.2.3.2. At all Other Axial Levels

Figures 8-7 to 8-9 represent comparisons between the measurements taken at various axial levels and the predictions made with the above-described model.

The measured to predicted agreement of the oxide thicknesses at other levels is consistent with that of the peak corrosion level.

8.1.2.3.3. Bounding Thicknesses

The bounding oxide thicknesses are calculated from an upper-bound model that was obtained by [b.].

8.1.2.4. Application to Optimized FCF Low Tin Zircaloy-4 Cladding

The results from using COPERNIC to predict the peak oxide thickness on FCF fuel rods is shown in Figure 8-11 in the form of measured vs predicted oxide thickness. The same inputs were previously used with COROS02 to predict peak oxide thickness and those results are shown in Figure 8-12. The slope of the best estimate fit through the measured to predicted oxide thickness is nearly identical, [e.].

8.1.2.5. Adaptation to Mixed Fuels

No difference in corrosion behavior has been observed for mixed fuel rods. Figure 8-13 shows the measured corrosion thicknesses versus fuel rod burnup for the following fuels:

- $(U,Pu)O_2$,
- UO_2-Gd_2O_3, and
- UO_2.

The above models are therefore applicable to both $(U, Pu)O_2$ and UO_2-Gd_2O_3 rods.

8.1.2.6. Validity Range

The validity range of this model corresponds to the code benchmarking ranges described in chapter 1.

8.1.3. Alloy 5 Cladding Model

8.1.3.1. Model

The alloy 5 model also contains two phases:

- a pre-transition phase, and
- a post-transition phase.

* Pre-transition:

The alloy 5 pre-transition phase is expressed with a [b.]:

[b., d.] Eq. 8-13

This relationship is used up to a transition oxide thickness of [d.]. During this phase, the increase in the oxide thickness is calculated for time intervals $\Delta t = t_1 - t_0$ with $S_1 = S_0 + \Delta S$:

[b., d.] Eq. 8-14

where

ΔS : increase in oxide thickness during the calculation time span (m),

S_0 : oxide thickness at time t_0 (m),

S_1 : oxide thickness at time t_1 (m),

[b.],

[b.],

T_i : metal/oxide interface temperature at time t_0 (K), and

Δt : time step (s).

* Post-transition:

The alloy 5 post-transition phase is expressed with [b.]:

[b., d.] Eq. 8-15

During this post-transition phase, the increase in the oxide thickness ($\Delta S = S_1 - S_0$) during time interval ($\Delta t = t_1 - t_0$) is determined with:

[b., d.] Eq. 8-16

where

ΔS : increase in oxide thickness during the calculation time span (m),

S_0 : oxide thickness at time t_0 (m),

S_1 : oxide thickness at time t_1 (m),

[b.],

[b.],

T_i : metal/oxide interface temperature at time t_0 (K), and

Δt : time step (s).

The metal/oxide interface temperature is calculated with the following relationship, irrespective of the corrosion phase:

$$T_i = T_s + \frac{FLUX \cdot S}{\lambda}$$ Eq. 8-17

where

T_s : oxide surface temperature at time t_0 (K),

FLUX : surface heat flux ($W.m^{-2}$), and

λ : thermal conductivity of the zirconia ($W.m^{-1}.K^{-1}$).

The thermal conductivity relationship for the alloy 5 oxide layer [b.].

[b., d.]

[b., d.] Eq. 8-18

[b., d.]

The uncertainties associated with the measurements are:

- [b., d.],

- [b., d.] and

- [b., d.].

The minimization of the χ^2 function was performed with a non-linear least squares method with [e.]. Resolution by non-linear least squares (Levenberg-Marquardt method) ensures convergence and provides a correlation matrix between the investigated parameters to be calculated. [d]:

[d].

The value of χ^2 is equal to [d], hence:

[d] Eq. 8-19

8.1.3.2. Calibration Database

Starting with the oxide thickness database available to date for alloy 5 rods, a calibration database was constructed that consists of measurements taken:

- on site (by SABRE blade or FISCHER probe),
- in hot cells by Eddy current, and
- from metallographs,

and comprising:

- the widest burnup range to date, including the measurements taken after [b.] cycles of irradiation,
- a variety of reactors (or geometries) and fuel management schemes: [b.],
- metallographs taken after [b.].

The data obtained during the hot cell examinations was reduced [d.].

[b., d.]

The alloy 5 calibration database, therefore, consists of [e.]:

[b., d.]

The alloy 5 zirconia thickness measurements in the calibration database are shown plotted versus the rod average burnup in Figure 8-14. The comparison of the measured and predicted alloy 5

data of the calibration database is shown in Figure 8-15. This figure indicates good measured to predicted agreement particularly for:

- [b., d.], and
- [b., d.].

8.1.3.3. Validation Database and Uncertainties

The validation database includes all of the measurements taken on site (FISCHER or SABRE blade), in the hot cell (destructive and non-destructive examinations) from all measured spans.

Figure 8-16 represents the maximum average azimuthal oxide thickness at the maximum corrosion span versus the rod average burnup.

Figure 8-17 shows good agreement between the measured and predicted oxide thicknesses for the entire validation database.

The measured and predicted zirconia thicknesses, for each type of reactor [b., d.].

An upper-bound model was constructed from the validation database, [b., d.]:

[b., d.] Eq. 8-20

[b., d.]

8.1.3.4. Benchmarking Range

The validity range of the alloy 5 cladding corrosion model corresponds to the code validity ranges described in chapter 1.

8.2. Hydriding

8.2.1. Phenomenon

The zirconium corrosion reaction with water (or steam) can be represented with the following relationship:

$$Zr + 2H_2O \rightarrow ZrO_2 + 2H_2 \qquad \text{Eq. 8-21}$$

The zirconium oxide is primarily formed on the outer surface of the cladding. A fraction of the hydrogen released is absorbed in the cladding.

8.2.2. Low Tin Stress-Relieved Zircaloy-4 Cladding Model

8.2.2.1. Model

[b., d.] Eq. 8-22

[b., d.]

[b., d.] Eq. 8-23

[b., d.] Eq. 8-24

8.2.2.1.1. Zircaloy-4 Thickness after Corrosion

[b., d.] Eq. 8-25

[b., d.] Eq. 8-26

8.2.2.1.2. Correction of the CEA Measurement

The results obtained by the CEA correspond to an overall measurement of the hydrogen in the metal, at the metal/oxide interface and in the oxide.

The measurements obtained by SIMS (Ref. 8-3), GDS or by the nuclear method show that a heavy hydrogen concentration is present at the metal/oxide interface and in the oxide.

The hydrogen is [e.]:

[e.]

In the following, it is [e.], which is justified by the EDF measurements on a sample from an autoclave test. These measurements showed that the hydrogen concentration [e.].

Let (per unit surface area in dm^2):

- h : quantity (in g) of total hydrogen (measured by the CEA),
- h_m : quantity (in g) of hydrogen in the metal,
- H : concentration (in ppm) of total hydrogen adjusted to the metal (CEA measurement), and
- H_m : concentration (in ppm) of hydrogen in the metal.

Since fuel rod cladding hydrogen concentrations are limited by operational criteria, it is assumed that the hydrogen [e.].

Eq. 8-27

Eq. 8-28

[b., d., e.]

Eq. 8-29

Eq. 8-30

Eq. 8-31

[b., d., e.]

Eq. 8-32

8.2.2.2. Hydrogen Content and Hydrogen Pickup Fraction

Eq. 8-33

Eq. 8-34

[b., d.]

Eq. 8-35

Eq. 8-36

Eq. 8-36 can then be used with the measured oxide thickness and hydrogen content data to determine the hydrogen pickup fraction.

8.2.2.3. Validation Database and Uncertainties

The hydrogen measurements obtained by the CEA are listed in Table 8-3 and are shown in Figure 8-22 in corrected hydrogen content form (H_m), determined by the equation Eq. 8-32, versus the oxide layer.

Two observations can be made from this curve:

[b.]

The latter measurements correspond to the creation of a new channel for off-gassing from the hot cells which has higher performance than the former one.

Given that the oxidation levels [e.] are more representative of the corrosion levels that will be reached on the rods during irradiation or during a design study, it is recommended that these results be used to determine the hydrogen pickup fraction.

Figure 8-23 shows the hydrogen concentration versus oxide thickness on the rods extracted after five cycles.

Figure 8-24 shows the hydrogen pickup fraction (determined by Eq. 8-36) versus oxide thickness.

The hydrogen pickup fraction on the average is equal to [d.] which is consistent with the results in the open literature. This value is similar to the pickup fraction determined in Ref. 8-4 for FCF standard tin Zircaloy-4 cladding. Therefore, the pickup fraction of [d.] will also be used for FCF fuel analysis. The predicted hydrogen content is then determined by Eq. 8-35. Note that if the full set of results is considered, the hydrogen pickup fraction is equal to [d.], which corresponds to the upper range (Figure 8-25).

8.2.2.4. Validity Range

The validity range of this model corresponds to the code benchmarking ranges described in chapter 1.

8.2.3. Alloy 5 Cladding Model

8.2.3.1. Model

The relationship for hydrogen content [b., d., e.]:

[d.] Eq. 8-37

where

[d.]

8.2.3.2. Experimental Validation and Uncertainties

The alloy 5 hydriding model is based upon hydrogen and zirconia hot cell measurements that were obtained from rods that had been irradiated from [b., d.] in PWR reactors. This data are presented in Table 8-4 that includes the:

- reactor and the number of cycles,
- number of rods analyzed and the assembly in which they were irradiated,
- rod average burnup,
- hydrogen content, and
- zirconia thickness that was measured [b.].

Before irradiation, the hydrogen concentration in the cladding was determined from chemical analyses. The initial content was [d.].

Figure 8-26 is a plot of the total hydrogen content versus rod average burnup. The total hydrogen content versus zirconia thickness is shown in Figure 8-27. [d.].

An upper bound of the hydrogen content is determined by evaluating the hydrogen content with a maximum zirconia thickness determined from the corrosion model upper bound.

8.2.3.3. Validity Range

The validity range of the hydriding model corresponds to the code benchmarking ranges described in chapter 1.

REFERENCES

Ref. 8-1 H. STEHLE, W. KADEN, R. HANZEL, *External Corrosion of Cladding in PWRs*, Nuclear Engineering and Design 33, pp 15-169, 1975.

Ref. 8-2 EPRI Report, *Waterside Corrosion of Zircaloy clad fuel rods*, NPSD 792 - May 1982.

Ref. 8-3 A.M. BRENNENSTUHL et al, *Deterium in-depth analyses of oxidized Zr-2.5% Nb pressure tube samples removed from an operating nuclear reactor fuel channel*, Technology Conference, Alliston, Ontario, Canada, 11/89.

Ref. 8-4 BAW-10183-A, *Fuel Rod Gas Pressure Criterion (FRGPC)*, July 1995.

This page intentionally left blank.

FIGURES

FIGURE 8-1 LOW TIN ZIRCALOY-4 (AFA 2G) CLADDING EXPERIENCE

[b.]

FIGURE 8-2 AFA 2G EXPERIENCE IN [b.]

[b.]

FIGURE 8-3 AFA 2G EXPERIENCE IN [b.]

[b.]

FIGURE 8-4 AFA 2G [b.]

[b.]

FIGURE 8-5 COMPARISON BETWEEN MEASUREMENTS AND PREDICTIONS [b.]

[b.]

FIGURE 8-6 COMPARISON BETWEEN MEASUREMENTS AND PREDICTIONS FOR [b.]

[b.]

FIGURE 8-7 COMPARISON BETWEEN MEASUREMENTS AND PREDICTIONS FOR [b.]

[b.]

FIGURE 8-8 COMPARISON BETWEEN MEASUREMENTS AND PREDICTIONS FOR [b.]

[b.]

FIGURE 8-9 COMPARISON BETWEEN MEASUREMENTS AND PREDICTIONS FOR [b.]

[b.]

FIGURE 8-10 COMPARISON BETWEEN MEASUREMENTS AND BOUNDING PREDICTIONS

[b.]

FIGURE 8-11 COPERNIC MEASURED TO PREDICTED LEAST SQUARE FIT

[b.]

FIGURE 8-12 COROS02 MEASURED TO PREDICTED LEAST SQUARE FIT

[b.]

FIGURE 8-13 DIFFERENT FUEL EXPERIENCES: UO_2, $(U,Pu)O_2$, UO_2-Gd_2O_3

[b.]

FIGURE 8-14 ZIRCONIA THICKNESSES VERSUS ROD AVERAGE BURNUP FOR ALLOY 5 RODS IN THE CALIBRATION DATABASE

[b.]

FIGURE 8-15 ALLOY 5 CALIBRATION DATABASE: MEASURED AND PREDICTED ZIRCONIA THICKNESS COMPARISON

[b.]

FIGURE 8-16 ALLOY 5 VALIDATION DATABASE: MAXIMUM AVERAGE AZIMUTHAL OXIDE THICKNESSES MEASURED AT THE MAXIMUM CORROSION SPAN VERSUS ROD AVERAGE BURNUP

[b.]

FIGURE 8-17 ALLOY 5 VALIDATION DATABASE: MEASURED AND PREDICTED ZIRCONIA THICKNESS COMPARISON

[b.]

FIGURE 8-18 VALIDATION DATABASE [b.]: MEASURED AND PREDICTED ZIRCONIA THICKNESS COMPARISON

[b.]

FIGURE 8-19 VALIDATION DATABASE [b.]: MEASURED AND PREDICTED ZIRCONIA THICKNESS COMPARISON

[b.]

FIGURE 8-20 VALIDATION DATABASE [b.]: MEASURED AND PREDICTED ZIRCONIA THICKNESS COMPARISON

[b.]

FIGURE 8-21 UPPER-BOUND ZIRCONIA THICKNESS MODEL

[b.]

FIGURE 8-22 HYDROGEN CONTENT VERSUS OXIDE THICKNESS FOR ZIRCALOY-4 CLADDING

[b.]

FIGURE 8-23 HYDROGEN CONTENT VERSUS OXIDE THICKNESS FOR THE ZIRCALOY-4 RODS IRRADIATED [b.]

[b.]

FIGURE 8-24 HYDROGEN PICKUP FRACTION VERSUS OXIDE THICKNESS FOR THE ZIRCALOY-4 RODS [b.]

[b.]

FIGURE 8-25 HYDROGEN PICKUP FRACTION VERSUS OXIDE THICKNESS FOR ZIRCALOY-4 CLADDING

[b.]

FIGURE 8-26 HYDRIDE CONTENT VERSUS ROD AVERAGE BURNUP FOR ALLOY 5 -CLADDING

[b.]

FIGURE 8-27 HYDROGEN CONTENT VERSUS OXIDE THICKNESS FOR ALLOY 5 CLADDING

[b.]

TABLES

TABLE 8-1 AFA 2G [b.]

Reactor	Assembly	Cycle	Rod	Rod Average Burnup (MWd/tU)	Average Azimuthal Thickness at the Peak Level (µm)
[b.]					

TABLE 8-2 PREDICTED OXIDE THICKNESSES [b.]

Reactor	Assembly	Cycle	Rod	Predicted Oxide Thickness (µm)
[b.]				

TABLE 8-3 HYDROGEN CONTENT OF IRRADIATED RODS

Reactor	Oxide Thickness (μm)	Measured Hydrogen Content H (ppm)	Corrected Hydrogen Content H_m (ppm)	Hydrogen Pickup Fraction

[b.]

Reactor	Oxide Thickness (µm)	Measured Hydrogen Content H (ppm)	Corrected Hydrogen Content H_m (ppm)	Hydrogen Pickup Fraction
[b.]				

TABLE 8-4 HYDROGEN CONTENT OF ALLOY 5 - EXPERIENCE

Reactor	Cycle	Fuel Assembly	Number of Rods	Rod Average Burnup (MWd/tU)	Zirconia Layer Thickness (µm)	Hydrogen (ppm)

[b.]